

SIMULATION OF ATMOSPHERIC DUST CLOUDS

Dissertation
zur Erlangung des Doktorgrades
des Departement Physik
der Universität Hamburg

vorgelegt von
Sören Witte
aus Greifswald

Hamburg
2011

Gutachter der Dissertation: Prof. Dr. P. Hauschildt
Prof. Dr. R. Neuhäuser

Gutachter der Disputation: Prof. Dr. J. Schmitt
Prof. Dr. R. Banerjee

Datum der Disputation: 03. Juni 2011

Vorsitzender des Prüfungsausschusses: Dr. R. Baade
Vorsitzender des Promotionsausschusses: Prof. Dr. P. Hauschildt
Dekan der MIN-Fakultät: Prof. Dr. H. Graener
Leiterin des Departement Physik: Prof. Dr. D. Pfannkuche

Zusammenfassung

Die Atmosphäre der Erde weist eine Vielzahl an Wettereffekten auf. Wolken, als einer von ihnen, haben immer das Interesse der Menschen geweckt und sie inspiriert.

Die Bildung von Wolken beginnt mit der Kondensation von Gas. Die Größe der sich bildenden Tröpfchen ist bestimmt durch ein Gleichgewicht zwischen Wachstum und Verdampfung. Die Tröpfchen schweben nahezu, solange sie klein sind. Sobald sie größer werden, beispielsweise durch sinkende Gastemperaturen, werden sie zunehmend stärker durch Gravitation beeinflusst. Mit anderen Worten, die Tropfen regnen aus der Atmosphäre bis keine weiteren gebildet werden können. Aufsteigende Strömungen der Atmosphäre tragen das wieder verdampfte Wasser zurück in höhere Schichten der Atmosphäre, was den Kreislauf schliesst.

Die Bildung von Wolken ist nicht beschränkt auf terrestrische Planeten, sondern reicht über jovianische Planeten und braune Zwerge bis hin zu den masseärmsten Sternen. Verglichen mit der Erde sind viele dieser Objekte wesentlich heisser. Die entsprechenden Wolken bestehen nicht aus Wasser, sondern aus kondensierten Metallen, die Staubkörner bilden. Besonders Silikatwolken welche die Oberflächen von braunen Zwergen und den kältesten Sternen bedecken sind opak. In den betroffenen Objekten kann dies eine Aufheizung des Gases um bis zu 1000K bewirken. Verständlicherweise, beeinflusst dies die chemische Zusammensetzung der Atmosphären. Die Bildung und anschließende Fällung der Staubpartikel verringert die Menge der schweren Element im sichtbaren Teil der Atmosphäre. Insgesamt haben Wolken gewöhnlich einen immensen Einfluß auf die spektrale Erscheinung von Atmosphären.

Diese Arbeit ist befasst mit der theoretischen Untersuchung von Staubwolken. Hierfür wurden selbstkonsistente 1D Atmosphären mit stationären Staubwolken über einen großen Bereich von Atmosphärenparameter berechnet. Die zur Verfügung stehenden Eingabedaten gestatten die Berechnung von Silikat- und Metallwolken in Atmosphären von Zwergsternen und braunen Zwergen. Die in früheren Arbeiten begonnene Diskussion der Entwicklung von Wolken über den Parameterraum wird in dieser Arbeit fortgesetzt. Durch die Einführung von Größen, wie der Säulendichte des Staubvolumens, kann erstmals ein direkter Vergleich der Staubmenge und Zusammensetzung für verschieden Modell-Parameter durchgeführt werden. Zusätzlich werden die zugehörigen synthetischen Spektren systematisch mit Beobachtungen verglichen. Allgemein ist die Übereinstimmung zwischen Modellen und Beobachtungen wesentlich besser als bei allen vorhergehenden Modellgenerationen. Leider sind die Modellen nicht in der Lage, den plötzlichen Verlust der Staubopazität, welcher bei späten L Spektraltypen beobachtet wird, zu reproduzieren. Entkoppelte Konvektionszonen wurden als eine wahrscheinliche Ursache identifiziert. Basierend auf identifizierten Modell-Defiziten werden modifizierte Staubratengleichungen für zukünftige Implementation hergeleitet.

Abstract

Earth's atmosphere exhibits a broad diversity of weather effects. Clouds, as one of them, have always drawn attention and inspired people.

The formation of clouds begins with the condensation of gas. The size of forming droplets depends on the equilibrium between their growth and evaporation. As long as the droplets remain small, they are more or less levitating. Once they become larger, for instance due to decreasing gas temperatures, they are stronger subject to gravitational settling. In other words, the drops will rain out of the atmosphere until no new ones can form. Upstreams in the atmospheres carry the re-evaporated water back into the higher layers of the atmosphere, which closes the cycle.

The formation of clouds is not limited to terrestrial planets but extends from there over the Jovian planets and brown dwarfs up to the least massive stars. In contrast to Earth, many of these objects are considerably hotter. The corresponding clouds are not made of water but instead of condensed metals, forming so-called dust grains. Especially the silicate clouds that cover the atmosphere of hot brown dwarfs and the coolest stars are very opaque. In the respective objects, this causes a considerable heating of the gas of up to 1000K. Obviously, this affects the chemical composition of the atmosphere. The formation and subsequent precipitation of dust particles depletes the observable gas of heavy elements. Altogether, clouds typically have an immense influence on the spectral appearance of an atmosphere.

This work is concerned with the theoretical study of such dust clouds. For this, self-consistent 1D atmospheres involving stationary dust clouds were calculated over a wide range of atmosphere parameters. The existing input data allows the calculation of silicate and metal clouds in stellar and brown dwarf atmospheres. The discussion of the development of the model cloud with the parameters, started in earlier works, is continued here. Among the most interesting results are the typical timescales for the descent of dust particles. With the introduction of quantities such as the column densities of dust grain volume, the amount of dust and its composition is compared directly between different stellar parameters. In addition, the corresponding synthetic spectra are systematically compared to the observations. Generally, the agreement between models and observations is considerably better than in all previous model generations. Unfortunately, the models are incapable of reproducing the sudden loss of dust opacity that is observed for late L spectral types. Detached convection zones have been identified as a likely reason. Based on identified model deficiencies, modification of the system of dust rate equations are derived for future implementation.

Contents

1	Motivation	1
2	Theoretical Approach: Atmospheres	6
2.1	Prerequisites	6
2.2	Stellar atmospheres	7
2.3	Radiative transfer	9
2.4	Gas phase chemistry	10
2.5	Stellar parameters	11
3	Theoretical Approach: Clouds	13
3.1	Composition of dust grains and definition of the grain size distribution . . .	13
3.2	Nucleation rate	14
3.3	Collision and growth rates	15
3.4	Evaporation rates	18
3.5	Effective growth rate	19
3.6	Equation of motion	20
3.7	Flow rate	21
3.8	Dust rate equations	23
3.9	Element rate equations	25
3.10	Final system of equations	25
3.11	Dust opacity	26
4	Model Code	28
4.1	The PHOENIX code	28
4.2	The DRIFT code	30
4.3	Merging DRIFT with PHOENIX	31
4.4	Adaption of ACES	32
5	Results: The model atmospheres	37
5.1	The gas phase	37
5.2	Atmospheric conditions	41
5.3	Revisiting the cloud structure	43
5.4	The cloud in general	45
5.4.1	The cloud structure as function of the stellar parameters	45
5.4.2	Geometrical extension of the cloud	48
5.4.3	Life cycle of a dust grain	49
5.4.4	Amount of dust	51

5.5	Grain composition	56
5.6	Metallicity	61
6	Results: Testing of models on observations	67
6.1	Observational data and fitting process	67
6.2	Effective temperature-spectral type sequence	68
6.3	Photometry	78
7	Conclusions	81
8	Framework for future dust models	86
8.1	Convective term	86
8.2	Improved plane-parallel 1D model	90
8.3	Spherical 1D model	94
8.4	Time-dependent 3D model in spherical geometry	96
9	Future prospects	99
	Literature	100



1 Motivation

Atomic nuclei and electrons seek to minimize their inner energy by bonding together, eventually forming neutral atoms. Likewise, atoms attain more favorable energetic states by sharing valence electrons. The higher the number densities of particles in a gas, the higher is the chance to form such neutral atoms and molecules. Counteracting the stability of these compounds are the radiation field and the thermal energy. For gas temperatures of thousands of Kelvin, the thermal energy dominates the chemical equilibrium completely, effectively inhibiting the formation of molecules.

The stars of the earliest spectral types are very hot and luminous. Hence, ionized non-molecular gas is the mainstay of respective stellar atmospheres. Moving along the main sequence of the Hertzsprung-Russell diagram, the atmospheres become more dense and cooler. This enhances the rate of stable recombination of nuclei and electrons and slightly later also the formation of persistent molecules. At some critical point, the gas becomes so dense and cool that the molecules begin to stick together at such high rates that they start to form macro-molecules that eventually relax into a lattice structure. In other words, solid particles form within these atmospheres. With a higher density than their environment, these so-called dust grains descend into the deeper layers of the atmosphere. Mixing processes replenish some of the material which results in quasi-static clouds within the atmosphere.

The critical combination of high density and low temperature that permits stable condensation is reached at the very bottom of the stellar main sequence. In direct continuity of this sequence, evolutionary tracks of substellar objects align to a pseudo-main sequence. The temperatures and densities of the corresponding atmospheres permit the condensation of more and more material. This extends down into the planetary regime, excellently demonstrated by the atmosphere of Earth with its water clouds and near-complete rain-out of chemical metals.

This work is concerned with the simulation of atmospheric dust clouds, their feedback on these atmospheres and their influence on the emerging spectra. In the following, the affected objects as well as the corresponding spectral types are briefly discussed. A timeline of the atmospheric cloud modelling is given. For a more comprehensive overview, review publications such as Allard et al. (1997), Basri (2000), Chabrier & Baraffe (2000), Chabrier et al. (2005) and Kirkpatrick (2005) are recommended.

Latest type stars: The commonly accepted mechanism of the star formation is the fragmentation and collapse of gas clouds, first formulated by Jeans (1902), although the underlying concept was already discussed more than a century earlier (Kant, 1755). The cosmological redshift was first derived theoretically by Lemaître (1927), soon followed by observational verification (Hubble, 1929). In this context, the classical stellar formation theory by Jeans

(1902) postulated that objects of only few percent of the solar mass could not have formed, since the corresponding timescales for the collapse exceeded the Hubble time, very roughly serving as placeholder for the age of the universe, by almost one order of magnitude. Similarly, the still large collapse timescales of slightly more massive stars would hypothetically have limited the number of such objects. Conflicting with this, there is observational evidence for the dominance of subsolar mass stars (e.g., Weigert & Wendker, 2001) with respect to the stellar mass distribution. Hayashi (1962) showed that convective rather than radiative energy transfer was responsible for the cooling the inner parts of less massive collapsing gas cloud. Based on this more efficient dissipation of energy, Kumar (1963a,b) derived collapse timescales of less than a billion years for objects of a few percent of a solar mass.

Brown dwarfs: At some point of the stellar formation, the temperatures and densities at the core of the protostar have become high enough to raise the rate of tunneling events on the atomic level that form larger atomic nuclei. Eventually, the amount of released nuclear energy becomes large enough to counteract the collapse by emission at the outer boundary of the cloud. Therefore, the resulting star assumes a nearly steady state. The first nuclides to fuse at a notable rate are tritium, deuterium and lithium isotopes. None of them are typically very abundant in the interstellar medium of which collapsing gas clouds are formed in the first place. Therefore, only the energy released by the fusion of the considerably more abundant hydrogen can stop the contraction of gas clouds.

Below a final mass of about $m_{\text{HBMM}} = 0.07M_{\odot}$ for solar element abundances (Chabrier et al., 2005) the temperatures and densities at the core of an object will never develop a stable fusion zone that could yield the sufficient energy output to counteract the ongoing contraction for long. This distinguishes so-called substellar objects from stars. Another commonly used term for substellar objects that form through gravitational collapse of gas clouds is “brown dwarf” (Tarter, 1975, 1976). Ultimately, the contraction of brown dwarfs is stopped by degeneracy of the electron gas (e.g., Hayashi & Nakano, 1963). Rebolo et al. (1992) introduced the lithium test in order to find a safe criterion to prove the substellar nature of an observed object. The idea behind it is that objects of less than ~ 60 Jupiter masses do not reach sufficiently high densities and temperatures at their cores to fuse lithium. Combined with the fact that objects of this mass range are nearly fully convective the presence of atmospheric lithium suggests a mass of less than 60 Jupiter masses, hence, substellarity.

Radiating away their energy, the brown dwarfs experience a sustained contraction and become cooler (e.g., Chabrier et al., 2000). In contrast to stars, such objects evolve continuously, hence, their spectral appearance varies with time. The slow initial contraction compared to stars causes stronger uncertainties with respect to the age determination of very young brown dwarfs since they will still show signs of their accretion history (Baraffe & Chabrier, 2010). At higher ages, the cooling tracks of substellar objects as functions of mass show overlaps in the stellar parameter space. In other words, unlike main sequence stars, brown dwarfs possess no unique effective temperature that can be attributed to each classical spectral type. For this reason, Kirkpatrick (2005) suggested a spectral classification that involves other parameters such as the surface gravity and metallicity.



As a matter of fact, substellar objects are very faint, which rendered their observation impossible in the years after Hayashi (1962) had shown that such objects could form indeed. For this reason, substellar objects have been considered for the apparent discrepancy between luminous and gravitational mass of galaxies and galaxy clusters. More recent studies of the mass distribution of brown dwarfs speaks against this hypothesis (e.g., Thies & Kroupa, 2007) while current world models require non-baryonic matter to explain the missing mass problem (e.g., Schneider, 2006).

So far, no definite lower mass limit has been found observationally for the gas cloud collapse. Béjar et al. (2001) and other groups have reported the observation of free floating objects of masses of only few Jupiter masses in young stellar clusters. Simulations (e.g., Whitworth & Stamatellos, 2006) predict such a lower mass limit close to one Jupiter mass.

Technically, the first definite brown dwarfs were discovered by Rebolo et al. (1995), although their substellarity was not universally accepted at the time. Shortly after, Nakajima et al. (1995) published the discovery of Gl 229B. Its strong methane absorption set it apart from stars while other characteristics spoke against a planetary nature (Basri, 2000). Therefore, it became the first accepted brown dwarf. Over the following years, hundreds of confirmed brown dwarfs have been detected which can be attributed mostly to surveys such as 2MASS (Kleinmann, 1992) or DENIS (Epchtein & Mamon, 1992) .

Planets: Unlike stars or brown dwarfs, planets do not form by simple collapse of gas clouds but inside of protoplanetary disks around a young parent star. A straightforward collapse of a part of the disk is excluded as well, since Keplerian shearing of the material proceeds faster than any hypothetical collapse (e.g., Wuchterl, 2004). Instead, mostly heavier elements of the disk begin to form dust particles while much of the lighter elements are slowly blown out of the stellar system by the stellar radiation or are scattered away by collision with dust particles (Chabrier et al., 2005). The dust particles coagulate and eventually form planetesimals that accrete smaller rocks in proximity of their orbit (Blum & Wurm, 2008). Geology studies of meteorites suggest that silicate melts could be required for the formation of planets because they could significantly increase the rate of non-destructive collisions between meter-sized rocks (e.g., Trialet et al., 2009). Once massive planetary cores have formed, they quickly sweep their environment free of most of the remaining gas and dust (e.g., Wuchterl, 2008). Closer to the host star, the disk is swept away much earlier. On the other hand, at higher distance to the central star, the density of the disk is decreasing fast. Hence, inner planets form fast but accrete comparably small amounts of gas to form an atmosphere, while further outside, planetesimals can not grow sufficiently to form a planet in the end. In between, giant planets can form, because there is ample material to form large cores and enough time before the disk has dissolved to accrete enough gas (e.g., Wuchterl, 2008).

For long, only the planets of our own solar system were observable. The first detected planet outside of the solar system, a so-called exoplanet, was HD 114762b (Latham et al., 1989). Unfortunately, its then suspected planetary nature could only be confirmed years later. The first system with multiple planets outside of the solar system was reported by Wolszczan & Frail (1992). Since the host object was a pulsar, this discovery attracted less interest than Mayor & Queloz (1995) who reported the first confirmed planetary de-

tection around a main sequence star. Since then, hundreds of stars have been detected through various methods. Current projects such as COROT (Catala et al., 1995) and KEPLER (Borucki & Summers, 1984) are going to raise this number considerably over the following years.

The observational data of exoplanets reveals that there are many objects of several Jupiter masses (e.g., Johnson, 2009). This means there is an overlap with brown dwarfs with respect to the mass. Likewise, there is an overlap between brown dwarfs and hot exoplanets with respect to the effective temperatures. For both reasons, a spectral distinction of both kinds of objects can become tricky. As mentioned above, the relative abundance of heavy elements is enhanced in protoplanetary disks (Chabrier et al., 2005). Hence, planets will show higher metal abundances than their host star while brown dwarfs should feature about the same composition as their more massive companion. In order to have a systematic distinction between planets and brown dwarfs, the International Astronomical Union published a working definition: Objects that orbit stars or stellar remnants that are not massive enough to sustain deuterium burning at their core are called planet, irrespective of their formation process. All other objects are called brown dwarfs. Arguably, this definition has left many astronomers unsatisfied because the formation mechanism has been ignored in favor of an arbitrarily chosen delimiter.

Spectral types: The spectral appearance of dust-bearing atmospheres shows broad diversity. This is not surprising since the effective temperature window of such objects ranges over almost 3000K. Therefore, the gas temperatures alone will cause a strong diversity of the spectral energy distribution and the atmospheric chemistry. In common procedure, new spectral types were defined for classification of such objects.

The spectral type M is one of the original types that have existed quite long. Hallmark of M dwarfs are strong molecular bands of species such as TiO and VO. In the latest type M dwarfs, oxygen-rich solid compounds begin to form dust clouds (e.g., Chabrier & Baraffe, 2000).

With the discovery of a low mass companion to the white dwarf GD 165 Zuckerman & Becklin (1987) the first object that did not fit into the scheme of classical stellar types was found. It lacked the strength of metal oxide features that are typical for the M type. Yet, it was obviously not an old Jovian planet, since it was far too bright and lacked the strong methane and ammonia absorption features. With growing numbers of detections of such objects, the new spectral type L was introduced Basri (2000). Already for the earliest L type objects, the metal hydride and oxide bands disappear because of the increasing rate of condensation and rain-out of the corresponding elements. The influence of the dust cloud on the structure of the atmosphere and the emerging spectrum is strongest for the mid-L type (e.g., Witte et al., 2011). According to evolutionary models (e.g., Baraffe et al., 2003), the stellar main sequence for near-solar element abundances ends at the early L spectral types. Later types are populated by objects that lack the mass for lasting and stable hydrogen burning. Thus, the L type corresponds to the transition from stellar to substellar objects. As the first discovered L dwarfs, GD 165B (L4 according to Kirkpatrick, 2005) might possibly represent the first observed brown dwarf (Becklin & Zuckerman, 1988).



In the later L subtypes, the gas pressure becomes high enough so that H_2O and CH_4 form in favor of CO (e.g., Allard & Hauschildt, 1995). The influence of the methane is emphasized by the disappearance of the silicate dust clouds, which suddenly allows to view considerably deeper into the atmosphere. This causes significant changes in the spectral appearance, hence, the end of the L spectral type. These methane-rich objects are classified as T dwarfs (e.g., Burgasser et al., 2002a). Cooler atmospheres than those of T dwarfs will exhibit NH_3 . The spectra of such objects are slowly approaching the appearance known from giant planets like Jupiter. So far, no such objects, designated Y dwarfs, have been observed.

The dust model: The importance of dust clouds in the atmospheres of late type stars and brown dwarfs was first noted by Lunine et al. (1986). The first atmosphere models involving dust simulation were presented by Tsuji et al. (1996), soon followed the first observational evidence for atmospheric dust clouds (Noll et al., 1997; Jones & Tsuji, 1997). As a result, a number of groups focused on atmosphere modelling have introduced their own dust models (Burrows & Sharp, 1999; Allard et al., 2001; Ackerman & Marley, 2001; Cooper et al., 2003; Woitke & Helling, 2003). An overview of the various models was given by Dehn (2007) while a direct comparison has been published by Helling et al. (2008a).

Dehn (2007) was responsible for the integration of the dust model code of Helling et al. (2008c) with the general-purpose atmosphere code by Hauschildt & Baron (1999). Work with the resulting DRIFT-PHOENIX model was continued by Witte (2008). Since then, the models were studied extensively. Theoretical work involving the DRIFT-PHOENIX models are Helling et al. (2008b); Johnas et al. (2008b,a); Seifahrt et al. (2009); Witte et al. (2009a,b, 2011); Helling et al. (2011). Likewise, a number of tests on observational data have been carried out (Helling et al., 2008b; Neuhäuser et al., 2009; Schmidt et al., 2008; Burgasser et al., 2009; Dupuy et al., 2010; Lafrenière et al., 2011).

Aims and outline: First of all, the theoretical background and assumptions of atmosphere models are discussed briefly in Sec. 2. In Sec. 3, the fundamental processes that affect dust particles in the atmospheres of interest are derived individually, followed by the introduction of rate equations and necessary simplifications. Thereafter, an overview of the model code is given in Sec. 4, including recent improvements. Section 5 studies various aspects of the resulting grid of model atmospheres with an eye towards necessary model improvements. In the subsequent Sec. 6, these models are tested on observations in order to evaluate the ability to reproduce observations. Based on the conclusions summarized in Sec. 7, modified dust models are derived in Sec. 8 in order to overcome the most serious issues of the modelling approach. The work is concluded with an overview of follow-up work (Sec. 9).

2 Theoretical Approach: Atmospheres

In the following, the fundamental processes and their theoretical background are explained in order to give a brief overview about the problem to be solved. Unless stated otherwise, the descriptions of the basics and the radiative transfer follow Rutten (2003), Mihalas (1970, 1978), Unsöld (1955), while the chemistry section relies on Smith & Missen (1982) and the dust sections are based on Voitke & Helling (2003, 2004), Helling & Voitke (2006), Gail & Sedlmayr (1988) and Nolting (2004).

2.1 Prerequisites

The intensity I_λ of a beam of light into a propagation direction \vec{n} is defined by the amount of energy dE within a wavelength interval $d\lambda$ which passes through a surface element dA into the solid angle $d\omega$ per time dt :

$$dE = I_\lambda(\vec{r}, \vec{n}, t) \left(d\vec{A} \cdot \vec{n} \right) d\lambda d\omega dt \quad (2.1)$$

Per definition, the intensity is a function of site, direction of view and time. The mean intensity J_λ is defined as the local angle average of the intensity:

$$J_\lambda(\vec{r}, t) = \frac{1}{4\pi} \oint I_\lambda(\vec{r}, \vec{n}, t) d\omega \quad (2.2)$$

Furthermore, the net of projected intensity into direction \vec{n} is described by the flux F_λ :

$$\vec{F}_\lambda(\vec{r}, t) = \oint I_\lambda(\vec{r}, \vec{n}, t) \vec{n} d\omega \quad (2.3)$$

The solid angle are resolved by $d\omega = \cos\theta d\theta d\phi$. Assuming an invariance of the intensity with respect to ϕ , the problem can be reduced to a single angular dimension. The polar angle is typically expressed through $\mu = \cos\theta$.

Passing any kind of material, a beam of light will interact with the present particles. With respect to the intensity in a given wavelength interval, the beam can experience an increase through emission or a weakening through absorption. Furthermore, photon scattering or redistribution to/from other wavelength intervals contributes to the intensity. For a distance ds along a photon path and the coefficients η_λ (emission (see Sec. 2.3)), κ_λ (absorption) and σ_λ (scattering), the change of intensity dI_λ is:

$$dI_\lambda = (\eta_\lambda - (\kappa_\lambda + \sigma_\lambda)I_\lambda) ds \quad (2.4)$$



On the macroscopic scale, the absorption and scattering coefficients are typically merged into the extinction $\chi_\lambda = \kappa_\lambda + \sigma_\lambda$. The optical thickness τ_λ is defined by the integration of the extinction along a beam segment:

$$d\tau_\lambda = -\chi_\lambda ds \quad (2.5)$$

By integrating radially from infinity to the core of a stellar object, the optical thickness allows for a definition of a depth scale of the atmosphere. Employing diverse forms of weighting, it is also common to have non-monochromatic definitions of the optical depth.

Aside from radiation, convection is another important way to transport energy. A fluctuation that moves a hot mass element to an environment of slightly lower pressure may already be sufficient to trigger a convective process. By such a shift, the mass element expands as it remains in hydrostatic equilibrium with its environment. This expansion of the mass element reduces its density. Therefore, it will experience a buoyant force if the expansion has reduced its density below that of the surrounding gas. If not, it will simply be pushed back into its original environment. This mechanism is most efficient for nearly adiabatic processes because a fast exchange of thermal energy with the environment would reduce the resulting density effect. At some point, the buoyancy will stop and the mass element decays, thereby distributing its energy over its new environment. In a similar fashion, a cold mass element can sink into hotter environments. In order to determine whether a plasma will start convection, one compares the temperature gradients for the entirely radiative case (R) and the adiabatic expansion scenario (A). Assuming an ideal gas of temperature T and pressure p , this can be transformed into the Schwarzschild criterion:

$$\left(\frac{d \ln T}{d \ln p}\right)_R > \left(\frac{d \ln T}{d \ln p}\right)_A \quad (2.6)$$

For one-dimensional or time-independent simulations, one still relies on the rather simple mixing length theory (Prandtl, 1925; Biermann, 1932) for an approximation of the convective motion. Therein, the mean distance after which hot and cool mass elements dissipate or absorb thermal energy is called mixing length and serves as a free parameter. Under these conditions, it is possible to derive a mean convective velocity v_{conv} and a related convective flux F_{conv} (see Mihalas, 1970, p. 202ff).

2.2 Stellar atmospheres

Even in their youth, stars and substellar objects evolve only slowly over timescales of millions of years or more. Compared to that, the radiative, hydrodynamic and chemical timescales are tiny. Because of this, it is a reasonable assumption that such objects are in a state of hydrostatic equilibrium at any given time. Due to the implied time independence, a model can be simplified considerably by assuming a conservation of energy flux, chemical elements and charge. Disregarding effects of stellar rotation, the hydrostatic equilibrium further implies an independence of the polar and azimuthal angles, resulting in a purely altitude-dependent atmosphere structure. Under these conditions, the energy transfer is

constrained by:

$$\frac{d}{dz}(F_{\text{conv}} + F_{\text{rad}}) = 0 \quad (2.7)$$

where z denotes the altitude within the atmosphere and $F_{\text{rad}} = \int_0^\infty F_\lambda d\lambda$. In this case, the actual amount of the total emergent flux is typically expressed through the definition of an effective temperature T_{eff} (Stefan-Boltzmann law):

$$F_{\text{conv}} + F_{\text{rad}} = \sigma T_{\text{eff}}^4 \quad (2.8)$$

Assuming that the local gas pressure is mostly unaffected by radiation and turbulence, the following basic hydrostatic equation can be derived by applying Eq. 2.5 to Bernoulli's equation:

$$\frac{dp}{d\tau_\lambda} = \frac{g}{\chi_\lambda}, \quad (2.9)$$

where p denotes the local gas pressure and g represents the local gravitational acceleration.

Brown dwarfs and hot giant planets typically feature a compact, geometrically thin atmosphere compared to their radius. This permits a further simplification in form of a plane-parallel geometry.

The stratification of stellar and substellar atmospheres is maintained by a radiation field, which is powered by release of nuclear or gravitational energy and possibly irradiation, and in some cases also by degenerate electron gas.

The photons of a radiation field interact with the gas and excite the bound electrons. In turn, this feeds back on the radiation field, affects the chemistry and the thermodynamics of the atmosphere. In the most general case, it would be necessary to solve rate equations for all existing atomic and molecular states in order to determine a static solution which would have to be in statistical equilibrium with the chemistry and thermodynamics. Depending on the complexity of the atmospheric chemistry, i.e., the number of states to consider, the computational effort can rise very fast. Most often, this is avoided by assuming local thermodynamic equilibrium (LTE). It requires that the velocities of all gas and solid species within the local atmosphere are described by a Maxwell-Boltzmann distribution, i.e., all species have the same mean temperature. Also, LTE suggests that the atomic and molecular excitations can be approximated by a Saha-Boltzmann distribution for the same mean temperature. Any violation of these requirements means that at least a sub-ensemble of the local atmosphere is not in LTE. The implication by LTE is a sufficient rate of gas-gas and gas-photon interactions within the local atmosphere so that mean thermodynamic properties are able to establish. A way to further LTE is a high gas density, because it results in high interaction rates. However, this is not a sufficient condition. The radiation field has to be weak enough to have a negligible influence on the mean excitation state of the gas. Less dense and less optically thick atmospheric regions can result in a partial decoupling of the radiation field from the local gas. On the other hand, hot and dense atmospheric regions will support strong photon scattering which can result in significant NLTE effects, especially for non-coherent scattering.



Fortunately, the atmospheres of very low mass stars, brown dwarfs and giant planets all feature high gas densities and weak radiation fields. Furthermore, their comparably low temperatures result in much weaker excitation and photo ionization rates. Both of these effects provide a justification for assuming LTE as simplification. Those atmospheric layers, for which such an assumption is not substantiated, typically have only a weak influence on the emerging spectrum.

2.3 Radiative transfer

The fundamental *radiative transfer equation* 2.4 can be brought to the form:

$$\frac{dI_\lambda}{\chi_\lambda ds} = \frac{dI_\lambda}{d\tau_\lambda} = \frac{\eta_\lambda}{\chi_\lambda} - I_\lambda = S_\lambda - I_\lambda \quad (2.10)$$

with the source function S_λ representing the ratio of the emissivity and extinction coefficients. The equation is usually converted onto an optical depth scale. This way, provided that S_λ and the initial intensity $I_\lambda(\tau_i)$ are known, the radiative transfer equation (2.10) is solved formally by:

$$I_\lambda(\tau_f) = I_\lambda(\tau_i)e^{\tau_i - \tau_f} + \int_{\tau_i}^{\tau_f} S_\lambda(t)e^{t - \tau_f} dt \quad (2.11)$$

The variables τ_i and τ_f correspond to the initial and final optical depths at two distinct points along a beam. In the case of LTE and purely thermal interaction between the radiation field and the gas, the source function is equal to the Planck function $B_\lambda(T)$ for the local gas temperature T . Unfortunately, as soon as photon scattering is considered, the source function depends on the radiative field itself. For coherent scattering in LTE, the source function is:

$$\begin{aligned} S_\lambda &= \frac{\kappa_\lambda}{\kappa_\lambda + \sigma_\lambda} B_\lambda(T) + \frac{\sigma_\lambda}{\kappa_\lambda + \sigma_\lambda} J_\lambda \\ &= \epsilon_\lambda B_\lambda(T) + (1 - \epsilon_\lambda) J_\lambda \end{aligned} \quad (2.12)$$

The photon destruction parameter ϵ_λ describes thermal coupling rate.

A straightforward analytical solution of the radiative transfer is not possible with a source function that accounts for scattering because it depends on the intensity, i.e., the quantity that is being determined. The problem needs to be approached numerically. First of all, Eq. 2.11 is applied to Eq. 2.2. After separating the integral between outwards and inwards directed angles μ and consecutive application of

$$E_n(x) = \int_0^1 e^{-x/t} t^{-n} dt, \quad (2.13)$$

the description of the mean intensity is rewritten in form of the *Schwarzschild equation*:

$$J_\lambda = \frac{1}{2} \int_0^\infty S_\lambda E_1(|t - \tau|) dt \quad (2.14)$$

This is typically abbreviated by introducing the Λ operator:

$$J_\lambda = \Lambda S_\lambda \quad (2.15)$$

Together, Eqs. 2.12 and 2.15 can be converted into a simple scheme for solving the radiative transfer problem iteratively. However, such a simple approach does not lead to satisfying results, because the required number of iterations to reach an acceptable degree of convergence is proportional to $1/\epsilon_\lambda$. In other words, it does not converge numerically in scattering-dominated environments. A significant improvement was achieved through the operator splitting method introduced by Cannon (1973). It requires the split of Λ according to

$$\Lambda = \Lambda^* + (\Lambda - \Lambda^*) \quad (2.16)$$

Based on this new approximate Λ^* operator the final iterative scheme is given by:

$$J_{\lambda,n} = \Lambda^* S_{\lambda,n} + (\Lambda - \Lambda^*) S_{\lambda,n-1} \quad (2.17)$$

With an appropriate determination of Λ^* the number of required iterations drops considerably, which outweighs the increased calculational effort per iteration in terms of total runtime. Further details on proper Λ^* calculation have for instance been given by Hauschildt & Baron (1999).

2.4 Gas phase chemistry

Before the radiative transfer can be solved, the thermodynamics and the chemistry of the atmosphere must be known. For an atmosphere consisting of N gas species, made of M elements, the following conservation equation must be satisfied:

$$\begin{aligned} \sum_{j=1}^N a_{j,k} n_j &= b_k \quad k \in \mathbb{N}_{\leq M} \\ \equiv \mathbf{A} \mathbf{n} &= \mathbf{b} \end{aligned} \quad (2.18)$$

The coefficient a_{jk} represents the number of atoms of element k in gas species j , while n_j is the number of involved atoms/molecules of species j and b_k is the total number of elements k within the chemical system. The stoichiometric degree of freedom F is given by $F = N - \text{rank}(A)$. Given there are no further constraints on the chemistry, it represents the number of chemical reactions which can take place in a system. Each possible reaction j is attributed with a stoichiometric vector ν_j ($j \in \mathbb{N}_{\leq F}$), defined by:

$$\mathbf{A} \nu_j = \mathbf{0} \quad (2.19)$$



It describes the conservation of elements during the chemical reaction j by adding up the number of atoms of element k in all initial reactants and subtracting the number of atoms of element k in all final reactants. A chemical reaction is only possible if this sum equals zero for all elements k in the chemical system. In other words, each chemical reaction affects the composition of the gas but conserves the element abundances.

The equations are valid regardless of whether the system is at equilibrium. As the intention is to derive such an equilibrium state, the thermodynamical quantities are necessary constraints. The *Gibbs function* G is a function of the local gas pressure and temperature. Its complete differential for known entropy S , and volume V is:

$$dG = V dp - S dT + \sum_{i=1}^N \mu_i dn_i, \quad (2.20)$$

with the chemical potential $\mu_i = (dU/dn_i)_{S,V,j \neq i}$ and the internal energy U . In equilibrium, the Gibbs function is minimized. Assuming the system has sufficient time to relax to equilibrium, T and p are considered to be fixed. This results in the following equilibrium condition:

$$\sum_{i=1}^N \nu_{i,j} \mu_i = 0 \quad (2.21)$$

with the chemical potential μ_i . Provided that the chemical potentials and the initial composition of the system are known, this equation system provides the equilibrium composition. Typically, only reference values of the chemical potential are known. Hence, their exact value for a given temperature and partial pressure must be derived from the equation of state, which in case of an ideal gas is

$$\left(\frac{\partial \mu_i}{\partial p} \right)_{T, \mathbf{n}} = \frac{RT}{p} = v_i, \quad (2.22)$$

where R represents the ideal gas constant and v_i the partial volume of species i .

2.5 Stellar parameters

In addition to the effective temperatures, there are other major parameters describing stellar or substellar objects.

With age and mass, the surface gravity g of such stellar and substellar objects varies over several magnitudes. Hence, it is convenient to refer to a logarithmic scale in form of $\log(g)$ [$\text{cm} \cdot \text{s}^{-2}$]. This gravity is associated with a distinct radius within the atmosphere. For comparisons with observations, both values have to be chosen with care because the definition of the stellar radius is wavelength dependent and hence also the observed surface gravity. Fortunately, due to the geometrically thin photospheres in the low mass regime, such effects are negligible for this work.

The abundance of the elements within an atmosphere represent a large set of independent parameters. Unfortunately, it is hardly possible to determine individual abundances precisely. However, the abundances within the solar atmosphere are more or less well known. Assuming that the solar neighbourhood and to some lesser degree our whole galaxy has had a comparable nucleo-synthesis history, the abundance pattern of the sun should ideally apply to other objects of comparable age. For smaller relative deviations from the solar values, element abundances other than for helium and hydrogen are, then, simply scaled by a single parameter called metallicity $[M/H]$:

$$[M/H] = \log \frac{M/H}{M_{\odot}/H_{\odot}}, \quad (2.23)$$

with M/H representing the individual stellar element abundances relative to hydrogen and M_{\odot}/H_{\odot} being the respective ratio for the sun. For large deviations from solar abundances, as for instance for population II and III stars, a single parameter is no longer applicable.



3 Theoretical Approach: Clouds

Dust clouds as treated in our model are in a complicated equilibrium state between statistical collision rates that trigger chemical growth reactions, thermal evaporation, gas motion and gravitational drag (Fig. 3.1). The whole process starts with nucleation, i.e., polymerization of gas molecules. On top of these dust seeds, more complicated solids can form. The condensed material possesses a higher density than its environment. Hence the forming dust grains will precipitate into denser regions of the atmosphere. The deeper the grains fall into the atmosphere, the more efficient are nucleation and growth processes, resulting in larger grain sizes and number densities. The dust opacity rises strongly and scattering of radiation causes an immense backwarming effect. Eventually, the falling grains reach hotter environments that cause their evaporation. The material is returned to the gas phase. Observational evidence for stable dust clouds dictates the existence of a mechanism that mixes this material back into higher layers. Only this still hardly understood process produces stable dust clouds within the observationally accessible parts of the atmosphere.

In the following sections, the fundamental processes of dust clouds are formulated in order to derive the set of equations that was used in this work. The underlying formalism is based on Gail & Sedlmayr (1988), Woitke & Helling (2004) and Helling et al. (2008c). In contrast to these publications, a slightly different perspective on the problem is shown in order to derive the formalism more consistently.

3.1 Composition of dust grains and definition of the grain size distribution

The total number of solid species that are considered in the formation of dust grains is denoted by $S \in \mathbb{N}$. The index variable to address individual solid species is s . Each species consists of monomers, i.e., the smallest chemical units that constitute one point of the solid lattice. A monomer of species s is assumed to occupy a volume ΔV_s . Each solid s contributes the number N_s of monomers to the a grain. Hence, the complete grain composition is described by the vector $\vec{N}_s = (N_1, \dots, N_S) \in \mathbb{N}^S$ that points to one specific spot in the monomer space that is also referred to as composition space. As a matter of clarity, unity vectors $\vec{1}_s$ in direction of species s serve as increments in the monomer composition space.

For convenience, the monomer volumina are also expressed by a vector $\vec{\Delta V}_s \in \mathbb{R}^S$. This allows to multiply both vectors in order to calculate the total volume of a considered dust grain V :

$$V = \vec{N}_s \cdot \vec{\Delta V}_s = \sum_{s=0}^S N_s \cdot \Delta V_s \quad (3.1)$$

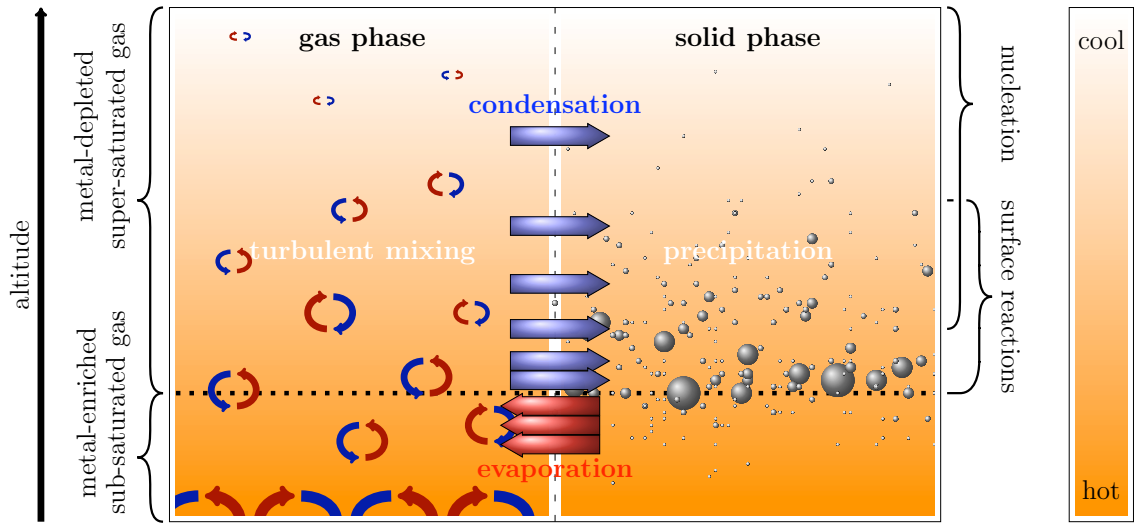


Figure 3.1: Rough sketch of the dynamic mechanism of dust formation.

The volume fraction b_s of species s is given by

$$b_s = \frac{V_s}{V} = \frac{N_s \cdot \Delta V_s}{V} \quad (3.2)$$

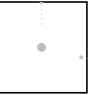
As an alternative to the composition vector \vec{N}_s , the grain is also adequately described by the combination of the volume V and the vector of all volume fraction \vec{b}_s .

Though both descriptions are equivalent, each has its individual advantages with respect to the derivation of model components. Initially, the composition \vec{N}_s is used for derivation of effective growth rate terms (Sec. 3.3ff), because this is a native problem in the monomer space. For the introduction of dust moments (Sec. 3.8) the grain volume V and the volume fractions \vec{b}_s are required.

A dust cloud is a spatially distributed accumulation of dust grains of various sizes and compositions. In other words, for every point in the space $\mathbb{R}^3 \times \mathbb{N}^S$ there is a distinct number density of dust particles. It is denoted by $f(\vec{N}_s, \vec{r})$ or, equivalently, by $f(V, \vec{b}_s, \vec{r})$ and is commonly referred to as grain size distribution function.

3.2 Nucleation rate

Molecules that possess stable monomers in the gas phase, can grow solids by simple polymerization. Hence, these species s form nuclei for subsequent growth of other species. The polymerization follows the most efficient reaction path in the isomer space. Along this path, the least efficient growth reaction determines the formation rate of new particles. All previous polymerization reactions have enough time to reach an equilibrium between growth and evaporation. Hence, there are always clusters waiting for a critical reaction to take place. Because all consecutive growth reactions are more efficient than their reverse reactions the clusters grow very fast past the least efficient reaction. Since the number of critical growth



reactions inhibits the number of all following reactions, it is sufficient to approximate the number density of the critical cluster n_s^* and its growth timescale $\tau_{n_s^*}^{\text{growth}}$ for the relevant solid species in order to determine the rate of dust particle formation J^* through polymerisation of gas molecules:

$$J^* = \sum_{s=0}^S J_s^* \approx \sum_{s=0}^S \frac{n_s^*}{\tau_{n_s^*}^{\text{growth}}} \quad (3.3)$$

The quantity J_s^* corresponds to the nucleation rate per species.

A more detailed discussion of the nucleation formalism can be found in Gail et al. (1984).

3.3 Collision and growth rates

In order to establish an equation for the growth of the dust grains it is necessary to determine the rate of collisions. For this task, a spherical grain of radius r and surface area $A = 4\pi r^2$ is assumed to move through a Maxwell-distributed single-species gas of temperature T , molecular mass m and number density n . The grain velocity is defined as v_d . Above each grain surface element $dA = r^2 \sin\theta d\theta d\phi$ each gas molecule has a velocity $\vec{v} = (v_x, v_y, v_z)$, where v_z is the component perpendicular to the grain surface. The inclination of v_d is given by the angle θ . Hence, the impact velocity of the molecule is $v_z - v_d \cos\theta$. Obviously, it must be larger than 0. The molecule number density times the impact velocity, times the probability of the molecule velocity and times the surface area element represents the local collision rate for molecules of a certain velocity. Integration over the whole grain surface and all permitted gas velocities results in the total collision rate c :

$$\begin{aligned} c &= \int_0^{2\pi} \int_0^\pi \int_{v_d \cos\theta}^\infty \int_{-\infty}^\infty \int_{-\infty}^\infty n \left(\frac{m}{2\pi kT} \right)^{3/2} e^{-\frac{m}{2kT}(v_x^2 + v_y^2 + v_z^2)} (v_z - v_d \cos\theta) r^2 \sin\theta dv_x dv_y dv_z d\theta d\phi \\ &= nA \left(\frac{kT}{2\pi m} \right)^{1/2} \cdot \left(1 + \sqrt{2} \cdot \sum_{n=1}^\infty \frac{\left(\frac{-mv_d^2}{2kT} \right)^{n+1}}{n!(2n+1)(2n+3)} \right) \end{aligned} \quad (3.4)$$

For resting grains, the equation simplifies considerably. The difference between both solutions is shown in Fig.3.2. Typically, the grains within brown dwarf atmospheres do not achieve significant fractions of the mean velocity of gas molecules. Only in the higher cloud layers, where velocities of the largest grains exceed 10^4 cm/s and the gas temperatures are low, the quantity $\frac{mv_d^2}{2kT}$ can exceed values of 0.3 for the heaviest of gas molecules. Even in those rare cases, the assumption of grains at rest causes less than five percent error in the rate. Therefore, it is reasonable to assume:

$$c = nA \left(\frac{kT}{2\pi m} \right)^{1/2} \quad (3.5)$$

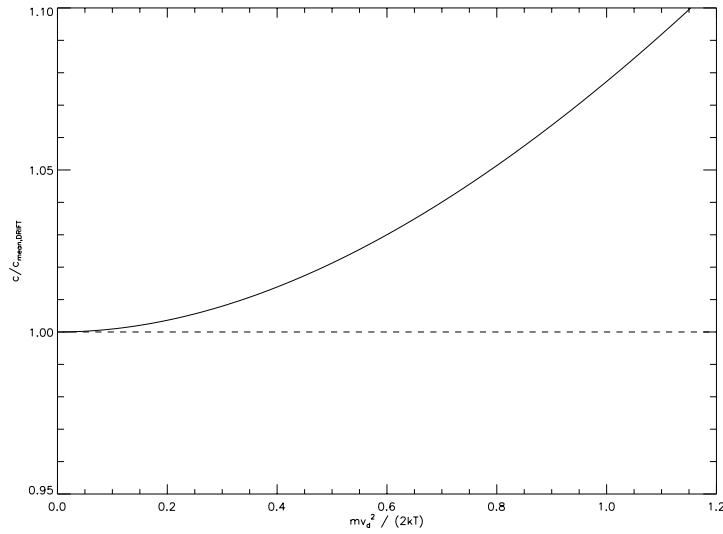


Figure 3.2: Collision rate of single-species gas molecules with moving grains in units of the rate for resting grains as a function of the squared velocity of the grain in units of the mean gas velocity.

A surface reaction is able to take place, as soon as all reactants are present at the grain surface (Fig. 3.3). The reactant of the lowest collision rate is called key reactant, because it determines the rate of chemical reactions. Presuming that all other reactants collide much

Surface reaction: Molecules in the gas phase are typically very simple. This is because the formation of more complex molecules requires multi-body reactions or complicated reaction schemes. Despite that, such molecules make up most of the solid species. By sticking to a pre-existing lattice structure, the phase space of chemical reactants is limited considerably. Hence, after a physical absorption of the reactants has taken place, chances for a chemical reaction are high. These reactions, following the adhesion to a surface, are referred to as surface reactions.

more often with the grain, their slots in the lattice structure of the respective solid islands can be assumed to be fully occupied. Hence, following its physical absorption, a key molecule is faced by numerous empty lattice points for a chemical reaction. This ensures that the thermal random walk of the reactant results in a chemical reaction almost instantly. Due to the higher collision rate of the other reactants, the adjacent lattice points are immediately occupied. Therefore, it is reasonable to approximate growth rates for individual solid species through the lowest collision rate of all involved molecules per contributing chemical reaction. The total growth rate of the monomer number N_s of a certain solid species s is given by the sum over the key reactant collision rates of all considered chemical reactions r_s :

$$\left. \frac{dN_s}{dt} \right|_{\text{growth}} = \sum_{r_s=0}^{R_s} c_{r_s}(n_{r_s,\text{key}}, m_{r_s,\text{key}}) \cdot \alpha_{r_s} \quad (3.6)$$

where $n_{r_s,\text{key}}$ and $m_{r_s,\text{key}}$ correspond to the number density and molecular mass of the key



reactant of reaction r of species s . The sticking parameter $\alpha_{r_s} \in [0, 1]$ is introduced to account for collisions which do not result in a physical absorption of the key reactant. In the model, it is treated as unity value due to a lack of laboratory data. If one grain of composition \vec{N}_s grows by one monomer $\vec{1}_s$, the local grain number density $f(\vec{N}_s, \vec{r})$ is reduced. On the other hand, the growth of a grain of composition $(\vec{N}_s - \vec{1}_s)$ increases the local number density. Therefore, the gradient of the grain number density is given by

$$\frac{\partial f(\vec{N}_s, \vec{r})}{\partial \vec{N}_s} = f(\vec{N}_s - \vec{1}_s, \vec{r}) - f(\vec{N}_s, \vec{r}) \quad (3.7)$$

and the product of this gradient and the collision rate (Eq. 3.6) results in the total, local growth rate of a dust grain of composition \vec{N}_s :

$$\begin{aligned} \left. \frac{\partial f(\vec{N}_s, \vec{r})}{\partial \vec{N}_s} \frac{d\vec{N}_s}{dt} \right|_{\text{growth}} &= \sum_{s=0}^S \sum_{r_s=0}^{R_s} \left(f(\vec{N}_s - \vec{1}_s, \vec{r}) A(\vec{N}_s - \vec{1}_s) - f(\vec{N}_s, \vec{r}) A(\vec{N}_s) \right) \\ &\quad \cdot n_{r_s, \text{key}} \left(\frac{kT}{2\pi m_{r_s, \text{key}}} \right)^{1/2} \cdot \alpha_{r_s} \\ &\approx \sum_{s=0}^S \sum_{r_s=0}^{R_s} \left(A(\vec{N}_s - \vec{1}_s) - A(\vec{N}_s) \right) \cdot f(\vec{N}_s, \vec{r}) \\ &\quad \cdot n_{r_s, \text{key}} \left(\frac{kT}{2\pi m_{r_s, \text{key}}} \right)^{1/2} \cdot \alpha_{r_s} \end{aligned} \quad (3.8)$$

Solid islands: Solids typically do not grow as a homogenous composite but as cluster into so-called “islands” because such a configuration minimizes the tension of the lattice structure. However, thermal excitation can result in a redistribution of lattice molecules and can cause a homogenous distribution of solid islands.

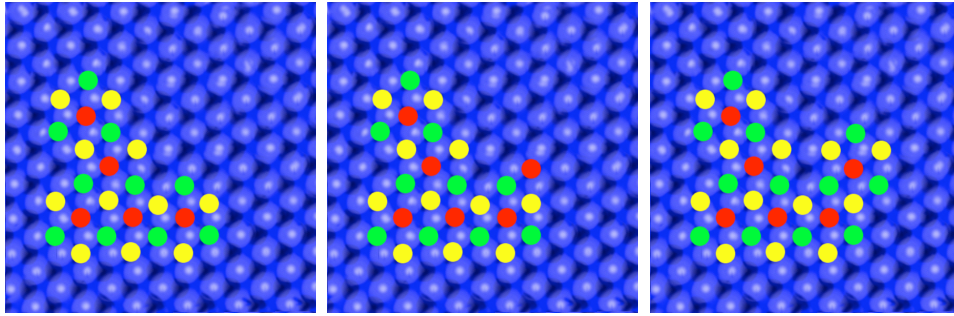


Figure 3.3: A solid island on the grain surface (*blue*). *left panel:* The key reactant lattice points (*red*) are completely enclaced by the more abundant reactants (*yellow/green*) at the grain surface. *center panel:* None of the other involved molecules is able to attach itself to the island before another key reactant is bonded. *right panel:* Once a key reactant is attached, the adjacent lattice points are immediately filled by other reactants. Hence, the key reactant governs the growth rate of the solid.

The equation was simplified by assuming an almost flat grain size distribution ($f(\vec{N}_s - \vec{1}_s, \vec{r}) \approx f(\vec{N}_s, \vec{r})$), which is valid for sufficiently large grains (Helling & Woitke, 2006).

3.4 Evaporation rates

The evaporation rate of a solid species is the product of its surface area and the dissociation probability of the monomers. Gauger et al. (1990) have shown that it can be expressed through its reversal, i.e., the grain growth, multiplied by the reciprocal supersaturation ratio and a number of departure coefficients. Further simplifying the problem by adopting thermodynamic and chemical equilibrium reduces the number of such coefficients to one (e.g., Helling & Woitke, 2006), namely the grain surface fraction of the considered solid species. Both simplifications are well justified. On one hand, small dust grains forming in the atmospheres of interest typically deviate less than 3.5K from surrounding gas temperatures (Woitke & Helling, 2003). On the other hand, compared to the long timescales of dust formation in these atmospheres, the gas phase itself is always at chemical equilibrium and it is in a statistical equilibrium with the solid phase.

Assuming thermal diffusion of the solid islands (Woitke & Helling, 2004), the surface fraction of solid s is approximately its volume fraction b_s . The monomer number growth rate is then:

$$\begin{aligned} \left. \frac{dN_s}{dt} \right|_{\text{evaporation}} &= - \sum_{r_s=0}^{R_s} c_{r_s}(n_{r_s,\text{key}}, m_{r_s,\text{key}}) \cdot \alpha_{r_s} \cdot \frac{A_s(\vec{N}_s - \vec{1}_s)}{S_{r_s} A(\vec{N}_s - \vec{1}_s)} \\ &= - \sum_{r_s=0}^{R_s} c_{r_s}(n_{r_s,\text{key}}, m_{r_s,\text{key}}) \cdot \alpha_{r_s} \cdot \frac{b_s(\vec{N}_s - \vec{1}_s)}{S_{r_s}}, \end{aligned} \quad (3.9)$$

where S_{r_s} corresponds to the effective supersaturation ratio (see Helling & Woitke, 2006) of solid species s with respect to reaction r_s . The quantity A_s denotes the grain surface area occupied by species s .

As was done for the growth rate in the previous section, the grain number density gradient in cluster space is multiplied by the evaporation rate in order to derive the total, local evaporation rate:

$$\begin{aligned} \left. \frac{\partial f(\vec{N}_s, \vec{r})}{\partial \vec{N}_s} \frac{d\vec{N}_s}{dt} \right|_{\text{evaporation}} &= - \sum_{s=0}^S \sum_{r_s=0}^{R_s} \left(f(\vec{N}_s + \vec{1}_s, \vec{r}) A_s(\vec{N}_s) - f(\vec{N}_s, \vec{r}) A_s(\vec{N}_s - \vec{1}_s) \right) \\ &\quad \cdot n_{r_s,\text{key}} \left(\frac{kT}{2\pi m_{r_s,\text{key}}} \right)^{1/2} \cdot \frac{\alpha_{r_s}}{S_{r_s}} \quad (3.10) \\ &\approx \sum_{s=0}^S \sum_{r_s=0}^{R_s} \left(A_s(\vec{N}_s) - A_s(\vec{N}_s - \vec{1}_s) \right) \cdot f(\vec{N}_s, \vec{r}) \\ &\quad \cdot n_{r_s,\text{key}} \left(\frac{kT}{2\pi m_{r_s,\text{key}}} \right)^{1/2} \cdot \frac{\alpha_{r_s}}{S_{r_s}} \end{aligned}$$



With respect to solid species s , evaporation of grains of composition \vec{N}_s reduces the local number density $f(\vec{N}_s, \vec{r})$ while the evaporation of grains of composition $(\vec{N}_s + \vec{1}_s)$ increase it.

3.5 Effective growth rate

Combining the growth and evaporation rates results in:

$$\begin{aligned}
& \frac{\partial f(\vec{N}_s, \vec{r})}{\partial \vec{N}_s} \frac{d\vec{N}_s}{dt} \\
&= \left. \frac{\partial f(\vec{N}_s, \vec{r})}{\partial \vec{N}_s} \frac{d\vec{N}_s}{dt} \right|_{\text{growth}} + \left. \frac{\partial f(\vec{N}_s, \vec{r})}{\partial \vec{N}_s} \frac{d\vec{N}_s}{dt} \right|_{\text{evaporation}} \\
&= \sum_{s=0}^S \sum_{r_s=0}^{R_s} A(\vec{N}_s - \vec{1}_s) \left(1 - \frac{b_s(\vec{N}_s - \vec{1}_s)}{S_{r_s}} \right) \cdot f(\vec{N}_s, \vec{r}) \cdot n_{r_s, \text{key}} \left(\frac{kT}{2\pi m_{r_s, \text{key}}} \right)^{1/2} \cdot \alpha_{r_s} \\
&- \sum_{s=0}^S \sum_{r_s=0}^{R_s} A(\vec{N}_s) \left(1 - \frac{b_s(\vec{N}_s)}{S_{r_s}} \right) \cdot f(\vec{N}_s, \vec{r}) \cdot n_{r_s, \text{key}} \left(\frac{kT}{2\pi m_{r_s, \text{key}}} \right)^{1/2} \cdot \alpha_{r_s} \\
&= \sum_{s=0}^S J_s(\vec{N}_s, \vec{r}) - J_s(\vec{N}_s + \vec{1}_s, \vec{r}) \tag{3.11}
\end{aligned}$$

The terms have been rearranged in order to distinguish the effective exchange rates of grains of composition \vec{N}_s with the next smaller grains $(\vec{N}_s - \vec{1}_s)$ and with the next larger grains $(\vec{N}_s + \vec{1}_s)$. These rates are abbreviated by $J_s(\vec{N}_s, \vec{r})$ and $J_s(\vec{N}_s + \vec{1}_s, \vec{r})$, respectively.

For later use, a number of algebraic manipulations of the effective growth rate are necessary. First of all, the grain size distribution is converted from composition space formulation $(f(\vec{N}_s, \vec{r}))$ to its volume fraction form $(f(V, \vec{b}_s, \vec{r}))$. In addition, the problem is simplified by assuming that all grains around \vec{r} have identical volume fractions \vec{b}_s . Instead of one growth rate per point in the volume fraction space (\mathbb{R}^S) only a single point has to be considered this way. The remaining dimension of the problem is the grain volume V .

Using these simplifications in Eq. 3.11, followed by multiplication of the equation with $V_i^{j/3}$ and consecutive summation over the grain volume interval $[V_l, V_u]$ in steps of $\Delta V_s = V_{i+1} - V_i$ for $i \in \mathbb{N}$ provides:

$$\begin{aligned}
\sum_{i=l}^{u-1} \frac{\partial f(V_i, \vec{r})}{\partial \vec{V}_s} \frac{d\vec{V}_s}{dt} V_i^{j/3} (V_{i+1} - V_i) &= \sum_{i=l}^{u-1} \sum_{s=0}^S (J_s(V_i, \vec{r}) - J_s(V_{i+1}, \vec{r})) V_i^{j/3} (V_{i+1} - V_i) \\
&= \sum_{s=0}^S J_s(V_l, \vec{r}) V_l^{j/3} (V_{l+1} - V_l) \\
&- \sum_{s=0}^S J_s(V_u, \vec{r}) (V_u - \Delta V_s)^{j/3} (V_u - V_{u-1}) \tag{3.12} \\
&+ \sum_{i=l}^{u-2} \sum_{s=0}^S J_s(V_{i+1}, \vec{r}) (V_{i+1}^{j/3} - V_i^{j/3}) (V_{i+1} - V_i)
\end{aligned}$$

Assuming $\Delta V_s \ll V_i$, the term $V_{i+1}^{j/3} - V_i^{j/3} = (V_i + \Delta V_s)^{j/3} - V_i^{j/3}$, as a function of V_i , is approximated by a first order Taylor expansion around $\Delta V_s = 0$. Also, the sum is transformed into an integral by $(V_i - V_{i-1}) \rightarrow dV \approx 0$. The terms $(V_{l+1} - V_l)$ and $(V_u - V_{u-1})$ both correspond to ΔV_s . This yields the required expression for the integrated effective growth rate:

$$\int_{V_i}^{V_u} \frac{\partial f(V, \vec{r})}{\partial \vec{V}_s} \frac{d\vec{V}_s}{dt} V^{j/3} dV = \sum_{s=0}^S J_s(V_l, \vec{r}) V_l^{j/3} \Delta V_s - \sum_{s=0}^S J_s(V_u, \vec{r}) (V_u - \Delta V_s)^{j/3} \Delta V_s \quad (3.13)$$

$$+ \frac{j}{3} \int_{V_i}^{V_u} \sum_{s=0}^S J_s(V + \Delta V_s, \vec{r}) \Delta V_s V^{j/3-1} dV = \left(f(V_l, \vec{r}) V_l^{j/3} - f(V_u, \vec{r}) (V_u - \Delta V_s)^{j/3} \right) \sum_{s=0}^S \chi_s(\vec{r}) \Delta V_s + \frac{j}{3} \chi_{\text{net}}(\vec{r}) \int_{V_i}^{V_u} f(V, \vec{r}) V^{(j-1)/3} dV \quad (3.14)$$

The net growth velocity χ_{net} and the species-dependent growth velocity χ_s are

$$\chi_{\text{net}}(\vec{r}) = \sum_{s=0}^S \chi_s(\vec{r}) = \sqrt[3]{36\pi} \cdot \sum_{s=0}^S \sum_{r_s=0}^{R_s} n_{r_s, \text{key}} \alpha_{r_s} \Delta V_s \cdot \left(\frac{kT}{2\pi m_{r_s, \text{key}}} \right)^{1/2} \left(1 - \frac{b_s}{S_{r_s}} \right). \quad (3.15)$$

3.6 Equation of motion

Being formed in a sufficiently dense gas, dust grains will not remain where they have formed but instead will be dragged along by gas flows. Furthermore, the solid grains have a much higher density than their environment, resulting in their gravitational precipitation. In general, a strong radiative field may also have a considerable influence on the grain motion. However, in the late type dwarf objects of interest, the radiation is typically too weak to necessitate its consideration for the solution of the equation of motion (Woitke & Helling, 2003).

Depending on its velocity, size and shape as well as the density and viscosity of its environment, a grain will sustain a certain frictional force that effectively reduces the acceleration by gravity. Simulations by Woitke & Helling (2003) have shown that the Knudsen number, i.e., the ratio of the mean free path of the grains and the grain radius, is typically large in late type dwarf atmospheres. Only on rare occasions, individual particles may violate this criterion. Similarly, theoretical results have shown that the grains remain far below the speed of sound throughout the observationally relevant layers of these atmospheres. For



both reasons, the characteristics of a subsonic free molecular flow are applicable. Also, the assumption of force equilibrium is justified because it is reached on very short fall distances. On this basis the equation of motion is solved to determine the relative drift velocity v_{drift} between a spherical dust grain of volume V and density ρ_d and its surrounding gas of density ρ , mean molecular mass $\bar{\mu}$ and temperature T :

$$\vec{v}_{\text{drift}} = \underbrace{\sqrt[3]{\frac{3}{4\pi}} \vec{g}}_{\xi} \frac{\rho_d}{\rho} \underbrace{\sqrt{\frac{\pi \bar{\mu}}{8kT}}}_{\frac{1}{c_{th}}} V^{1/3} \quad (3.16)$$

The local gravitational acceleration is denoted by \vec{g} , while k is the Boltzmann constant. The characteristic gravitational acceleration ξ and the mean thermal gas particle velocity c_{th} serve as abbreviations. The drift velocity \vec{v}_{drift} describes only the relative velocity between dust and gas. It is further necessary to take into account the flow of gas \vec{v}_g , which drags along the dust grains, in order to consider the full grain motion \vec{v}_d :

$$\vec{v}_d = \vec{v}_g + \vec{v}_{\text{drift}} \quad (3.17)$$

In the time-dependent case, the gas velocity results from hydrodynamical simulations.

3.7 Flow rate

In order to estimate the local number density of dust grains of a certain size, it is necessary to track the exchange rates between adjacent volume elements (hereafter *voxels*) of the atmosphere. The net flow for grains of composition \vec{N}_s into and out of a voxel is given by:

$$\Phi(\vec{N}_s, \vec{r}) = \oint f(\vec{N}_s, \vec{r}) \vec{v}_d(\vec{r}) \cdot \vec{n}_{A_v}(\vec{r}) dA_v(\vec{r}), \quad (3.18)$$

where A_v denotes the surface of the voxel at \vec{r} and \vec{n}_{A_v} its normal vector. The velocity \vec{v} refers to the average velocity of grains of composition \vec{N}_s into and out of the voxel of interest. It must be noted that the considered velocities at the adjacent voxels are sign sensitive, in this respect. Only if an actual inflow occurs from an adjacent voxel, it affects the dust particle number of the considered voxel. On the other hand, the velocity inside the considered voxel determines the sides through which grains are moving out.

By dividing the net flow by the voxel volume dV_v , the lost/gained grains are distributed throughout the voxel, resulting in an expression for the local flow rate:

$$\frac{\partial f(\vec{N}_s, \vec{r})}{\partial \vec{r}} \frac{d\vec{r}}{dt} = \frac{d\Phi(\vec{N}_s, \vec{r})}{dV_v(\vec{r})} \quad (3.19)$$

Presuming a Cartesian grid, the voxel volume is given by $dV_v = dx \cdot dy \cdot dz$ and the velocity of the dust is given by $\vec{v}_d = (v_{d,x}, v_{d,y}, v_{d,z})$. The surface area of the voxel is segmented into

six faces, which separates the flow rate into six simple terms and eliminates the integral:

$$\begin{aligned}
 \frac{\partial f(\vec{N}_s, \vec{r})}{\partial \vec{r}} \frac{d\vec{r}}{dt} &= \frac{d}{dx} \left(f(\vec{N}_s, \vec{r} - \vec{1}_x/2) \cdot v_{d,x}(\vec{r} - \vec{1}_x/2) \right) \\
 &\quad - \frac{d}{dx} \left(f(\vec{N}_s, \vec{r} + \vec{1}_x/2) \cdot v_{d,x}(\vec{r} + \vec{1}_x/2) \right) \\
 &\quad + \frac{d}{dy} \left(f(\vec{N}_s, \vec{r} - \vec{1}_y/2) \cdot v_{d,x}(\vec{r} - \vec{1}_y/2) \right) \\
 &\quad - \frac{d}{dy} \left(f(\vec{N}_s, \vec{r} + \vec{1}_y/2) \cdot v_{d,y}(\vec{r} + \vec{1}_y/2) \right) \\
 &\quad + \frac{d}{dz} \left(f(\vec{N}_s, \vec{r} - \vec{1}_z/2) \cdot v_{d,x}(\vec{r} - \vec{1}_z/2) \right) \\
 &\quad - \frac{d}{dz} \left(f(\vec{N}_s, \vec{r} + \vec{1}_z/2) \cdot v_{d,z}(\vec{r} + \vec{1}_z/2) \right)
 \end{aligned} \tag{3.20}$$

A formulation for spherical geometry has been derived and is given in Sec. 8.3.

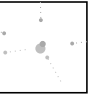
Gravitational settling: In a static vertical 1D case, whether plane-parallel or spherical, the velocity field \vec{v} is zero in the tangential planes. Further assuming there is no upstream, the grain motion is caused entirely by the gravity. As result, only an inflow from above and an outflow to the next lower layer must be considered at every height and the number density fractions of the motion are unity:

$$\begin{aligned}
 \left. \frac{\partial f(\vec{N}_s, \vec{r})}{\partial \vec{r}} \frac{d\vec{r}}{dt} \right|_{\text{gravity}} &= \frac{f(\vec{N}_s, \vec{r} + \vec{1}_z/2) v_{\text{drift}}(\vec{r} + \vec{1}_z) - f(\vec{N}_s, \vec{r} - \vec{1}_z/2) v_{\text{drift}}(\vec{r} - \vec{1}_z/2)}{\Delta z} \\
 &= \frac{\partial}{\partial z} \left(f(\vec{N}_s, \vec{r}) v_{\text{drift}}(\vec{r}) \right)
 \end{aligned} \tag{3.21}$$

For later use, the flow rate due to gravitational settling is multiplied by $V^{j/3}$ and integrated over the volume interval $[V_l, V_u]$. The grain volume is invariant with respect to the altitude and, hence, is drawn into the differential quotient. This permits to exchange the order of the integral and the derivation:

$$\begin{aligned}
 \int_{V_l}^{V_u} \left. \frac{\partial f(\vec{N}_s, \vec{r})}{\partial z} \frac{d\vec{r}}{dt} \right|_{\text{gravity}} V^{j/3} dV &= \frac{d}{dz} \int_{V_l}^{V_u} f(\vec{N}_s, \vec{r}) \cdot v_{\text{drift}}(\vec{r}) V^{j/3} dV \\
 &= \xi \frac{d}{dz} \left(\frac{\rho_d}{c_{th}\rho} \int_{V_l}^{V_u} f(\vec{N}_s, \vec{r}) \cdot V^{(j+1)/3} dV \right)
 \end{aligned} \tag{3.22}$$

The last step substituted the drift velocity according to Eq. 3.16 and presumed $\frac{d\xi}{dz} \approx 0$, which is reasonable for the geometrically thin atmospheres of very low mass stars and substellar objects.



Convective overshooting: In a time-independent 1D model, mixing length theory is employed to calculate convective motion. However, the momentum of convective bubbles does not vanish instantly at the edge to radiative zones but disperses slowly with distance to the convectively unstable region. Woitke & Helling (2004) approximated this overshooting by a local mixing timescale $\tau_{\text{mix}}(z)$:

$$\frac{\tau_{\text{mix}}(z)}{\tau_{\text{mix},0}} = \exp\left(\beta \cdot \max\left(0, \log \frac{p_0}{p(z)}\right)\right) \quad (3.23)$$

The reference mixing timescale $\tau_{\text{mix},0} = \frac{l}{H_p v_{\text{conv},0}}$ relies on the mixing length parameter l , the pressure scale height H_p and the convective velocity $v_{\text{conv},0}$ at the convection zone edge. Similarly, p_0 refers to the pressure at this reference point. The gradient of the timescale with respect to the gas pressure $p(z)$ is determined by the overshooting parameter β . Results by Ludwig et al. (2002) suggest a value of $\beta \approx 2.2$ (Woitke & Helling, 2004).

The continuous mass exchange represents an additional velocity field that affects the motion of the dust grains. Using Eqs. 3.18 and 3.19, the respective flow rate component is given by:

$$\left. \frac{\partial f(\vec{N}_s, \vec{r})}{\partial \vec{r}} \frac{d\vec{r}}{dt} \right|_{\text{overshooting}} = -\frac{f(\vec{N}_s, \vec{r})}{\tau_{\text{mix}}} \quad (3.24)$$

Combining the gravitational and overshooting flow terms, the final flow term of the model of this work is:

$$\frac{\partial f(\vec{N}_s, \vec{r})}{\partial \vec{r}} \frac{d\vec{r}}{dt} = \left. \frac{\partial f(\vec{N}_s, \vec{r})}{\partial \vec{r}} \frac{d\vec{r}}{dt} \right|_{\text{gravity}} + \left. \frac{\partial f(\vec{N}_s, \vec{r})}{\partial \vec{r}} \frac{d\vec{r}}{dt} \right|_{\text{overshooting}} \quad (3.25)$$

3.8 Dust rate equations

At this point, all prerequisites for setting up rate equations for the local number density $f(\vec{N}_s, \vec{r})$ of dust grains of composition \vec{N}_s at the coordinates \vec{r} :

$$\frac{df(\vec{N}_s, \vec{r})}{dt} = \frac{\partial f(\vec{N}_s, \vec{r})}{\partial \vec{N}_s} \frac{d\vec{N}_s}{dt} + \frac{\partial f(\vec{N}_s, \vec{r})}{\partial \vec{r}} \frac{d\vec{r}}{dt} \quad (3.26)$$

Unfortunately, it is not feasible to solve this equation for all possible grain compositions $\vec{N}_s \in \mathbb{N}^S$. A number of simplifications are necessary to estimate dust cloud quantities. First of all, it is convenient to substitute $f(\vec{N}_s, \vec{r}) = f(V, \vec{b}_s, \vec{r})$. Then, the individual grain compositions are ignored in favor of a more advantageous local average grain compositions. This way, only a single rate equation needs to be solved per grain size, instead of one per possible grain composition. Even then, the number of equations is not yet manageable. Therefore, the individual grain volumina have to be replaced with local integrated quantities. These dust moments L_j are defined by:

$$\rho L_j(\vec{r}) = \int_{V_i}^{\infty} f(V, b_s^{-1}, \vec{r}) V^{j/3} dV \quad [cm^{j-3}] \quad j \in \mathbb{N} \quad (3.27)$$

Below the lower integration limit V_l , grains growth is treated as a pure nucleation process independent from the rate equations. This distinction is possible because tiny clusters typically have a negligible fall velocity and their surface area is too small to permit strong growth through surface reactions. On the other hand, larger particles grow predominantly through surface reactions and not through polymerisation. There is no unique grain size where this transition occurs. A value is arbitrarily selected to be a thousand times of the $\text{TiO}_2[\text{s}]$ monomer volume. The exact value is more or less insignificant for the final cloud models, as long as it is not chosen too low, i.e., violating fundamental assumptions of the nucleation theory, or exceedingly high, neglecting efficient growth through surface reactions.

The dust moments represent integrated quantities (particle number, radius, surface area, volume,...) for all dust grains within a considered spatial volume element. For instance, L_0 represents the number of dust grains while L_3 represents the total dust volume per spatial volume element. From them, it is possible to derive local mean dust quantities: the number density n_d

$$n_d = \rho L_0 \quad [\text{cm}^{-3}], \quad (3.28)$$

the mean grain radius $\langle a \rangle$

$$\langle a \rangle = \sqrt[3]{\frac{3}{4\pi} \frac{L_1}{L_0}} \quad [\text{cm}], \quad (3.29)$$

the mean dust grain surface $\langle A \rangle$

$$\langle A \rangle = \sqrt[3]{36\pi} \frac{L_2}{L_0} \quad [\text{cm}^2] \quad (3.30)$$

and the mean dust particle volume $\langle V \rangle$

$$\langle V \rangle = \frac{L_3}{L_0} \quad [\text{cm}^3]. \quad (3.31)$$

With the definition of dust moments, the rate equation (Eq. 3.26) can be converted into a new form. For this, the equation is multiplied by $V^{j/3}(\vec{N}_s)$. Consecutively, it is integrated over V between V_l and V_u . Inserting Eqs. 3.14, 3.22, 3.24 and 3.25 provides:

$$\begin{aligned} \frac{d}{dt} \int_{V_l}^{V_u} f(V, z) V^{j/3} dV &= \left(f(V_l, z) V_l^{j/3} - f(V_u, z) (V_u - \Delta V_s)^{j/3} \right) \sum_{s=0}^S \chi_s(z) \Delta V_s \\ &+ \frac{j}{3} \chi_{\text{net}}(z) \int_{V_l}^{V_u} f(V, z) V^{(j-1)/3} dV \\ &+ \xi \frac{\partial}{\partial z} \frac{\rho_d}{c_{th} \rho} \int_{V_l}^{V_u} f(V, z) V^{(j+1)/3} dV - \frac{1}{\tau_{\text{mix}}} \int_{V_l}^{V_u} f(V, z) V^{j/3} dV \end{aligned} \quad (3.32)$$



As mentioned above, the exchange rate with grains of lower volume corresponds to the nucleation rate:

$$f(V_l, z) \sum_{s=0}^S \chi_s(z) \Delta V_s = J^* \quad (3.33)$$

Enforcing $u \rightarrow \infty$, the exchange rate with grains of higher volume vanishes due to:

$$\lim_{u \rightarrow \infty} f(V_u, \vec{r}) = 0 \quad (3.34)$$

Substituting the integrals for the dust moments turns Eq. 3.32 into the moment equations:

$$\frac{d}{dt} \rho L_j = \underbrace{V^{j/3} J^*}_{\text{nucleation}} + \underbrace{\frac{j}{3} \chi_{\text{net}}(z) \rho L_{j-1}}_{\text{growth/evaporation}} + \underbrace{\xi \frac{\partial}{\partial z} \left(\frac{\rho_d}{c_{th}} L_{j+1} \right)}_{\text{gravitational settling}} - \underbrace{\frac{\rho L_j}{\tau_{\text{mix}}}}_{\text{convective overshooting}} \quad (3.35)$$

3.9 Element rate equations

Dust growth removes elements out of the gas phase, which causes a self-regulation of the growth mechanism. Hence, the element conservation needs to be considered. Its derivation follows analogous reasoning as for dust particles. Nucleation and growth consume local gas elements while evaporation releases them. In addition gas motions such as convective overshooting mix the gas phase elements. The local concentration of element e in an undepleted atmosphere is denoted by $n_{e,0}$ while the actual local gas phase number density in the dust-bearing atmosphere is n_e . E is the set of all considered elements. Each chemical reaction r consumes a number of elements e equivalent to the stoichiometric coefficient for the resulting solid species. For nucleation processes this coefficient is given by ν_{e,p_s} . The corresponding value for surface reactions is ν_{e,r_s} . The maximum monomer number for nucleation before exceeding the limiting volume V_l is $N_{l,s}$. The resulting rate equation is:

$$\frac{dn_e}{dt} = \underbrace{\frac{n_{e,0} - n_e}{\tau_{\text{mix}}}}_{\text{convective overshooting}} - \underbrace{\sum_s \nu_{e,p_s} N_{l,s}}_{\text{nucleation}} - \underbrace{\rho L_2 \sum_s o_s}_{\text{growth/evaporation}} \quad (3.36)$$

with the abbreviation

$$o_s = \sum_{r_s} \sqrt[3]{36\pi} \cdot \nu_{e,r_s} n_{r_s, \text{key}} \alpha_{r_s} \left(\frac{kT}{2\pi m_{r_s, \text{key}}} \right)^{1/2} \quad (3.37)$$

3.10 Final system of equations

The dust moment equations (Eq. 3.35) describe the relations between the total particle number, the summed particle radii, the summed particle surface area, the summed particle volume and higher orders of summed spatial particle quantities of the dust grains within a specific atmosphere volume.

In order to determine a mean grain composition, additional equations are required. After introducing $2 \cdot S$ additional dust moments $L_{3,s} = \int_{V_l}^{\infty} f(\vec{N}_s, z) V_s dV_s$ and $L_{4,s} = L_4 \cdot L_{3,s} / L_3$ (Helling et al., 2008c), Eq. 3.26 is reformulated for a single solid species s . The relations $L_3 = \sum_{s=0}^S L_{3,s}$ and $L_4 = \sum_{s=0}^S L_{4,s}$ satisfy the conservation of the dust moments. Multiplication with V_s and consecutive integration results in the set of equations:

$$\frac{d}{dt} \rho L_{3,s} = V_l J_{l,s} + \chi_s \rho L_2 + \xi \rho_d \frac{\partial}{\partial z} \frac{L_{4,s}}{c_{th}} - \frac{\rho L_{3,s}}{\tau_{\text{mix}}} \quad (3.38)$$

The presence of L_2 is not a mistake because the full grain surface area contributes to the growth of species s and not only the respective surface fraction.

These new equations are sufficient to constrain the average grain composition. As a last point, a closure condition $L_0(L_1, L_2, L_3, L_4)$ in form of a double delta-peaked grain size distribution is defined (see Helling et al., 2008c), which is necessary because there are always two more dust moment involved than there are equations.

With the intention to derive a static dust cloud, the effective rates for dust and the gas have to be in equilibrium. Hence, the final system of moment and constraint equations is:

$$\begin{aligned} -\xi \frac{\partial}{\partial z} \left(\frac{\rho_d}{c_{th}} L_{j+1} \right) &= V_l^{j/3} J_l + \frac{j}{3} \chi_{\text{net}} \rho L_{j-1} - \frac{\rho L_j}{\tau_{\text{mix}}} \quad \forall j \in \{0, 1, 2\} \\ -\xi \frac{\partial}{\partial z} \left(\frac{\rho_d}{c_{th}} L_{4,s} \right) &= V_l J_{l,s} + \chi_{\text{net},s} \rho L_2 - \frac{\rho L_{3,s}}{\tau_{\text{mix}}} \quad \forall s \in S \\ \frac{n_{e,0} - n_e}{\tau_{\text{mix}}} &= \sum_s \nu_{e,p_s} N_{l,s} + \rho L_2 \sum_s o_s \quad \forall e \in E \end{aligned} \quad (3.39)$$

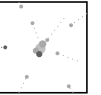
The current implementation considers 7 solid species ($S = \{\text{TiO}_2[s], \text{MgO}[s], \text{SiO}_2[s], \text{MgSiO}_3[s], \text{Mg}_2\text{SiO}_4[s], \text{Al}_2\text{O}_3[s], \text{Fe}[s]\}$) that are considered to form through 32 chemical reactions (see Witte et al., 2009a) and affect the gas phase abundances of 6 elements ($E = \{\text{O}, \text{Mg}, \text{Al}, \text{Si}, \text{Ti}, \text{Fe}\}$).

3.11 Dust opacity

The calculation of the dust opacity is carried out in two steps. First of all, an effective optical medium is determined for the composite grains. The solid islands within the dust grains are considered to be small compared to the grain size and are assumed to be homogeneously distributed. For such conditions, Maxwell's equations for non-magnetic and neutral conductive materials can be solved, provided that laboratory data of the refractive index for the pure solid species is available. The method used here for deriving an effective medium was introduced by Bosch et al. (2000):

$$\left| \sum_s \frac{V_s}{V_{\text{tot}}} \frac{m_s^2 - \bar{m}^2}{m_s^2 + 2\bar{m}^2} \right| = 0, \quad (3.40)$$

with m_s representing the complex refractive index of the pure species s and \bar{m} being the effective refractive index of the composite medium. The only additional constraint on the



solution is the non-negativity of the real and imaginary components of the refractive index as well as the imaginary component of the dielectric coefficient. This method follows the general outline of Bruggeman (1935) but avoids ambiguities due to back and forth conversions between the complex dielectric coefficients and the complex refractive index.

In the second step, *Mie theory* (Mie, 1908; Wolf & Voshchinnikov, 2004) is applied to determine the effective absorption efficiency Q_{abs} and the effective scattering efficiencies Q_{sca} of the spherical dust grain of volume V . It involves a solution of Maxwell's equations for absorption, re-emission and scattering of an electromagnetic field by homogenous non-magnetic uncharged conductive spheres made of the determined effective medium. By multiplying the determined efficiency coefficients with the geometric cross section ($\sqrt[3]{36\pi}V^{2/3}$ of a spherical grain of volume V , the effective cross-section for absorption and scattering are found. Integrated over the grain size distribution, the cross sections add up to the opacity:

$$\chi_{\text{dust}}(z) = \kappa_{\text{dust}}(z) + \sigma_{\text{dust}}(z) = \sqrt[3]{36\pi} \int_0^\infty (Q_{\text{abs}}(V, \vec{b}_s) + Q_{\text{sca}}(V, \vec{b}_s)) f(V, \vec{b}_s, z) V^{2/3} dV \quad (3.41)$$

Of course, such a calculation of the effective medium with subsequent Mie theory solution needs to be carried out for every wavelength.

The re-emission of photons by dust grains brings about one of the most important influences of dust clouds. A considerable fraction of the outwards directed local energy flow is redistributed into the opposite direction. The result is a heating of the atmospheric layers below, until the flux is once more conserved. The effect is denoted as backwarming.

4 Model Code

All calculations which have been done for this work were carried out with the general-purpose model atmosphere code PHOENIX (e.g., Hauschildt & Baron, 1999). It has been used for the simulation of a wide assortment of atmospheres, ranging from planetary atmospheres to supernova light curves. The current version also possesses a mode for time-dependent simulations. The code is 3D capable, with time-dependence pending the completion of integration with a hydrodynamical solver.

Atmospheric dust clouds have been introduced to the code by Allard et al. (2001). However, the resulting DUSTY and COND models proved to be far too simple to reproduce observations properly. Currently, the DRIFT code by Helling et al. (2008c) features the most sophisticated cloud model of the community. Dehn (2007) introduced it as module for PHOENIX for mutual benefit of both codes. Evaluation of these models and improvement of the combined convergence of both components was done by Witte (2008).

In the following sections, a brief overview of two codes is given. Subsequently, the code improvements since Witte (2008) and their impact are discussed.

4.1 The PHOENIX code

The current implementation of the dust model is designed for time-independent 1D atmospheres in LTE. Accordingly, PHOENIX is used in such a configuration. The resulting model atmospheres are an equilibrium solution between chemistry, thermodynamics and energy transport. A rough outline of the code structure is shown in Fig. 4.1.

Each calculation begins with the initialisation which involves reading of the fundamental atmosphere parameters and the exact model configuration. Required input data is either read directly or referenced for later use. Depending on whether the calculation is started from scratch or resumes a previous calculation, the initial atmosphere is either approximated by simple models or read directly.

The first computational step is the calculation of an equilibrium chemistry for a given temperature profile of the atmosphere accompanied by the concentration of the individual chemical elements (Sec. 2.4). As soon as this is complete, the altitude-dependent gas phase composition and the partial pressures are known. For this, the hydrostatic equilibrium and convection are calculated (Sec. 2.1). As the next step, the dust module is executed which returns the grain size distribution, the mean grain composition and the element abundances across the atmosphere. Because the solution of the EOS and the dust cloud bear the potential for a significant feedback on each other, a loop re-runs both modules.

With the chemistry completed, a logic module sorts out the appropriate atomic and molecular line opacities for the imminent radiative transfer calculation. In the LTE mode, occupa-

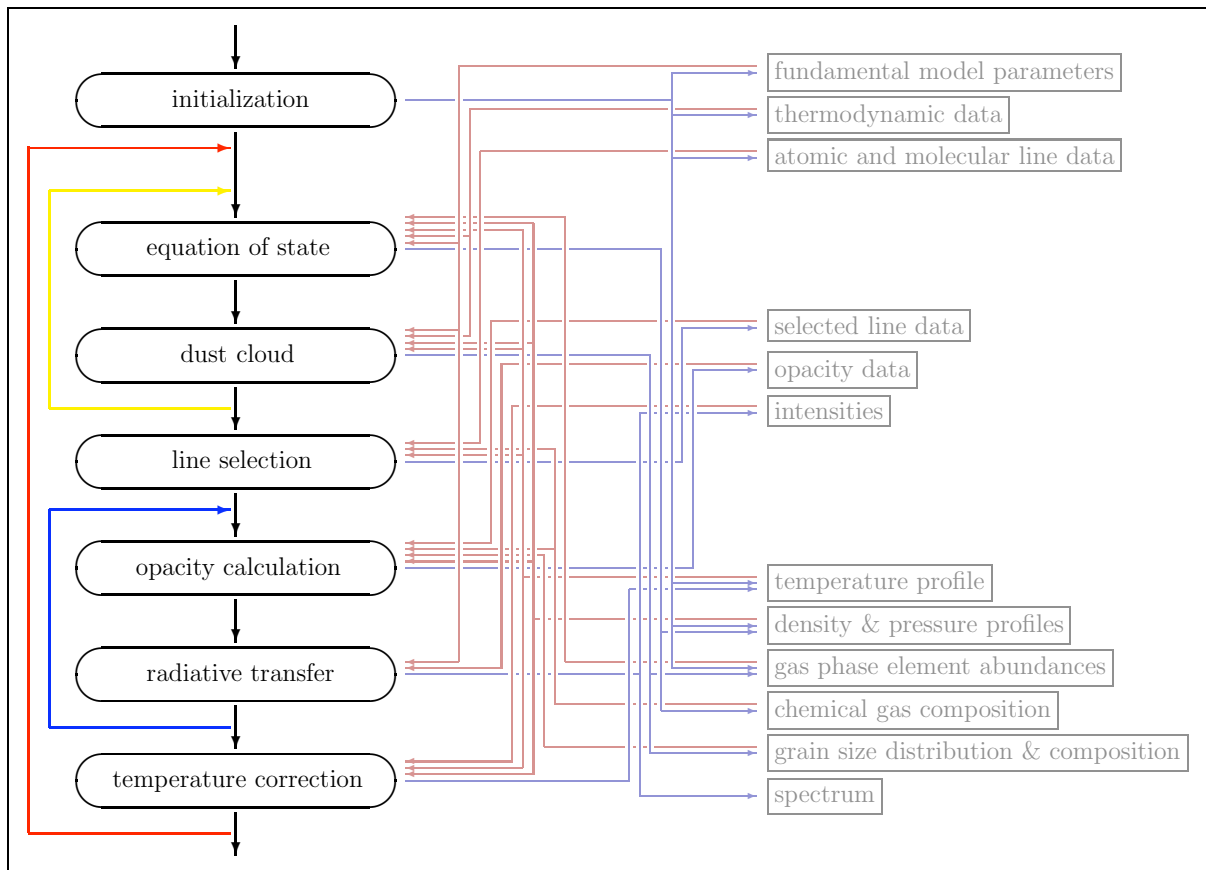


Figure 4.1: Flow chart for a typical 1D LTE PHOENIX run for brown dwarfs with dust treatment by the DRIFT module (*left*). The most important processed data elements are shown (*right*). The blue loop solves the radiative transfer equation for all considered wavelength bins. Highlighted in red, the main loop runs until a static solution is found (or a terminal condition is triggered). The yellow loop is responsible for calculation of an equilibrium between the equation of state and the dust cloud.

tion numbers do not rely on rate equations but are given by the Saha-Boltzmann distribution. Hence, it is possible to calculate all relevant opacities, including that of the dust cloud, before the actual solution of the radiative transfer equation. The radiative transfer itself is solved iteratively through operator splitting (Sec. 2.3). Opacity and radiation field are determined for all specified wavelength bins. In order to converge the model to a physical solution, all wavelength ranges have to be sampled.

As soon as the flux calculation is completed, deviation from radiative equilibrium is known. Consequently, the local gas temperatures have to be adjusted. The new temperatures of the non-convective atmospheric layers are determined by a modified Unsöld-Lucy method (Hauschildt et al., 2003).

Based on this new temperature, a new iteration is started, beginning with the EOS mod-

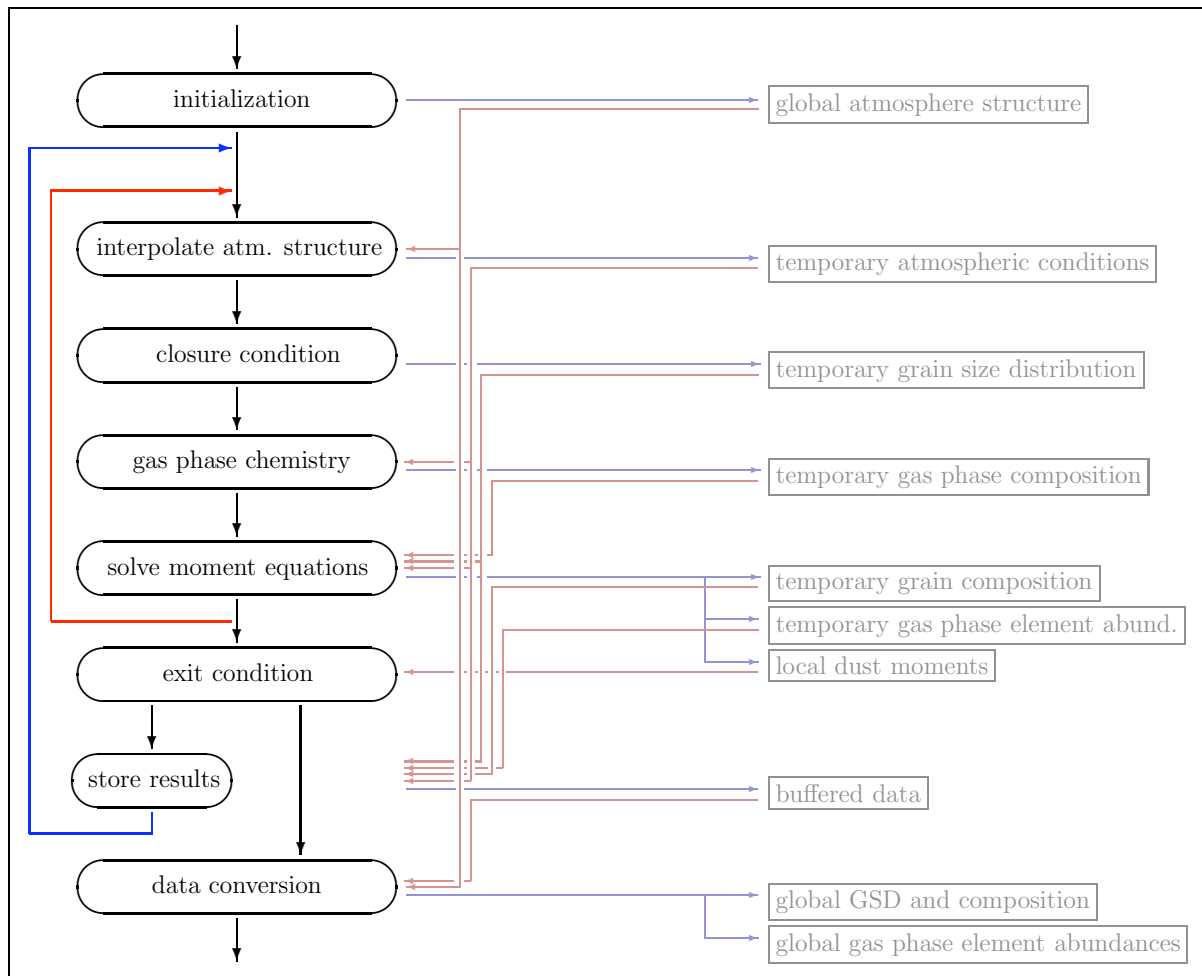


Figure 4.2: Flow chart for the DRIFT module (*left*) and the most important processed data elements (*right*). The loop highlighted in red corresponds to a Newton-Raphson iteration step while the blue loop is responsible for altitude steps.

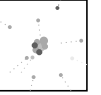
ule. The exit condition for this cycle is either the satisfyingly well determined radiative equilibrium solution for the given model parameters or a maximum number of iterations.

A more thorough description of the PHOENIX code is given by Hauschildt & Baron (2007).

4.2 The DRIFT code

The DRIFT code was originally designed as a standalone (Woitke & Helling, 2004). A rough flow chart is shown in Fig. 4.2. It relies on pre-calculated atmosphere models as input. The overshooting parameter, the mixing length and the convective velocities from the input are used to calculate the necessary mixing timescales. Thereafter, the actual cloud calculation can take place.

The algorithm starts in the upper atmosphere and assumes an initial set of dust moments



PHOENIX to DRIFT	DRIFT to PHOENIX
mixing length parameter l	grain size distribution $f(V, z)$
overshoot parameter β	average grain volume fractions $V_s(z)/V(z)$
gas temperature $T(z)$	depleted element abundances $\epsilon_e(z)$
gas pressure $p(z)$	
gas density $\rho(z)$	
mean molecular mass $\mu(z)$	
gravitational acceleration $g(z)$	
convective velocity $v_{\text{conv}}(z)$	
solar element abundances $\epsilon_{e,0}$	

Table 4.1: Table of the required exchange data between the two code components.

with zero values and undepleted element abundances. This assumption is not too far off, considering that the nucleation and growth processes are extremely ineffective at the low densities of the upper atmosphere.

In order to solve the system of dust moment and element conservation equations (Sec. 3.10), the atmospheric conditions such as temperature and pressure have to be interpolated for each given altitude, because the dust model is not designed to function for a preset layering of atmospheres but instead takes variable altitude steps according to the feasibility of determining a solution. Also, the closure condition has to be determined from the current set of dust moments (Sec. 3.10). Following the calculation of the chemical equilibrium for the gas phase from the current gas phase element abundances, the nucleation rate and the growth rate can be determined. Now that all prerequisites for the moment equations are known, the system of equations can be solved. The root of the system is determined through an adapted Newton-Raphson iteration, involving the closure condition, the gas chemistry and the moment equations.

After the physical solution is sufficiently well determined, a step to a lower altitude is taken. Assuming the altitude step is small, the final values of the dust moments and the gas phase element abundances from the previous altitude are appropriate initial values for the new altitude. This initial value problem is the reason why the dust code has not been parallelized.

If no solution is found for a given altitude, the last taken altitude step is undone and a smaller step is applied. For this reason, the number of atmosphere layers of the drift output is variable. The run of the code ends as soon as there is no dust left in the current layer, i.e., if there are negative dust moments.

4.3 Merging DRIFT with PHOENIX

With respect to memory requirements, the original dust code is very slim because the data is not stored in arrays to cover the altitude dimension but instead uses scalar variables. After the calculations for a given altitude are done, the variables are written into output files and consecutively overwritten for the next altitude.

For numerical stability, the dust module strictly requires input atmospheres that do not differ too strongly from the final atmospheres. In other words, too large differences between iterative steps will almost certainly cause an abort of the calculation. The reason for this is the strong sensitivity of the dust cloud to the gas temperature which itself is strongly affected by the dust opacity. For this reason, the temperature correction of PHOENIX is typically dampened strongly for atmospheres with dense dust clouds. The models typically have to be calculated in the restart mode with reasonably small steps of the model parameters. Further, this restart has raised the necessity of retaining the output file of the DRIFT module. It is required for the initialization of PHOENIX in order to keep variations of atmosphere properties between iterations at a minimum.

With this in mind, Dehn (2007) handled the data exchange between DRIFT and PHOENIX entirely through output files. The current version deviates in this respect. The data (see Tab. 4.1) is now passed directly. However, since the dust module output is still required for model restarts, the respective file is still written. All other output files are tagged optional.

For an optimal sampling of the atmosphere, the DRIFT-PHOENIX atmospheres are calculated for 256 layers. The dust module calculates the dust cloud for a previously undetermined number of atmosphere layers, which is typically around 500. This has to be converted to the PHOENIX layers. For the new direct data exchange, allocatable arrays are used to buffer the DRIFT output during the module run. Afterwards, the data is converted to the PHOENIX layers and the temporary memory is released.

With the revision of the data exchange, the dust opacity calculation has been redone as well. Originally a part of the data exchange routines, the dust opacity was calculated for 601 pre-selected wavelengths for each atmospheric layer. Later, in the opacity calculation module of PHOENIX, this would be interpolated to the actual wavelength grid. Such an approach bears two disadvantages. On one hand, the stored dust opacity data was permanently blocking memory. On the other hand, the pre-selected wavelength bins unnecessarily smoothed the dust opacity. In the current version, the dust opacity calculation is completely sourced out to the respective module of PHOENIX. The effective medium and Mie routines are now called once per wavelength bin, which allows a parallelized calculation. The direct calculation of the opacity for every wavelength increases the required computational effort, though not on a substantial level. The benefit is a potentially higher resolution of the dust opacity which is required for directly observable dust absorption features in the mid- and far-infrared. Unfortunately, such features have not been verified in the models yet, because the refractive index data at hand is not sufficiently well resolved.

4.4 Adaption of ACES

The new PHOENIX EOS module ACES (Barman, 2011), based on Smith & Missen (1982), was adapted for use with the DRIFT module. The altitude-dependent element abundances had to be passed instead of global element abundances. Unfortunately, the immense element depletion by dust formation often proved fatal for the chemical solver. Hence, the passed relative element abundances had to be limited to a minimum of 10^{-12} . Albeit unsatisfying, resulting deviations are unlikely to have a significant impact on model atmospheres or spectra

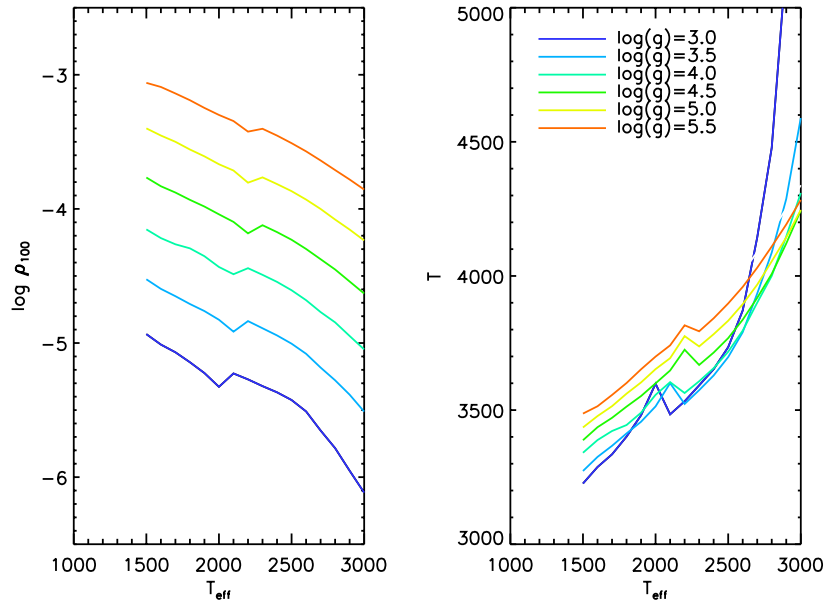
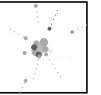


Figure 4.3: Boundary conditions (density and temperature at $\tau_{1.2\mu m} = 100$) for possible evolutionary calculations extracted from the model grid featuring the old EOS. There is a discontinuity 2100K that becomes more pronounced for lower gravity.

since the partial pressures and opacities of gas species involving such rare elements are negligibly small.

With the previous EOS, increasingly strong model oscillations occurred below $T_{\text{eff}}=2400\text{K}$. Below $T_{\text{eff}}=1500\text{K}$, models practically crashed immediately in the DRIFT routines due to exceedingly large variations of atmospheric properties. A large maximum in the oscillations was found around $T_{\text{eff}}=2100\text{K}$, caused by a discontinuity in the thermodynamic data sets. This discontinuity resulted in two distinct solution spaces that prohibited a use of earlier models for evolutionary calculations (Fig. 4.3). The symptom of this was the permanent oscillation between two solutions. Thanks to the new EOS, these problems are gone. Convergence of the model atmospheres has improved considerably (Fig. 4.5). The new boundary conditions for possible evolutionary calculations are continuous (Fig. 4.4).

The results of the convection calculation have changed slightly with the new EOS. The resulting convection zones end slightly deeper than before. As a result, the mixing efficiency by convective overshooting across the atmosphere has dropped, which has caused an inwards shift of the dust cloud (Fig. 4.6). Despite this, the average grain sizes and dust particle number densities are affected only weakly. The difference between spectra for old and new EOS models are nonetheless immense (Fig. 4.7).

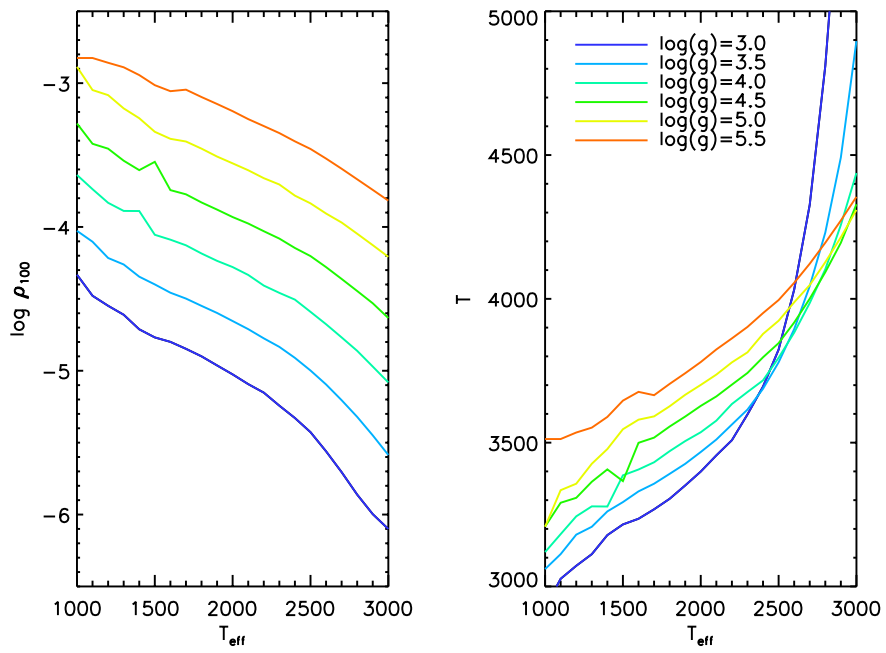


Figure 4.4: Same as Fig. 4.3 but for models based on the new EOS. In contrast to the curves for the old EOS models, the new model curves are continuous.

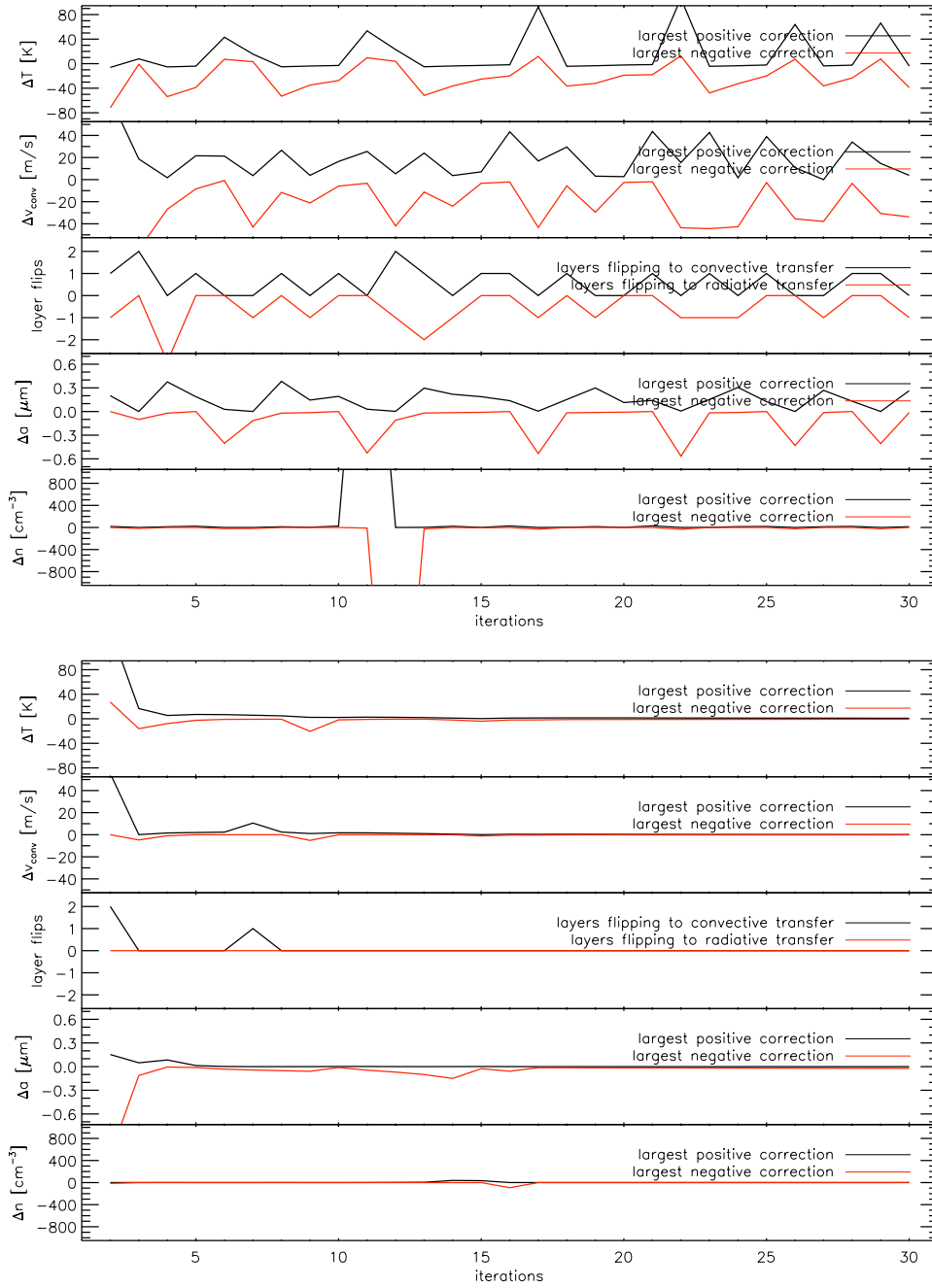


Figure 4.5: Comparison of model oscillations between old EOS (*upper panel*) and new EOS (*lower panel*). Both shown models correspond to $T_{\text{eff}}=2100\text{K}$, $\log(g)=5.0$ and $[M/H]=0$. From top to bottom, the five sub-panels denote the largest changes of the temperature ΔT and the convective velocity Δv_{conv} , the number of layers switching between radiative and convective energy transport and the largest changes of the mean grain size Δa and the dust particle number density Δn .

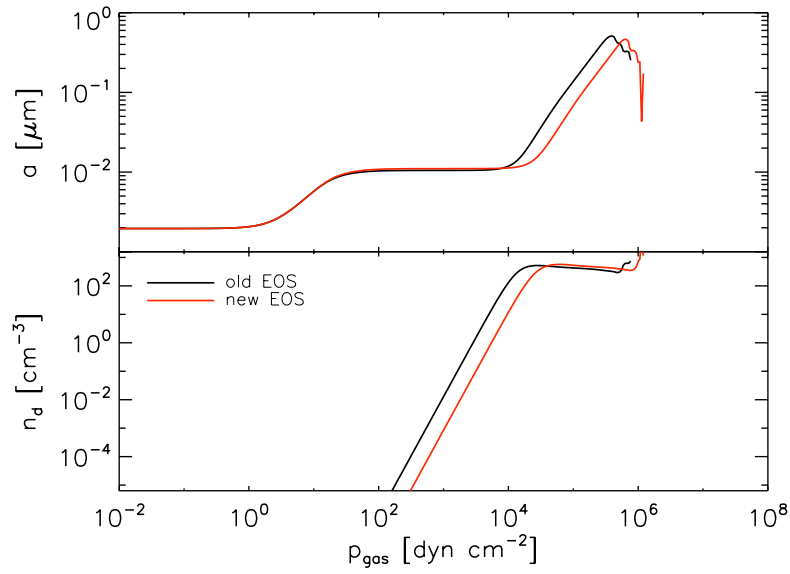


Figure 4.6: Influence of the PHOENIX EOS on the mean grain size and dust particle number density.

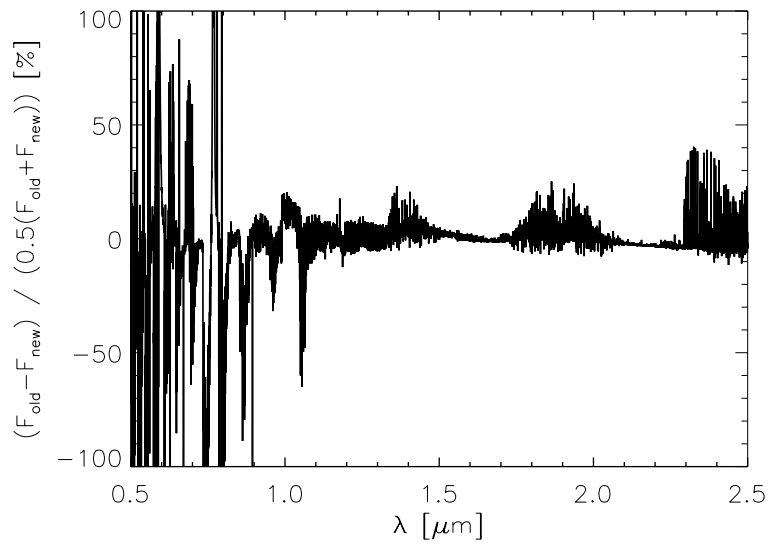


Figure 4.7: Normalised difference of the red optical and near-infrared spectra for the new and old PHOENIX EOS.



5 Results: The model atmospheres

This section deals with the analysis of the dust cloud structure, started by Witte (2008). As the destination of the cloud into five different regions, made in this previous work, applies to all but the most extreme cases in the stellar parameter space, it is employed here as well.

5.1 The gas phase

Before examining the cloud itself, it is worth to have a look at the gas of its environment. As mentioned above, the gas is strongly depleted by condensation (Fig. 5.1). As a rule of thumb, the more rare elements are typically stronger depleted in their relative numbers. As one of the most abundant elements, oxygen is affected the least even though its sheer number contributing to the forming solids is dominant (cf. Witte et al., 2009a, Tab. 1). Aside from the fact that it is comparably rare in the first place, titanium is much stronger depleted

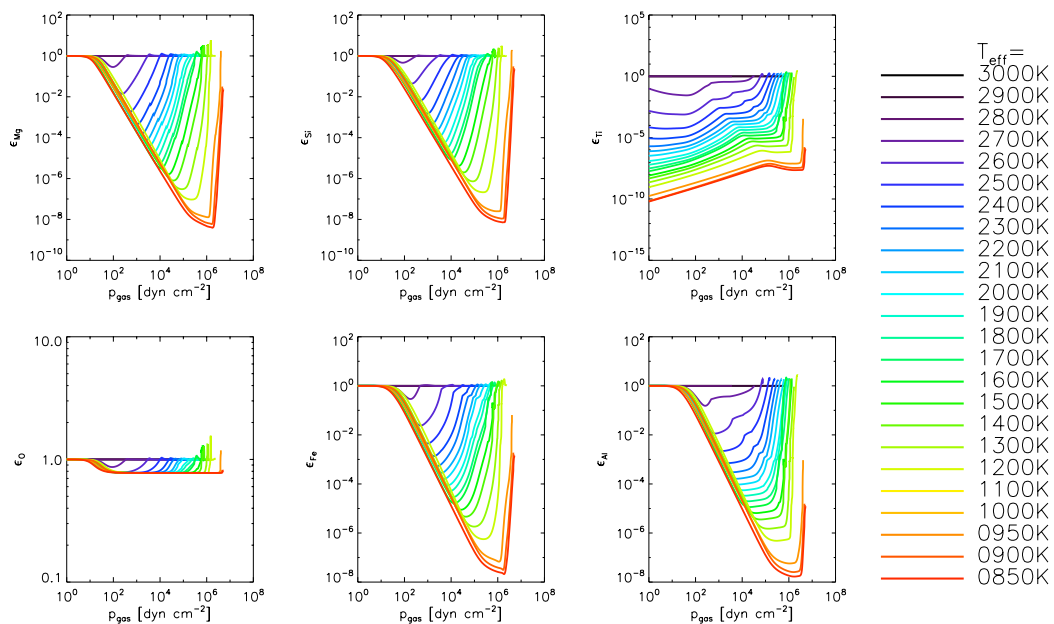


Figure 5.1: The gas phase element abundances are strongly altitude-dependent. The maximum gas phase depletion is typically found near the nucleation maximum. The panels show the element abundances normalised to a hypothetical undepleted and cloudless state of well-mixed atmospheres. (compare to Witte, 2008, Fig. 6.15).

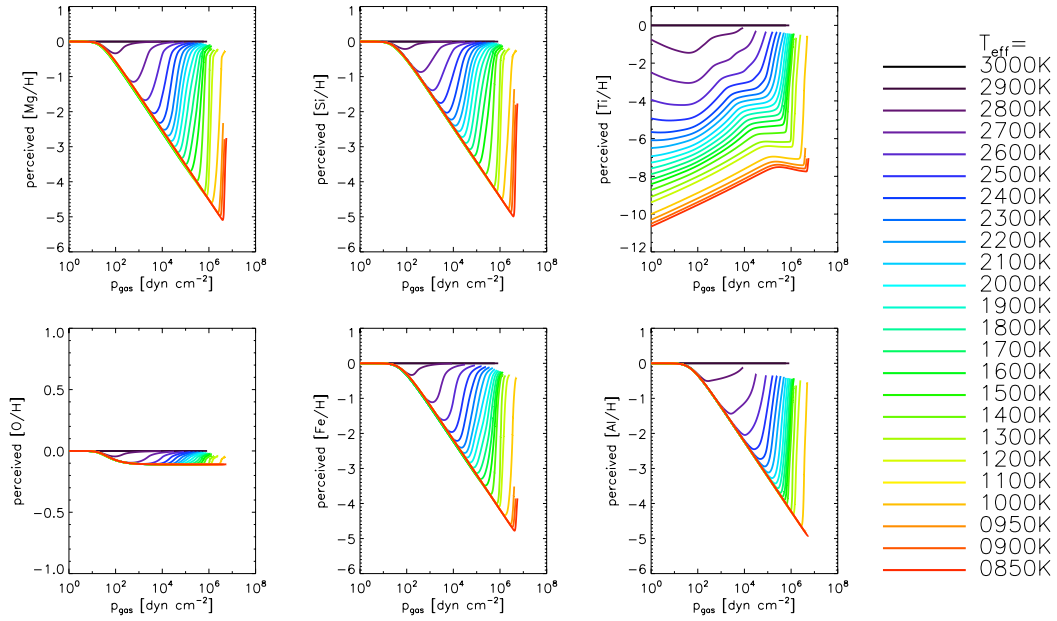


Figure 5.2: Depending on the wavelength, an observation will only penetrate the atmosphere to a certain depth. The diagrams show the perceivable metallicities above the indicated layer in terms of the gas pressure.

through the polymerisation of TiO_2 , i.e., *nucleation*. Most other solids, specifically all other ones considered in the current model, can not form efficiently through polymerisation of free gas molecules. Hence, the involved gas phase elements are comparably less depleted.

Above the evaporation region, the efficiency of nucleation and growth increases with atmospheric depth due to the rise of the gas density. Together, with the gas phase opacity, this effect determines the observable amount of elements within the atmosphere. Depending on the atmospheric depth to which one is able to look into the atmosphere at a given wavelength, the observed element abundances may vary widely over several orders of magnitude (Fig. 5.2). The deeper a view into the cloud, the lower is the perceived metallicity. Hence, the determination of stellar parameters from individual absorption lines can become ambiguous.

The variation of local element abundances feeds back on the individual gas species. Figure 5.1 depicts the most abundant gas species for three effective temperatures for a high and a low surface gravity, respectively. In the hottest models (3000K), there is no dust yet. Hence, the curves remain mostly flat and smooth. The second row panels correspond to early L type dwarfs, which already feature significant amounts of dust in their atmospheres. Therefore, considerable dips appear in the H_2O concentration while pure metals such as Fe, Mg and Si plus their hydrides and oxides vanish almost completely from the gas phase at the dense parts of the cloud. Around $T_{\text{eff}}=1000\text{K}$, metal hydroxides have replaced most of the hydrides which are prominent in atmospheres around the M-L-transition. Nevertheless, molecules involved in the dust formation are nearly absent from the gas phase over an even

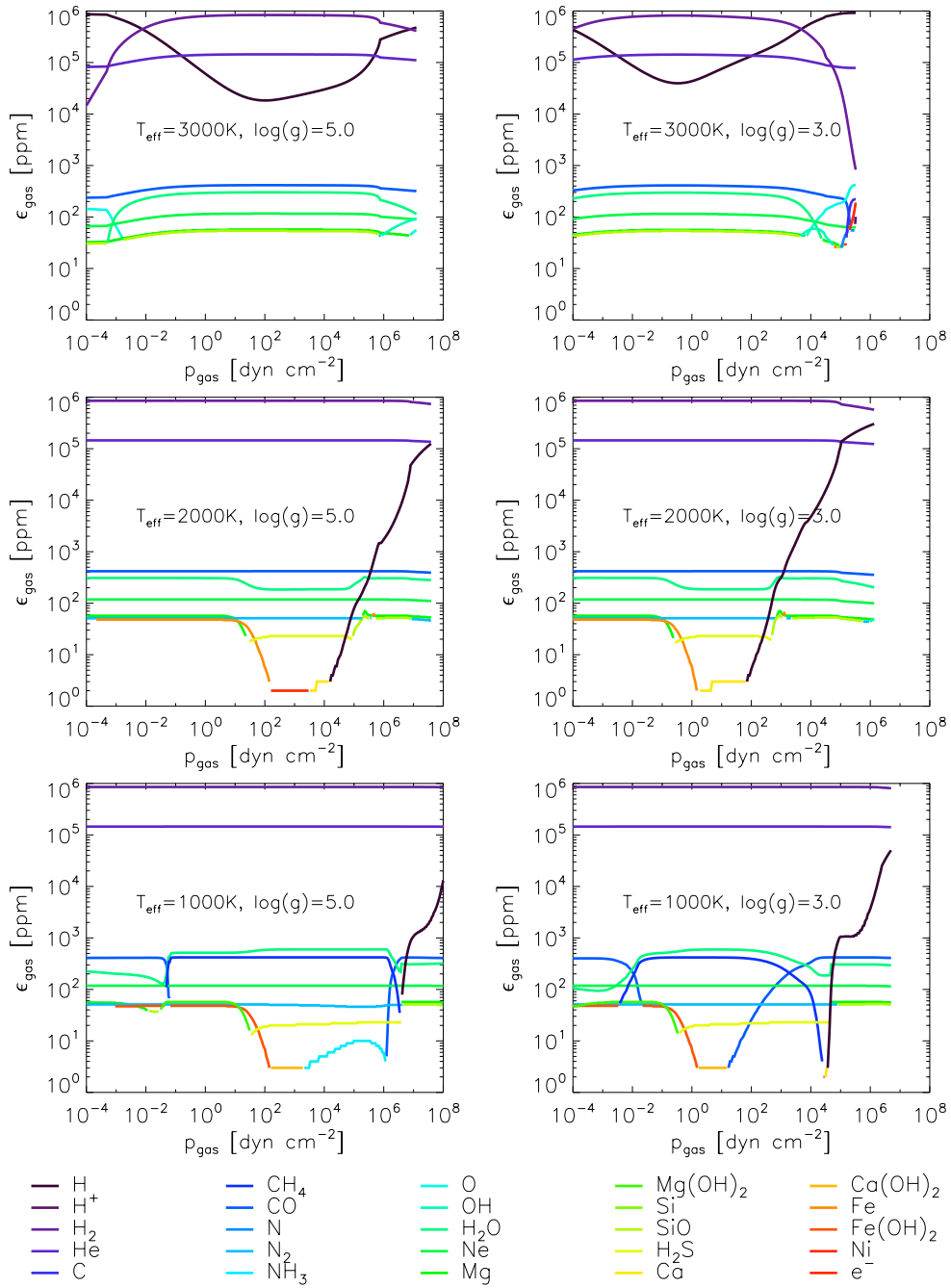


Figure 5.3: The most abundant gas species vary with the stellar parameters and are also sensitive to the dust cloud. Gas phase depletion by condensation can result in a considerable shift of the chemical equilibrium.

wider range of the atmosphere. Therefore, dust growth will proceed very slowly there.

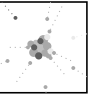
In addition, CO has dissociated throughout most of the atmosphere in favor of methane and water in the coolest featured models. This might open up entirely new reaction paths for the dust growth in even cooler atmospheres as methane represents the fundamental reactant for the formation of PAHs (polycyclic aromatic hydrocarbons) and condensation of other carbon compounds. Unfortunately, a carbon chemistry with respect to the solid phase is not considered in the current model.

At cooler model with clouds, Ca and $\text{Ca}(\text{OH})_2$ appear among the most common gas species. Neither is considered in the current dust formation of the model, hence, the element Ca is not depleted in the gas phase. In contrast, the newer standalone dust model version (Helling et al., 2008c) features $\text{CaTiO}_3[\text{s}]$ which relies on both Ca and $\text{Ca}(\text{OH})_2$ for growth. However, this growth is comparably weak and occurs only at the bottom of the cloud, where nucleation has ceased and the rare titanium is available for growth reactions. The overall abundance of Ca throughout the whole atmosphere seems to remain almost unaffected. From geology (e.g., Mueller & Saxena, 1977), it is known that the contribution of alkali and alkaline earth elements to the formation of igneous rock rises for decreasing condensation temperatures. While not forming from a magma but a gas, the dust grains in the atmospheres of interest will experience a similar diversification of their composition, nonetheless. Therefore, additional Ca-rich minerals as well as species containing other alkali/alkaline earth elements are likely required among the considered solid species of the dust model.

Another noteworthy aspect of the models is the enhanced concentration of H_2S in the cloud layers. In the current models, metal-sulfides contribute strongly to solid growth reactions. While the involved metals are integrated into the solid lattice, hydrogen sulfide is released to the gas phase. The strong metal depletion at the cloud inhibits the formation of new metal-sulfides, hence, hydrogen sulfide is accumulated in the gas phase at the cloud. A newer version of the stand-alone dust model (Helling et al., 2008c) features iron sulfide as solid species, which results in a depletion of the sulfur to some small degree in the upper cloud. However, iron is already heavily depleted through the formation of other solids. Hence, most of the sulfur is left in the atmosphere to form H_2S . At a first glimpse, the enriched H_2S might appear as a good indicator for the presence of dust in an atmosphere. Unfortunately, though, the enhancement has practically no relevance for the emerging spectrum. Only for considerably cooler models, wherein the silicate dust cloud has become optically thin, there might be a chance to observe the hydrogen sulfide directly.

Uncorrelated to the dust cloud, the high pressure environment of the coolest shown high gravity model begins to cause the formation of ammonia. Approaching temperatures of old Jovian planets, the ammonia and hydrogen sulfide become more and more important for the atmospheres because most other metals have rained out almost completely. At some point, both will start to form ices (e.g., Sromovsky & Fry, 2010), notably $\text{NH}_4\text{SH}[\text{s}]$, which are most prominently known for the colorful structures of Jupiter's atmosphere (Delitsky & Baines, 2007). Though the current models are still hundreds of Kelvins too hot to require the treatment of such clouds, they will be required eventually.

Comparisons with observations (Schmidt et al., 2008; Witte et al., 2011) suggest an over-estimated water opacity in the models. Figure 5.1 shows that the concentration of water



is only marginally affected by the presence of the dust cloud. Even though water is heavily involved in the model dust chemistry, its part is not as one-sided as for H_2S , which is solely a byproduct of growth reactions. Furthermore, oxygen is much more abundant than all other considered condensing elements. Therefore, the sheer number density of water molecules dominates over the number of dust growth reactants which ensures that only a small fraction of the water is involved in the dust formation.

With the possibility of over-abundant water in the model atmospheres from late M to late L spectral types, it is necessary to identify mechanisms that could be able to reduce the water concentration. Obviously, this can not be achieved through the gas phase chemistry alone, because the amount of water dominates over its potential reaction partners by several orders of magnitude. Non-equilibrium chemistry by mixing (e.g., Saumon et al., 2003) is also not able to have a considerable influence on the water because the atmospheric layers of interest are too cool to dissociate a perceivable fraction of the water. Another option is the condensation of water. However, the model atmospheres above approximately $T_{\text{eff}} = 700\text{K}$ do not feature temperature-pressure regions that could sustain even limited amounts of water ices (compare Fig. 5.4 and Dunaeva et al. (2010)). Likewise, the atmospheres of the current model grid are not dense and cool enough to sustain liquid water.

An intriguing option are porous, hygroscopic or charged dust grains. This way, the precipitating dust grain might carry away a significant fraction of the water to the bottom of the cloud. The easiest way to do so would be a transport of water molecules in voids in the grains. In a variation of this method, water molecules could slip directly into solids with large lattice parameters and, hence, might be carried along. A more intricate procedure to transport water with the dust grains is the formation of hydrates, i.e., direct integration of water molecules into a lattice structure with the actual salt/mineral. Furthermore, it might be possible that charged dust grains might attract nearby dipole molecules such as water and drag them along. Though, technically, most of these options represent no significant problem with respect to the implementation, the current lack of laboratory data forestalls anything but an arbitrary parametrisation.

As exemplified above, the observed model gas phase concentrations call for consideration of additional solids species. Unfortunately, the dust model is already strained to its limits, because each additional solid adds another moment equation, additional terms to the element conservation and possibly more conservation equations to the already stiff numerics. In the long run, it will be strictly necessary to relax the model numerics before it can be expanded. Even then, laboratory data is not available in many cases.

5.2 Atmospheric conditions

With the strong feedback between the dust cloud and its environment, it is useful to have a look at the atmospheric conditions around it.

The optical thickness of the dust cloud increases fast for decreasing effective temperatures. As a result, a growing backwarming feature establishes (Fig. 5.4). Witte (2008) discussed the immense bump in the temperature profiles in detail, that corresponds to a raise of the local gas temperatures by up to 1000K. The model grid presented by Witte et al. (2009a)

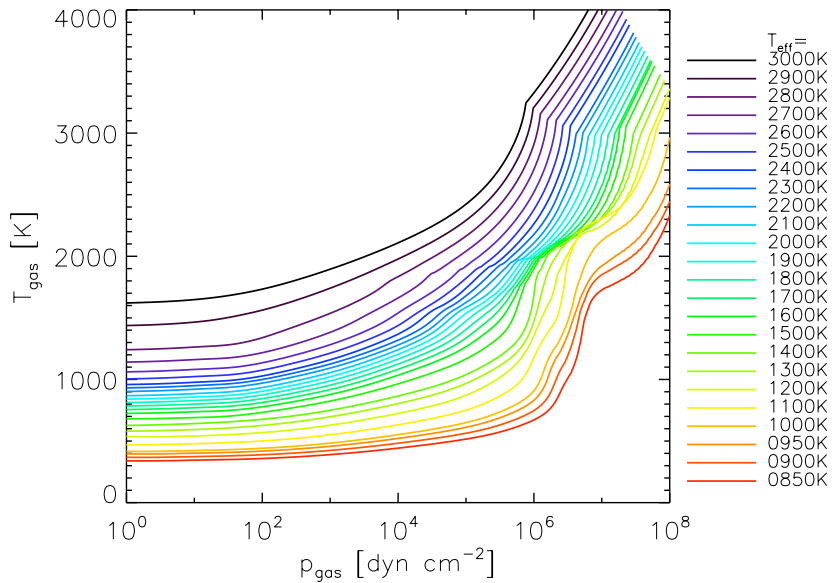


Figure 5.4: Temperature-pressure profiles of a model sequence for varied effective temperatures. The shown models feature $\log(g)=5.0$ and solar element abundances. (compare to Witte, 2008, Fig. 6.3)

ended at $T_{\text{eff}}=1500\text{K}$. These models suggested that this backwarming feature was not able to sink deeper into the atmosphere than to a pressure of 10^6dyn/cm^2 . Since the dust cloud sinks inwards for decreasing effective temperature, this implied a destruction of the cloud by its own backwarming at some point below $T_{\text{eff}}=1500\text{K}$. This was considered as a possible explanation for the sudden drop of dust opacity at the transition between L and T spectral types.

With the new EOS module, the temperature range of the new model could be expanded down to $T_{\text{eff}}=1000\text{K}$. As shown in Fig. 5.4, the backwarming feature is no longer stuck at a pressure of 10^6dyn/cm^2 for $T_{\text{eff}} \leq 1500\text{K}$. Against expectations, it begins to sink further inwards, again. Hence, the backwarming alone is not able to cause an abrupt loss of dust opacity as observations suggest.

The explanation for this change in behaviour of the backwarming bump is the descent of the convection zone edge for decreasing effective temperatures (Fig. 5.5), which is notably accelerated below $T_{\text{eff}}=1500\text{K}$. Simultaneously, the convective velocities drop rapidly. The withdrawal of the convection zone combined with lower velocities decreases the efficiency of the element replenishment across the upper atmosphere (e.g., Witte, 2008), which effectively shifts the dust cloud further inwards, as well. Therefore, the local dust opacity begins to drop at a given pressure region for decreasing effective temperatures. This is accompanied by a weaker local backwarming. However, as the gas density at the lower cloud layers has increased, the amount of dust within those layers is growing for decreasing effective temperatures. Therefore, the backwarming bump is shifted inwards for $T_{\text{eff}} \leq 1500\text{K}$.

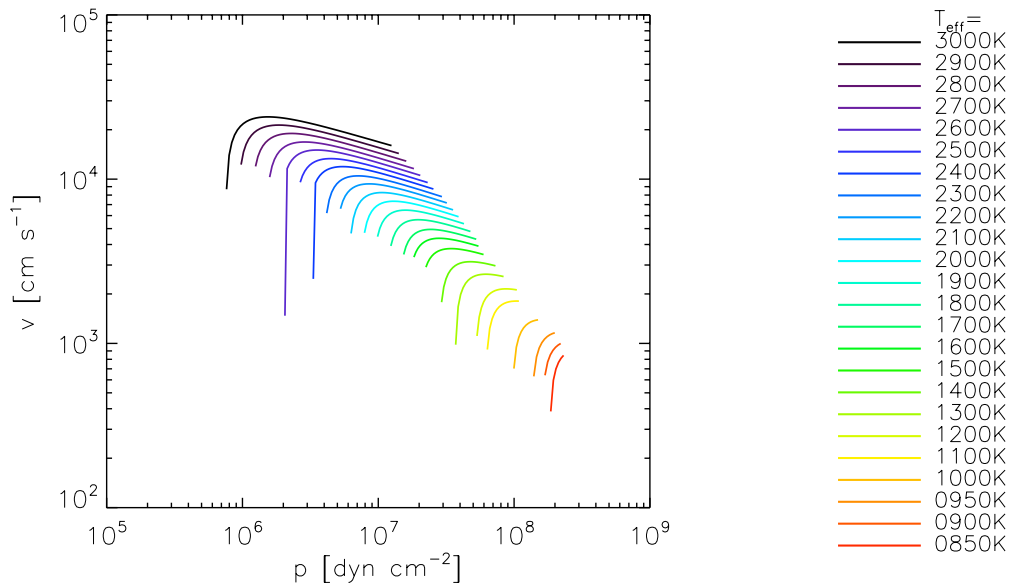
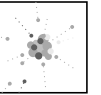


Figure 5.5: The convective velocity across the atmosphere, displayed on the pressure scale for an effective temperature model sequence for $\log(g)=5.0$ and $[M/H]=0.0$. (compare to Witte, 2008, Fig. 6.4)

Another interesting aspect of the backwarming feature is the associated gas temperature. For the hottest dust-bearing models it starts around 1800K and rises slowly to 2000K for $T_{\text{eff}}=1100\text{K}$. These temperatures agree with the critical temperature for the evaporation of Al_2O_3 and TiO_2 which dominate the respective layers of the cloud in these models. In models for lower effective temperatures, the gas temperature at the backwarming bump drops to about 1600K. In these models, the bottom of the cloud is no longer dominated by those high-temperature condensates but rather a mixture of silicates and iron. Their critical temperatures are notably lower. Hence, the atmosphere is not heated as much before the dust grains have evaporated. For this reason, the composition of dust grains at the bottom of the dust cloud is imprinted into the temperature profile of the atmosphere.

5.3 Revisiting the cloud structure

With respect to the grain size distribution, there are five distinct zones within the clouds (Fig. 5.6), which are defined according to characteristic changes in the altitude-behaviour of the mean grain size (Witte, 2008). The cloud regions alternate between zones of flat mean grain sizes and zones of strong growth/evaporation of the mean grain size, beginning with the flat seed-dominated haze on top. This structure of the model clouds determines the dust opacity and is vital for our understanding of the physics of dust-bearing atmospheres. Each kink in the grain size and dust particle number density denotes a change of balance between the various effects on the dust.

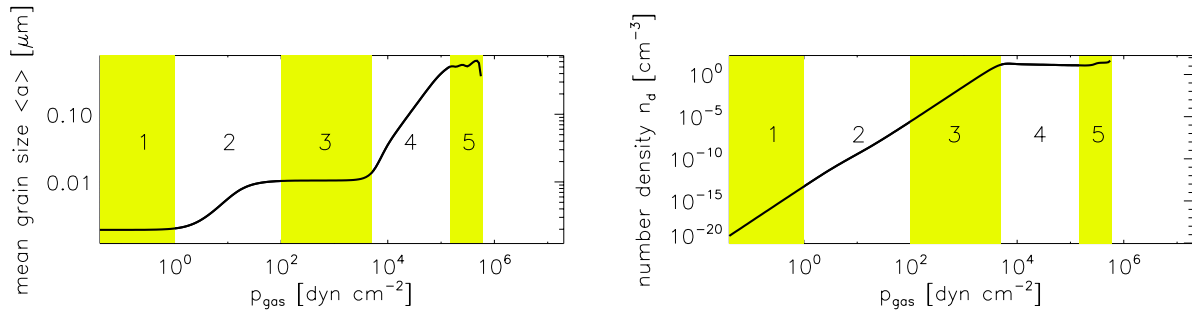


Figure 5.6: From top to bottom of the cloud there are five distinct regions: 1. seed-dominated, 2. first growth, 3. drift-dominated, 4. second growth, 5. evaporation. (Shown on an example model for $T_{\text{eff}} = 2000\text{K}$, $\log(g) = 5.0$, $[M/H] = 0.0$.) This plot is excerpted from Witte (2008)

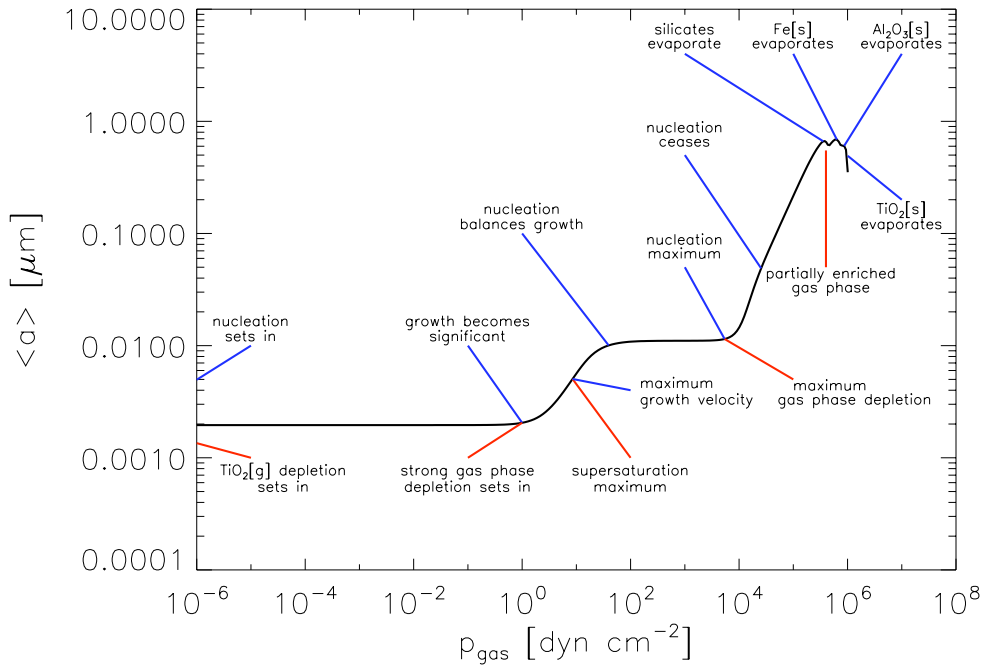
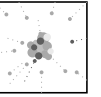


Figure 5.7: The mean grain size $\langle a \rangle$ is very sensitive to a number of effect. All significant balance shifts between the various influences on the dust particles are embossed in the mean grain size over the altitude.

At this point, the discussion of the cloud structure characteristics by Witte (2008) is briefly summarized, which is necessary for following sections:

In the uppermost region, nucleation, i.e., polymerisation of gas molecules, dominates the



cloud. These forming seeds, which in case of the DRIFT model consist of $\text{TiO}_2[\text{s}]$, fall inwards at a significant fraction of the speed of sound, due to their high density compared to the environment. The increasing gas density for shrinking altitude results in growing friction. At some point, the collision rates between gas and dust grains become large enough to permit growing numbers of surface reactions. The formation of various solids on top of the TiO_2 seeds increases the size of the grains considerably and results in a strong depletion of the gas phase. At the same altitudes, the rate of newly forming seeds rises exponentially. Over the following atmospheric layers, the increasing number of particles, consuming elements from the gas phase, begin to reduce the collision rate with condensible gas molecules. The slower descent, caused by the rising density, magnifies this effect. The growth of the mean grain size ends. However, this does not mean that growth is irrelevant in the atmosphere below, but rather that the increasing size of the larger particles is compensated by the size of newly forming grains. This balance between growth and nucleation lasts through the deeper atmospheric layers until the efficiency of the nucleation process drops, which occurs on a very short pressure interval. No longer kept in check, the mean grain size increases immensely with depth, which in turn ends the decrease of the grain fall velocity, which remains more or less constant for an average grain over the deeper cloud layers. At about the height of the nucleation maximum, the maximum gas phase depletion is reached as well. Likewise, the local backwarming can already exceed several hundred Kelvins. The subsequent fast growth of the dust grains by roughly two orders of magnitude results in an even faster rise of the local temperatures with the gas pressure. The solid silicates are the first to react to this. Over a short pressure interval, all their chemical reaction paths begin to favor dissociation. The silicate evaporation can cause a drop of the mean grain size, resulting in a perceptible local maximum. However, the extremely fast growth of $\text{Fe}[\text{s}]$ and $\text{Al}_2\text{O}_3[\text{s}]$ may already dominate the overall growth process and cover such a peak in the grain size. With growing importance of the iron volume fraction, the grain opacity rises strongly for the optical and near-infrared. Hence, over a short distance, the environment of the falling grains will heat extremely fast, causing a quick evaporation of solid iron, slightly deeper in the atmosphere followed by Aluminium-Oxide and Titanium-Dioxide. Each with its own possible maximum perceivable in the mean grain size. Following the evaporation of the last species, the cloud ends. Regardless, the atmosphere beneath is considerably hotter than it would have been without dust. In some cases up to twice as hot. Inside the evaporation regions of individual solids, the abundances of constituent elements may be enhanced, compared to a dust-free atmosphere.

5.4 The cloud in general

5.4.1 The cloud structure as function of the stellar parameters

The model cloud region boundaries on the pressure scale as functions of the effective temperature and surface gravity are shown in Fig. 5.8.

Irrespective of the surface gravity, clouds begin to form below $T_{\text{eff}}=2900\text{K}$ for solar el-

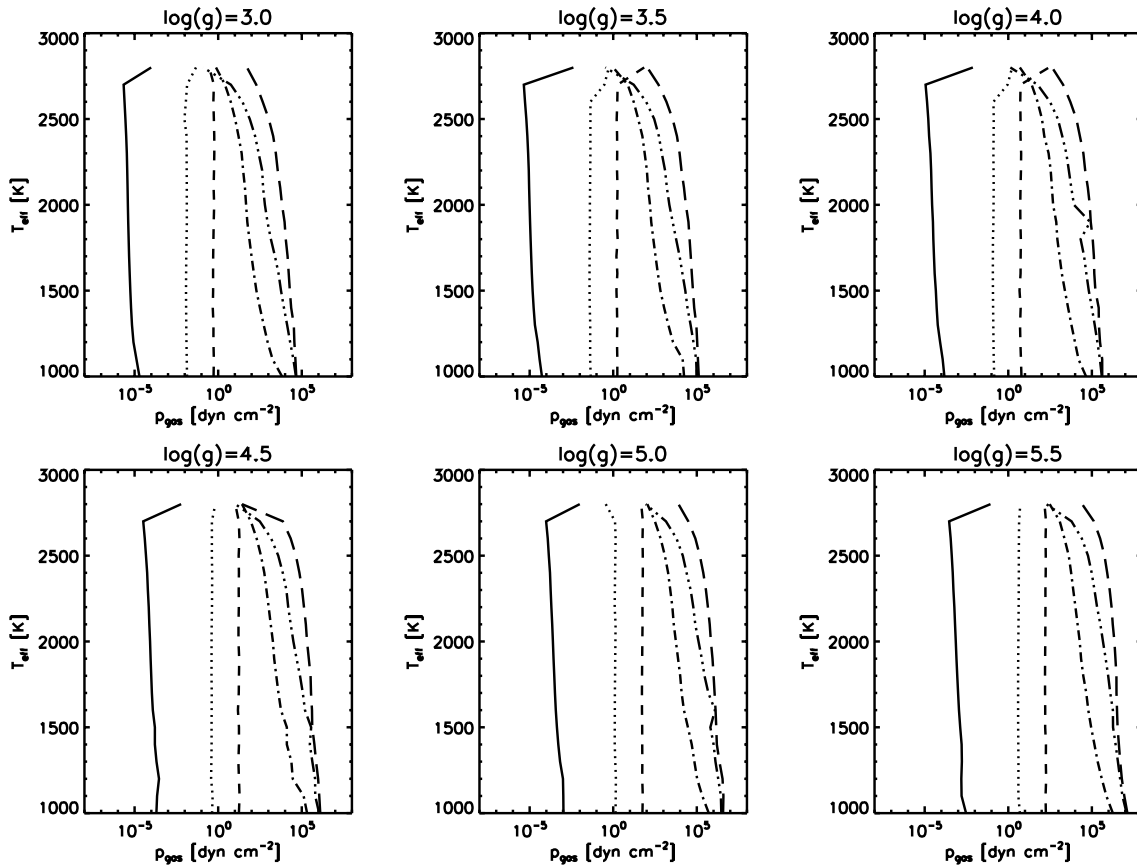


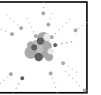
Figure 5.8: The five cloud regions react to the stellar parameters. The curves correspond to the outer cloud boundary (—), onset of the first significant growth (\cdots), end of the first growth region (— —), onset of second growth region (- · -), end of second growth region (- · · ·) and inner cloud boundary (—).

element abundances¹. Initially, the model clouds span only across confined regions of the atmospheres but over a small range of effective temperature expand to some eight to ten orders of magnitude on the pressure scale. Below $T_{\text{eff}}=2500\text{K}$ the cloud extension remains more or less constant on the pressure scale.

The growing gas density accompanying a rise in the surface gravity increases the gas pressure at the dust cloud. Otherwise, the surface gravity has no noteworthy influence on the extension of the individual cloud regions with respect to the pressure scale.

The outer cloud boundary is the point for which the first dust particles are present in the atmosphere. In the models, this is typically the point where the calculation is started. Only for $T_{\text{eff}}=2800\text{K}$ models, this boundary agrees with the altitude of the onset of nucleation. For lower effective temperatures, the actual onset of nucleation is shifted to much lower pressures

¹Unless noted otherwise, the term element abundance is used for the global average value of an objects and not the altitude-dependent abundance.



very fast and lies well beyond the outer cloud boundary of the model clouds. The reason for this is the strongly growing region of supersaturated gas for decreasing gas temperatures. Errors by disregarding the outer atmosphere dust seeds are negligible, though, considering the tiny gas density beyond the indicated limit.

At the highest altitudes, the dust seeds do not grow significantly. Only further inwards, where the supersaturation of the gas is at its maximum, a first growth region is situated. Interestingly, the upper and lower boundary of this region are hardly affected by the effective temperature. Only for the hottest dust-bearing models, these limits are shifted notably towards the supersaturation rate maximum. The reason for this is the weak square root dependence of the dust-gas collision rate (Eq. 3.5) on the gas temperature combined with the dependence on the exponential increase of the gas density with atmospheric depth. Because the gas density is almost independent of the effective temperature of the given models, both boundaries remain nearly fixed to unique pressure values. In contrast, the surface gravity affects the gas densities directly and, hence, causes shifts of the first growth region of the dust cloud. A change of $\log(g)$ results in a linear shift on the logarithmic pressure scale.

The region below this first growth zone is characterised by a constant mean grain size. It ends as soon as the efficiency of the nucleation process begins to drop. Its lower boundary is shifted by the surface gravity in the same fashion as its upper boundary. Thus, the extension of this region on the pressure scale is not affected by the surface gravity. In contrast, a decrease of the effective temperature is responsible for an increase of the supersaturation rates which enables nucleation to last into lower layers of the atmosphere. For the hottest dust-bearing models, this region is non-existent while it grows to span over four orders of magnitude of the gas pressure at about $T_{\text{eff}}=1000\text{K}$. Though unspectacular with respect to the grain size, it is this region that determines the amount of dust within the atmosphere because its strong variation of extension. Its lower boundary holds control over the number of particles that are formed. A higher gas pressure, i.e., a higher gas density, at the lower boundary brings about a higher number of particles.

The second to last cloud region is responsible for most of the grain growth. As no additional particles can be formed, all material in the gas contributes to the growth, only. Again, the surface gravity has only a weak impact on the extension of this zone except for shifting it to a different pressure. For effective temperatures below 2500K , this second growth region spans over an almost constant range of one and a half orders of magnitude with respect to the pressure. The achieved maximum mean grain sizes do not vary strongly over the stellar parameter space.

In the lowest parts of the cloud, the individual chemical growth reactions begin to switch from growth to evaporation. This means, only here, a noticeable diversification of the grain composition with the stellar parameters is able to take place. As a result of the still weak gas temperature gradient of the atmosphere, the evaporation zone stretches over more than two order of magnitude in pressure for the hottest dust-bearing models. The backwarming effect caused by the dust cloud grows for cooling atmospheres and creates a steep gradient at the bottom of the dust cloud. Thus, the evaporation zone shrinks fast with decreasing effective temperature.

In summary, the upper dust cloud structure on the pressure scale is mostly unaffected by the effective temperature while the lower cloud structure varies. The surface gravity is

mostly responsible for shifting the cloud through the atmosphere, or more precisely on the pressure scale, but the cloud structure remains mostly unharmed by this.

5.4.2 Geometrical extension of the cloud

The previous section referred to the cloud extension with respect to the pressure. However, more intuitive and also more significant with respect to the absolute amount of dust within the atmosphere is the geometrical thickness. A brief discussion of this, based on the previous model generation, was given by Helling et al. (2011). The geometrical extension of the dust cloud is shown in Fig. 5.9. In stark contrast to the cloud extension on the logarithmic pressure scale, the geometrical cloud extension depends strongly on the surface gravity. For low surface gravities, the typical cloud thickness exceeds the thousand kilometer mark. In more compact high gravity atmospheres, the clouds shrink to few kilometers of vertical expansion. A closer look on Fig. 5.9 reveals that the geometrical thickness of the cloud is largest for approximately $T_{\text{eff}}=2000\text{K}$. The reason for this is a selfregulation of the cloud, created by

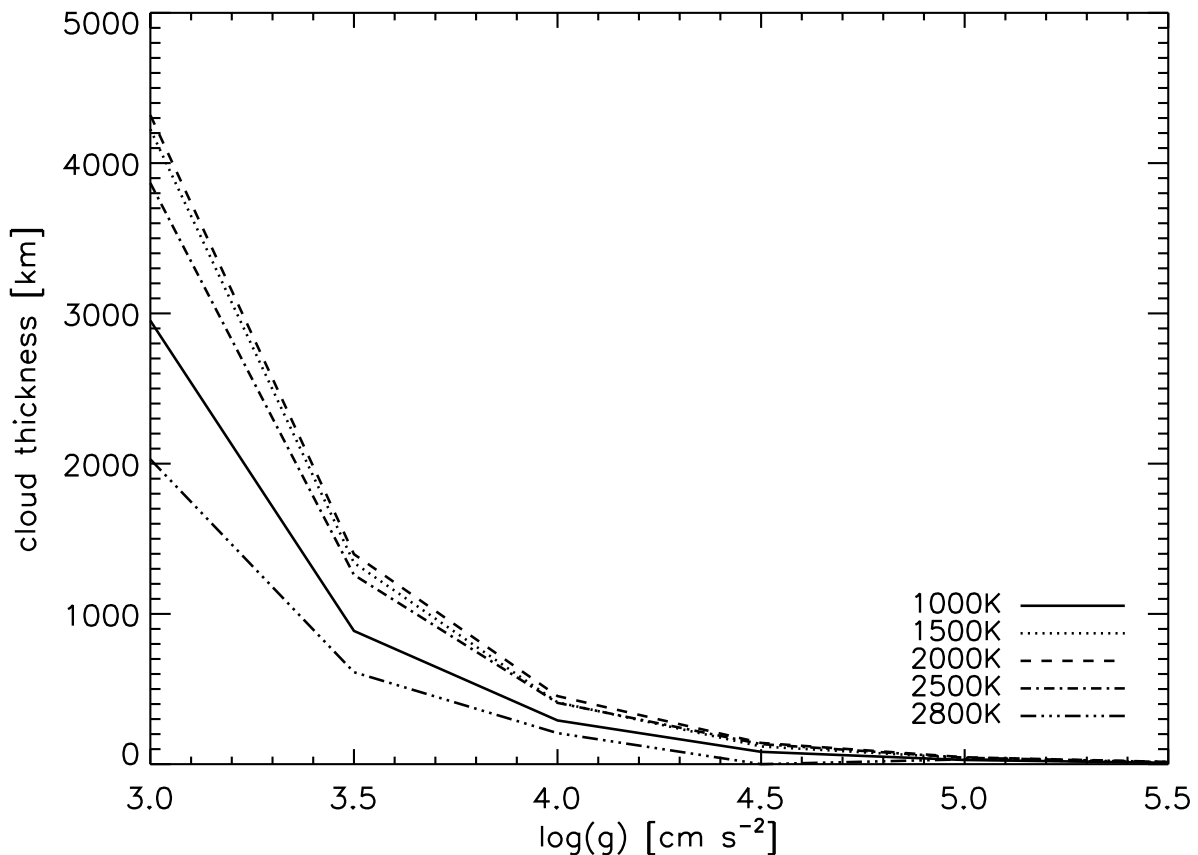
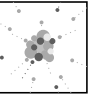


Figure 5.9: The geometrical thickness of the dust cloud varies strongly with surface gravity of the model. Compared to that, the effective temperature has only a small influence.



the its own backwarming: Above $T_{\text{eff}}=2000\text{K}$, the growing zone of supersaturated gas with decreasing effective temperatures results in the fast expansion of the cloud. This significantly increases the dust opacity. Around $T_{\text{eff}}=2000\text{K}$, this increasing opacity has reached a critical point and literally melts away the lower parts of the cloud. Nonetheless, the opacity of the remaining cloud rises with decreasing effective temperature. Thus, a growing fraction of the cloud is lost to backwarming. The backwarming forestalls the otherwise unchecked growth of the supersaturation zone into more dense layers of the atmosphere.

Atmospheres at clouds of up to several thousand kilometers thickness bear one potential problem. With an approximate object radius of 100000km , the cloud covers a significant fraction of the outer shell of the object. Hence, the plane-parallel geometry of the dust model starts to be no longer appropriate. This affects the gravitational settling term of the current dust model. The result of a spherical geometry would be a higher inflow rate from above. In other words, the dust particle number density would grow faster for decreasing altitude. The condensible gas species would have to be distributed over a larger number of dust grains with an overall reduction of the mean grain size. A larger number of particles increases the opacity, which would sustain a stronger backwarming. Thus, the bottom of the cloud would be pushed upwards.

5.4.3 Life cycle of a dust grain

The velocity of a dust grain due to gravitational settling (Eq. 3.16) is a function of the grain size its density/composition and the properties of its environment. Therefore, it is not surprising that typical grains require different amounts of time to cross the individual regions of the dust cloud. Furthermore, the lifetime of dust grains can be separated into different periods they spend in these regions. These timescales are shown in Fig. 5.10 for grains that start their descent at the uppermost considered cloud layer. The surface gravity affects these timescales in two ways. On one hand, the fall velocity is proportional to the gravitational acceleration. On the other hand, a higher gravity makes the cloud geometrically thinner (Sec. 5.4.2). Between $\log(g)=3.0$ and 5.0 the timescales differ by an almost constant factor of roughly 300. For instance, for a $\log(g)$ of 5.0 , typical grains take roundabout 10 seconds to cross the uppermost cloud layers, before the first significant growth takes place. For a low gravity ($\log(g)=3.0$), this takes almost a full hour.

With decreasing altitude, the density of the environment grows exponentially. At the same time, the mean grain size rises only in two distinct regions of the cloud. Thus, the grain size is unable to compensate for the gas density with respect to the gravitational settling. Because the descent is slowed down considerably, more time is spent at consecutive cloud regions.

As shown in Sec. 5.4.1, the position and extension of the first growth region of the cloud is only weakly influenced by the effective temperature. Therefore, also the time required to fall through the first growth region is rather weakly affected by the effective temperature. In contrast, the zone between the two growth regions of the mean particle size is becoming broader for a decreasing effective temperature. This broadening extends into atmospheric layers of considerably higher densities. For this reason, the dust particles take considerably more time to pass this region for low effective temperatures. For $\log(g)=5.0$, the time spent

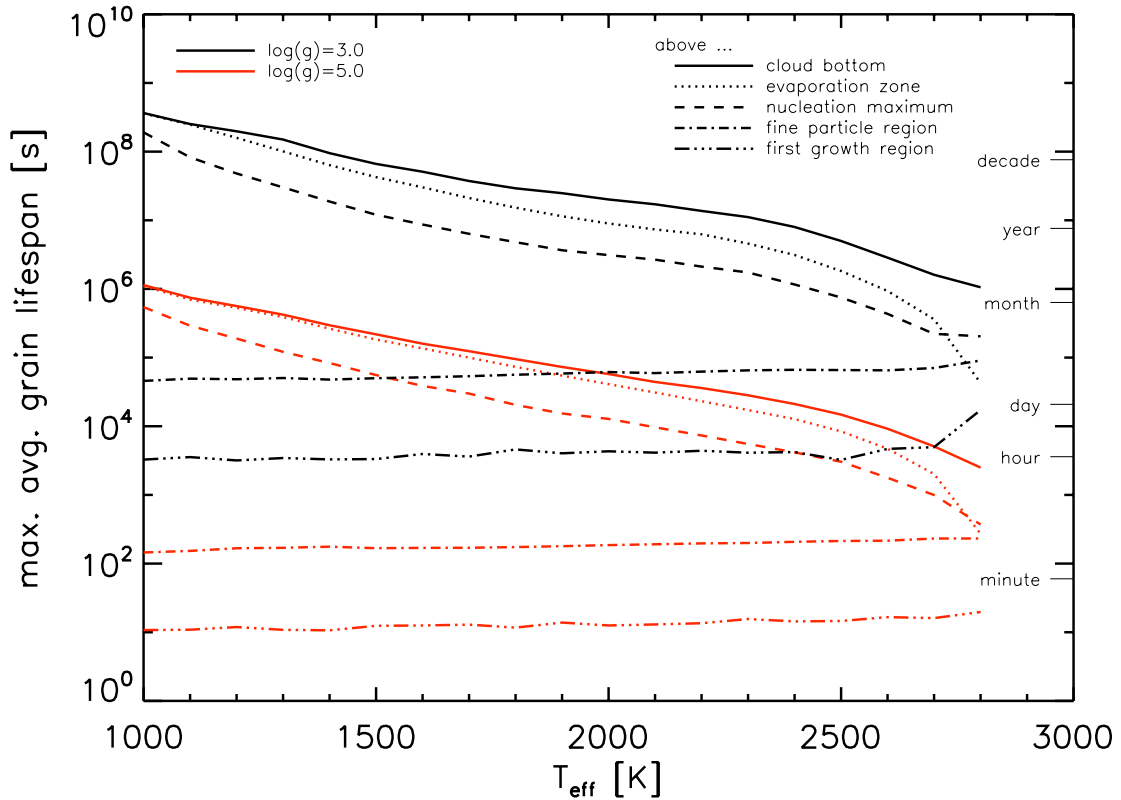


Figure 5.10: A grain of average size requires a certain amount of time to descent a specific distance. The curves show the required time to reach critical points of the dust cloud, for typical grains that begin their fall at the highest cloud layer.

at this region is roughly 20 minutes near the edge of dust formation ($T_{\text{eff}} \approx 2800\text{K}$) and rises by 3 orders of magnitude to about a month for the coolest considered atmospheres. Again, the timescales increase by a constant two and a half magnitudes for $\log(g)=3.0$.

In the hottest dust-bearing model atmospheres, the evaporation of the silicates starts before the formation of new particles has ceased. This represents an overlap of the otherwise well-separated cloud layers. It is well discernible in the descent time-scales (Fig. 5.10), because the upper evaporation zone edge, identified with the silicate evaporation, is reached much earlier than the maximum of the nucleation.

All parts of the cloud considered, the life of an average dust grain lasts between an hour for the hottest, high gravity model atmospheres with dust clouds and half a century for coolest considered low gravity atmospheres. Therefore, it is one of the critical factors that determine the number of dust particles within an atmosphere. Compared to typical mixing timescales due to convective overshooting, the amount of time that typical particles take to pass the cloud from top to bottom are negligible. In contrast to that, turnover timescales by convective motion are considerably shorter than the lifetime of typical grains (compare

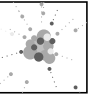


Fig. 5.5). Hence, should convection become the most efficient way of transporting energy at some part of the dust cloud, the resulting high velocities will likely tear the cloud apart in short order.

5.4.4 Amount of dust

In order to study all the mechanisms affecting atmospheric dust clouds, it is necessary to have a tool for quantitative comparisons between different stellar parameters. Dehn (2007) suggested the column density of the dust particle number. This represents a good measure in the upper parts of the clouds, because the number density is the determining quantity with respect to the dust opacity while the mean size and composition of dust particles are effectively independent from the stellar parameters, there. Unfortunately, the mean grain size as well as the mean grain composition are affected by the stellar parameters in the lower parts of the cloud. Hence, the column density of dust particles alone is not able to provide a conclusive summary of all dust cloud quantities.

Preparation: The optical depth with respect to the dust is defined as $\tau_{\text{dust}} = \int_0^{\infty} \chi_{\text{dust}}(z) dz$. Based on Eq. 3.41 it can be rewritten as:

$$\tau_{\text{dust}} = \sqrt[3]{36\pi} \int_0^{\infty} \int_0^{\infty} (Q_{\text{abs}}(V, \vec{b}_s) + Q_{\text{sca}}(V, \vec{b}_s)) f(V, \vec{b}_s, z) V^{2/3} dV dz \quad (5.1)$$

The absorption and scattering efficiencies of a specific kind of dust grains is invariant to the altitude. Hence, neglecting the altitude-dependence of the average dust grain composition, both values can be pulled out of the altitude integral. Likewise, it is useful to assume a negligible influence of the grain size on both efficiency values, which yields:

$$\tau_{\text{dust}} = \sqrt[3]{36\pi} (Q_{\text{abs}} + Q_{\text{sca}}) \int_0^{\infty} \rho L_2(z) dz \quad (5.2)$$

In other words, the altitude-integrated dust moment of second order, or more precisely, the sum of the cross-sections of all grains in a line of sight, is proportional to the dust opacity. From the perspective of the radiation field, it bears much more significance than the mere column density of dust grains.

At this point, the reliability of the approximation $\tau_{\text{dust}} \sim \int_0^{\infty} \rho L_2 dz$ necessitates verification. Figure 5.11 demonstrates the extinction efficiency (absorption + scattering) of a representative example of grain composition. This efficiency is evidently a function of the wavelength. More important for the approximation, however, is the efficiency gradient as a function of the grain size. The most significant feature of the silicate-dominated grains of the figure is the sharp edge in the far infrared. Comparable ridges can form for significantly different grain compositions. For smaller grains, such edges result in a snowballing rise of dQ/dV . For those grains, the approximation is technically violated. However, unless the

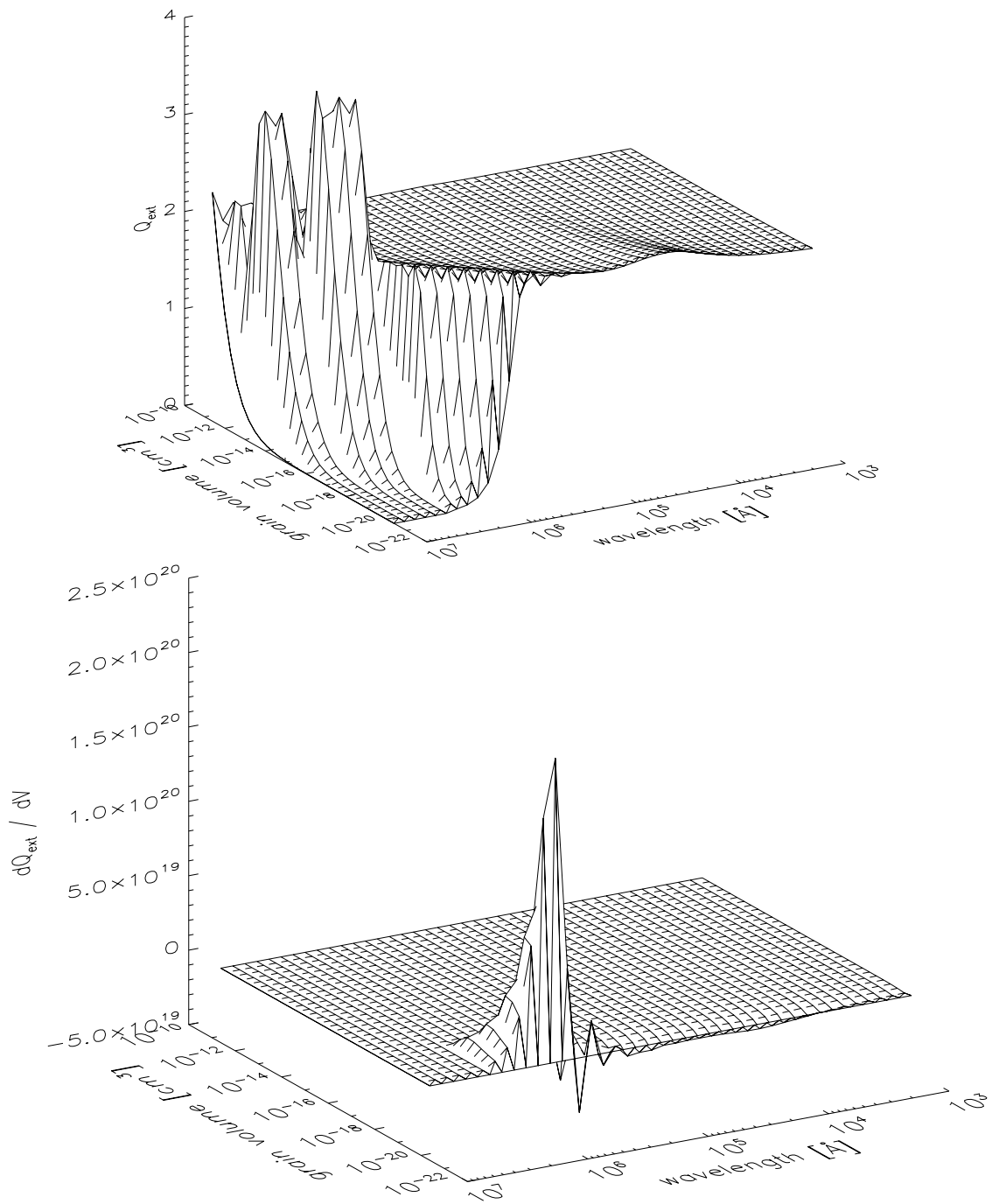
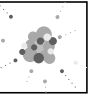


Figure 5.11: Extinction efficiency of a single dust grain of a typical composition (a conglomerate of silicates with admixed iron) from the middle of the dust cloud versus the grain volume and the wavelength. The lower panel represents the volume gradient of this efficiency.



grain size distribution is dominated by such tiny particles, the violation is not as significant as it appears on the first look. The extremely small cross-section of these particles compensates most of arising errors. For shorter wavelengths and the given grain composition the extinction coefficient becomes all but independent from the grain size. Though a different composition of the dust can add additional wavelength ranges that strain the validity of Eq. 5.2, errors typically remain connected to the smallest particles. Therefore, as long as the mean grain size is large enough, $\tau_{\text{dust}} \sim \int_0^\infty \rho L_2 dz$ is a viable approximation for all wavelengths. While the mean grain composition does vary only weakly with the stellar parameters, it allows to assess the changes of influence of the dust cloud layers on the radiation field with these parameters.

In a similar fashion, the altitude-integrated third order dust moment is qualified to describe the actual amount of material in the solid phase. Together with the particle column density and the cross-section column density, the amount of material is the easiest way to compare atmospheres for different stellar parameters quantitatively.

To set these quantities on a systematic footing, a new set of moments is defined:

$$\sigma_j = \int_0^\infty \rho L_j dz \quad \forall j \in \mathbb{N} \quad (5.3)$$

In contrast to the classical maximum of the so-called dust-to-gas ratio, which is the ratio of the dust and gas mass densities, the moments σ_j do not refer to one specific atmospheric layer but consider the full atmosphere instead. The advantage of the new method is best shown with an example: A hot atmosphere will not feature a high dust-to-gas ratio in any of its layers because the supersaturation of the gas is comparably weak. Regardless, it may possess a larger amount of material in the solid phase than a cooler atmosphere with a higher dust-to-gas ratio if its supersaturated zone is geometrically thicker. The σ_j consider the full extent of the atmosphere and, thus, represent a more reliable tool.

Evaluation: Now that the altitude-integrated dust moments have been introduced, it is possible to examine non-local quantities over the stellar parameter space. The dust moments ρL_0 , ρL_2 and ρL_3 are shown in the left panels of Fig. 5.12 for two temperature sequences with each a low and a high surface gravity. The same quantities integrated over the altitude are shown on the right of said figure. The left panels exemplify how strongly the local quantities vary. This underlines the importance of integrated quantities for model comparisons.

As demonstrated by the original dust moments L_j , the profiles of the number density L_0 curves (Fig. 5.12, top-left) deviate from the cross-section and volume quantity curves at the bottom of the clouds. Therefore, as mentioned above, it is neither a representative tool for the local opacity nor for the grain volume. Integrated over the altitude, the particle number density (Fig. 5.12, top-right) features a plateau around $T_{\text{eff}}=2000\text{K}$ that is emphasized for lower gravity models. The solid phase has reached a form of saturation at this plateau. Its origin is the backwarming, caused by the cloud itself, that begins to limit the expansion of the cloud with dropping effective temperatures. Below $T_{\text{eff}}=1800\text{K}$, this self-regulation starts to soften up again, because the convection zone starts to withdraw fast for falling

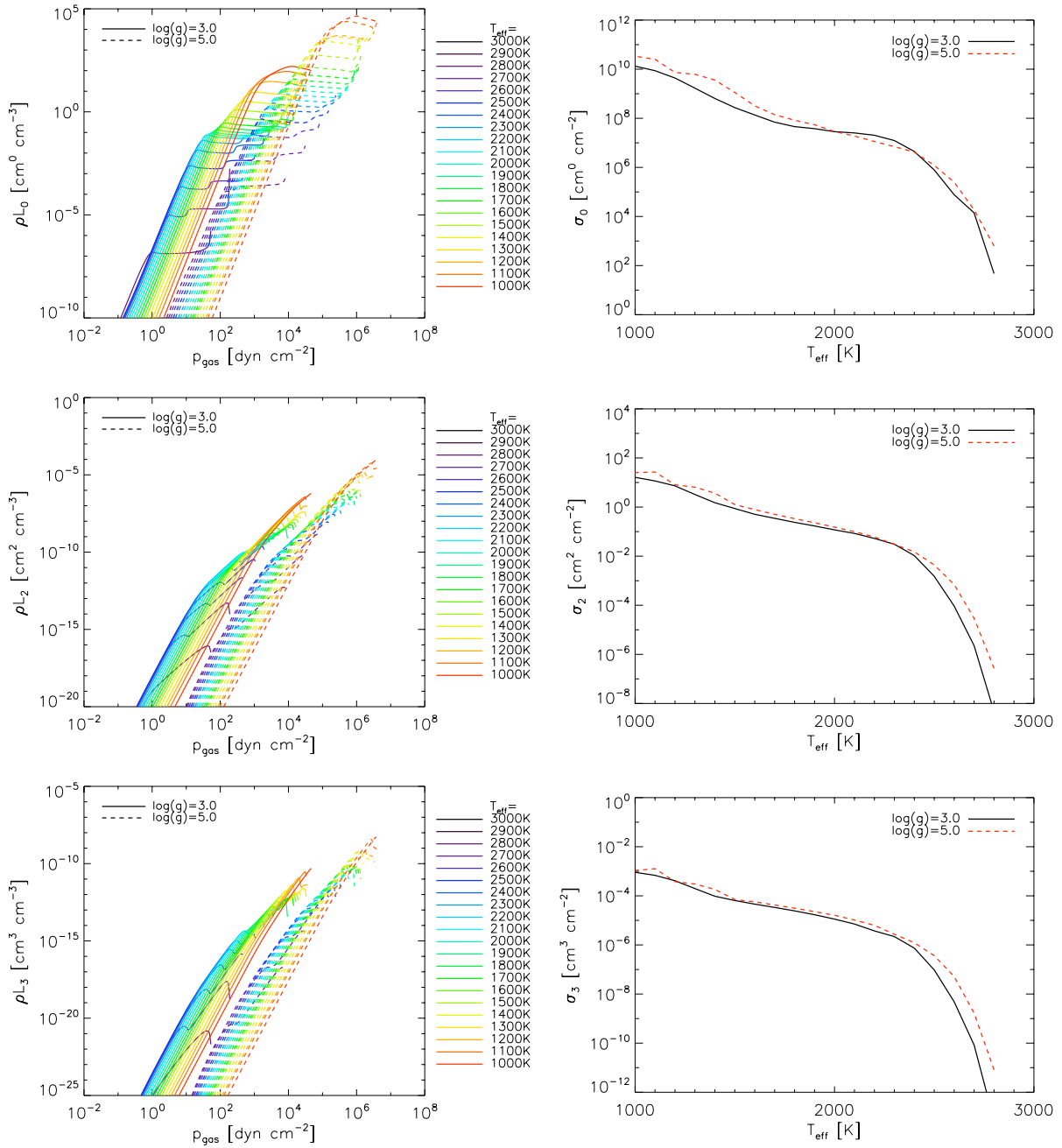
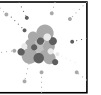


Figure 5.12: The dust moments L_0 , L_2 and L_3 are a measure for the dust particle number, integrated grain surface and integrated grain volume per cm^3 , respectively. An integration over the altitude allows a direct comparison of different models.

effective temperatures. This shifts the cloud to a higher density environment which, in turn, results in a more efficient dust growth. Likewise, the higher density of the envrioning gas is partially suppressing the backwarming. The effective temperature has an immense influence



on the number of the dust particles. In comparison, the spread due to the surface gravity is tiny. In general, models of higher surface gravity feature larger particle numbers within their atmospheres, because the higher density environment overcompensates for the significantly decreased geometrical extension of the clouds. Regardless, a higher gravity typically does not increase the particle numbers by much more than a factor of three. The only exception, where lower gravity models possess larger particle number column densities than respective high gravity models, is the range between $T_{\text{eff}}=2100\text{K}\dots 2300\text{K}$, which is due to a stronger cloud limitation by backwarming.

The second and third dust moment curves (Fig. 5.12, center-left, bottom-left) do not show the same bends as the particle number density. Hence the particle column density is generally not suited to describe the amount of dust within an atmosphere. Similarly, the altitude-integrated quantities σ_2 and σ_3 (Fig. 5.12, center-right, bottom-right) do not possess the same flat plateau around $T_{\text{eff}}=2000\text{K}$ that is prominent for the particle number column density. This means, while the number of dust particles remains nearly constant over a certain range of the effective temperature, the average particles within a vertical column of gas becomes larger for decreasing effective temperatures. Even so, the influence of backwarming is considerable as well with respect to the column densities of the grain cross-section and the grain volume. Thus, below $T_{\text{eff}}=2500\text{K}$, the curves of all σ_j are markedly flatter. Anyhow, dust volume within a gas column rises by three orders of magnitude between $T_{\text{eff}}=2500\text{K}$ and 1000K . For higher effective temperatures, the higher gas density of high gravity atmospheres results in up to one order of magnitude larger average particles within a vertical gas column than for the lower gravity models, i.e., notably larger surface area and volume column densities. As soon as the backwarming becomes relevant, this difference between the σ_j of different gravities vanishes almost completely. In other words, the total grain surface area and total grain volume within a gas column are hardly depending on the surface gravity. This is especially surprising since the gravity varies the geometrical thickness of the dust clouds (Sec. 5.4.2) as well as the fall timescales of dust particles (Sec. 5.4.3) over orders of magnitude. A lower gravity yields a lower gas density at the cloud, which reduces the rate of newly forming particles (e.g., Witte, 2008). Apparently, this is almost fully compensated by the wider extension of lower gravity clouds.

Irrespective of the gravity, the integrated geometrical cross-section of all grains within a gas column exceeds unity below $T_{\text{eff}} \approx 2000\text{K}$. Hence, for these models, optically thick dust clouds can be present, depending on the wavelength. This optical thickness of the clouds coincides with the saturation of the particle numbers column density around $T_{\text{eff}}=2000\text{K}$. Below 1800K , the σ_2 and σ_3 curves become steeper once more for decreasing effective temperatures. As for σ_0 , this effect occurs due to the fast withdrawal of the convection zone, which enables the cloud to sink into layers of higher gas density, thereby, causing a more efficient grain growth. For the coolest models shown in the figures ($T_{\text{eff}} \leq 1500\text{K}$), this gravity-symmetry is weakly broken. The reason for this is the gravity-dependence of the grain composition, which is discussed in the following.

5.5 Grain composition

Zones within the cloud: As noted earlier by Helling & Woitke (2006) and following publications on the dust model (Witte et al., 2009a), the dust clouds feature individual zones with respect to the grain composition. The integration with a model atmosphere code does not change this (Fig. 5.13). The uppermost layers are almost entirely made of the nucleation species TiO_2 , as the growth of other species remains mostly irrelevant there. The first efficient grain growth is dominated by silicate species. The volume fractions of individual silicates at this region is hardly influenced by the stellar parameters. Eventually, silicates begin to evaporate while the efficiency of solid iron growth rises, resulting in iron-heavy grains. Slightly deeper within the atmosphere, the iron vanishes almost instantly from the solid phase and leaves behind almost pure Al_2O_3 [s] with a tiny fraction of TiO_2 [s]. In contrast to the silicate region where the grain composition is almost unaffected by the stellar parameters, the peaks of the dominant Fe [s] and Al_2O_3 [s] are affected by the local gas density and temperature. Typically, a cloud which reaches into more dense and hot layers of the atmosphere features a higher solid iron peak while the Al_2O_3 [s] vanishes slowly. Such clouds are the result of lower effective temperatures, higher gravities or lower metallicities. It is noteworthy that the Fe [s] and Al_2O_3 [s] regions are absent in the models for $T_{\text{eff}} \leq 1000\text{K}$ and 1100K , respectively. The maximum volume fraction of the Al_2O_3 [s] begins to fade slowly with decreasing effective temperature. Below 1500K , the convection zone is withdrawing

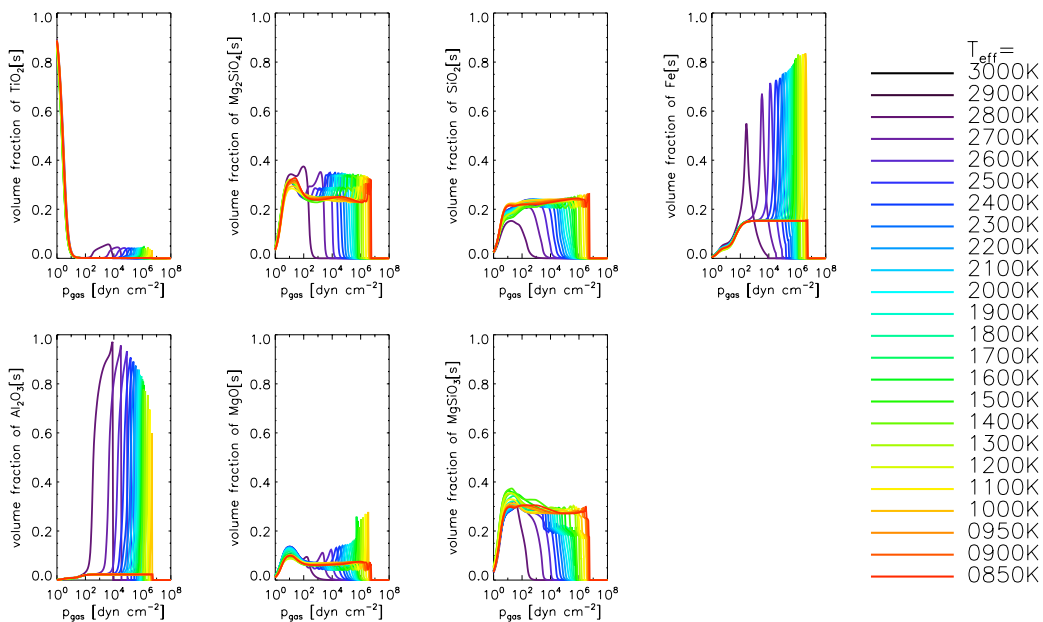
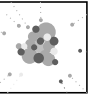


Figure 5.13: The typical dust cloud features 4 different regions with respect to the mean grain composition. Each is dominated by one kind of solids: TiO_2 [s], silicates, Fe [s], Al_2O_3 [s] (from cloud top to bottom). The shown models correspond to $\log(g)=5.0$ and solar abundances. (Compare to Witte, 2008, Fig. 6.16)



inwards very quickly for lower effective temperatures, which shifts the cloud to higher gas densities and, therefore, accelerates the disappearance of this zone. The final fading of $\text{Al}_2\text{O}_3[\text{s}]$ -dominated layers takes place very abrupt, dropping from 60% to zero within less than 100K of effective temperature for high gravity models. For lower gravity models, the disappearance of this zone is still abrupt but spreads over a slightly wider range of effective temperature. The same mechanism clears the $\text{Fe}[\text{s}]$ -dominated layers of the cloud. Since these layers are situated slightly higher within the cloud, they vanish at slightly lower effective temperatures. In contrast to the solid aluminium oxide, the maximum volume fraction of solid iron is increasing from $T_{\text{eff}}=2800\text{K}$ down to 1000K. This trend makes the sudden loss of the iron-dominated zone, which is occurring because of the inwards-shift of the convection zone, even more harsh.

The four different cloud regions with respect to the grain composition exist in basically all clouds throughout the stellar parameter space (Fig. 5.13), even for extreme metallicities down to $[\text{M}/\text{H}]=-4.0$. Only for even lower metal abundances the composition deviates strongly from the typical state, which is predominantly a result of a shift in the chemical equilibrium of the gas phase. On the other hand, such chemical equilibrium shifts, resulting in changed grain compositions, may as well be caused by tweaking abundance ratios. For instance a lower than usual $[\text{Mg}/\text{Si}]$ would result in a higher volume fraction of SiO_2 while the Mg-bearing compounds would be suppressed. In fact, such variation in the element abundance pattern have been observed for different stellar generations (e.g., Frebel et al., 2008), i.e., objects of considerably lower metal abundances.

The standalone dust models by Helling et al. (2008c) feature additional solid species. None of those species is able to form its own domain with respect to the grain composition. Despite this, it is possible that alkali and alkaline earth compounds as well as metal-rich silicates, which are known to have a growing influence in low temperature condensates of igneous rock (e.g., Mueller & Saxena, 1977) could form own zones of dominance. Approaching temperatures and densities of old planetary atmospheres, it will be strictly required to introduce solid species such as water ice and compounds of ammonia and sulfur. Currently, the model is simply lacking the data to take such species into account. As mentioned above, the stiffness of the system of equations of the dust model increases with the number of solid species. The current numerics are unable to solve this system for considerably higher numbers of solid species. Hence, before significant improvements can be achieved with respect to the grain composition, the numerics will have to be revised.

Currently, the composition at the silicate-dominated zone is hardly affected by the stellar parameters. One consequence of additional solid species could be a diversification of this zone, which would imply systematic errors in the current chemistry and opacity calculation.

Mean composition of the cloud: Although the exact composition at the different zones of the clouds determines the local dust opacity, the global influence of the individual solids is not directly comparable this way. Therefore, additional dust volume column densities are

introduced for the individual species s , based on Eq. 5.3:

$$\sigma_{3,s} = \int_0^{\infty} \rho L_{3,s} dz \quad \forall s \in [0, S] \quad (5.4)$$

Divided by σ_3 , the average volume fraction of the solid species within a vertical gas column are determined, which are shown in Fig. 5.14. For clarity, the four silicate species ($\text{SiO}_2[s]$, $\text{MgO}[s]$, $\text{MgSiO}_3[s]$, $\text{Mg}_2\text{SiO}_4[s]$) are not displayed individually but are summed. Unlike other solid species, the relative numbers between the silicate species are not changing much over the effective temperature and surface gravity for solar element abundances.

In all of the hottest dust-bearing models, $\text{Al}_2\text{O}_3[s]$ is effectively the only relevant solid species in terms of the grain volume, while all other species combined contribute less than 5% of the solid material volume. As mentioned above (Sec. 5.4.4), the cloud begins to vaporize its own lower layers through backwarming. Since the aluminium compound and $\text{TiO}_2[s]$ dominate the bottom of the cloud, both species slowly decrease their contribution for increasing dust opacity, i.e., decreasing effective temperatures. Due to the more compact nature of clouds in higher gravity atmospheres, the backwarming has a greater impact than in low gravity models, which means the fraction $\sigma_{3,s}/\sigma_3$ is decreasing faster for decreasing effective temperatures. Whereas those two species decrease their contribution to the dust volume within a vertical gas column, the silicates and solid iron rise in importance. Starting below $T_{\text{eff}}=2700\text{K}$ in the case of high gravity atmospheres, $\text{Fe}[s]$ is already the second most

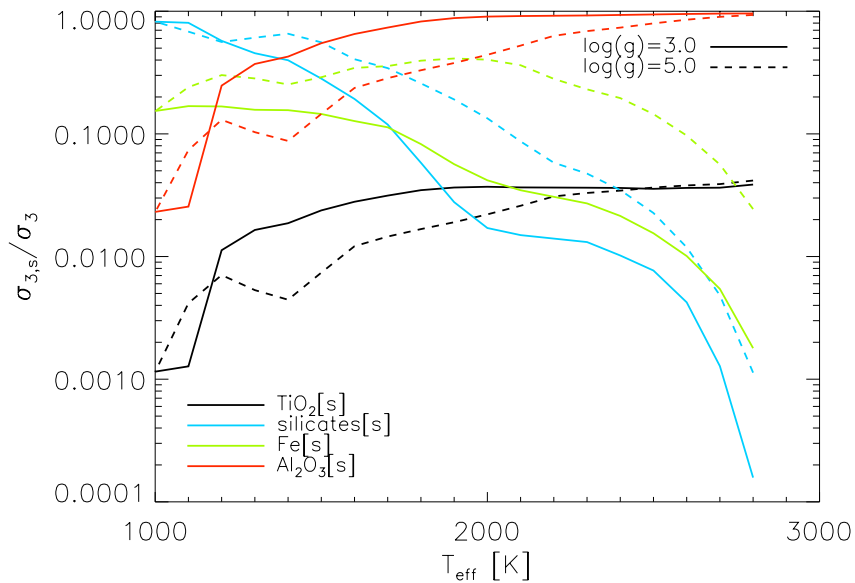
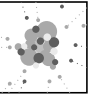


Figure 5.14: Column density of the solid species volume as fraction of the total grain volume column density. The composition of the average dust grains within a vertical gas column is changing with the stellar parameters.



important species. For lower surface gravities, $\text{TiO}_2[\text{s}]$ remains the second most important solid above $T_{\text{eff}}=2100\text{K}$. The volume of the silicate species remains irrelevant in the hottest models. Combined, they reach the 5% level of the dust volume for $T_{\text{eff}} \approx 2300\text{K}$ in a high gravity environment and for $T_{\text{eff}} \approx 1800\text{K}$ in low gravity atmospheres.

Section 5.4.4 has shown that the integrated model grain cross-section within a vertical gas column model clouds becomes large enough to cover the full surface area of the dwarf or planet around $T_{\text{eff}} \approx 2000\text{K}$. Thus, the cloud can turn optically thick for lower effective temperatures. Therefore, the backwarming effect will become considerably stronger. Because of this, the lower altitude cloud layers are unable to form, leaving behind only the higher altitude layers which are dominated by silicates. Thus, the silicates volume fraction within the gas column rises quickly below $T_{\text{eff}} \approx 2000\text{K}$ while $\text{Al}_2\text{O}_3[\text{s}]$, $\text{TiO}_2[\text{s}]$ and $\text{Fe}[\text{s}]$ begin to drop.

For the higher gravity models, there is a small window in the effective temperatures wherein iron is the most important solid species ($\sim 40\%$). Anyway, aluminium-oxide and the silicates contribute almost identical amounts ($\sim 30\%$) to the dust volume at this effective temperature range. Following this range of dominant solid iron, the silicates become the most important species while all other species becomes less important for decreasing effective temperatures. Lower gravity models skip the effective temperature range of dominant solid iron completely because their iron volume fraction never exceeds 20%. Around $T_{\text{eff}} \approx 1000\text{K}$ silicates amount to some 80% of the total dust volume of the models.

The volume contribution by $\text{Al}_2\text{O}_3[\text{s}]$ and $\text{TiO}_2[\text{s}]$ exhibits a series of bumps for $T_{\text{eff}} \leq 1500\text{K}$, which are magnified by higher surface gravities. Their origin is the superposition of two effects. The first one is the growing backwarming that reduces the amount of both solid species. The shift of the cloud to a higher density environment with decreasing effective temperature counteracts the reduction around $T_{\text{eff}} = 1200\text{K}$ and causes a re-increase of the volume fractions of both species. For even lower effective temperatures, this counteracting effect is unable to keep up with the backwarming. As a result, $\text{Al}_2\text{O}_3[\text{s}]$ drops to merely 2% of volume contribution to the solid material within the atmosphere by $T_{\text{eff}} = 1000\text{K}$ while $\text{TiO}_2[\text{s}]$ becomes even less relevant for the grain growth.

In general, the contributions of the individual solids meet expectations. The most abundant, high temperature condensates such as $\text{Al}_2\text{O}_3[\text{s}]$ dominate the clouds in the hottest dust-bearing models. For cooler atmospheres, these species are replaced, first by solid iron and later by silicates. With the dominance of the silicate species, the dust grains have become more alike to igneous rock as we know it from Earth's crust.

Solid phase element abundances: The previous paragraphs have discussed the molecular composition of the dust cloud. In the following, the same is done briefly for the composition with respect to the chemical elements.

Analogous to the definition of the gas phase element abundances ϵ_e , solid phase abundances $\epsilon_{\text{solid},e}$ are introduced for all elements $e \in [0, E]$. For convenience, these values are expressed by relative numbers, i.e., fractions of the total number of elements in the solid phase $\epsilon_{\text{solid},e} / \sum_{e=1}^E \epsilon_{\text{solid},e}$. These quantities can be traced back to the species-dependent

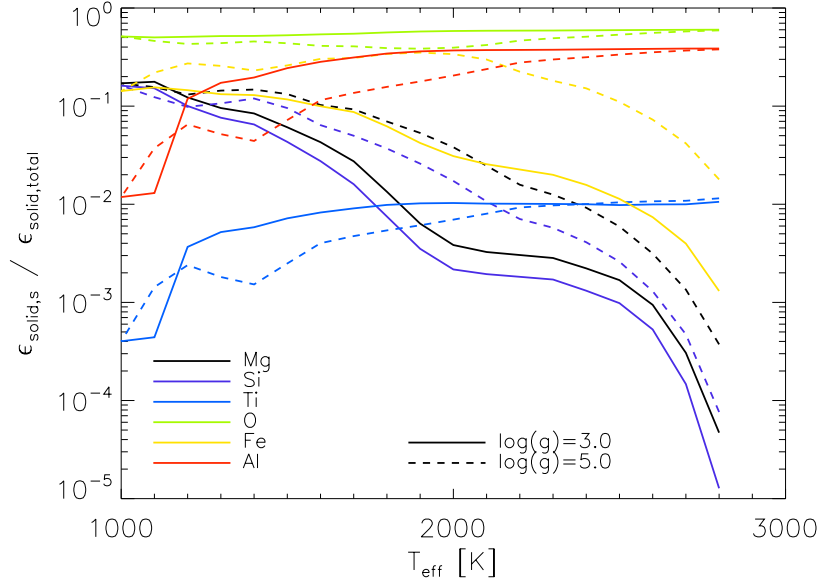


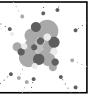
Figure 5.15: Abundance of element e in the solid phase divided by the total abundance of all solid elements. Just as the mean grain composition, the abundances in the solid phase are a function of the stellar parameters.

dust moments $L_{3,s}$:

$$\frac{\epsilon_{\text{solid},e}}{\epsilon_{\text{solid,total}}} = \frac{\epsilon_{\text{solid},e}}{\sum_{e=0}^E \epsilon_{\text{solid},e}} = \frac{\sum_{s=0}^S \frac{\nu_{e,s}}{\Delta V_s} L_{3,s}}{\sum_{e=0}^E \sum_{s=0}^S \frac{\nu_{e,s}}{\Delta V_s} L_{3,s}}, \quad (5.5)$$

where ΔV_s is the monomer volume of species s , again, and $\nu_{e,s}$ corresponds to the stoichiometric coefficient of element e in species s .

These relative abundances can be understood as individual contributions of the six considered chemical elements. These contributions are shown in Fig. 5.15 as functions of the effective temperature for a high and a low gravity model sequence, respectively. Irrespective of the stellar parameters, roughly every second atom in the solid phase is an oxygen atom. This high contribution is not surprising, since oxygen is by far the most abundant element contributing to the dust growth. For hotter models, the oxygen contribution can be as high as 60%, with the remaining material almost entirely made of aluminium. Around $T_{\text{eff}}=2000\text{K}$, the clouds in high gravity atmospheres are dominated by solid iron, which decreases the oxygen fraction to some 40%. In these models, Al and Fe contribute roughly 30% to the total number of elements within the solid phase. The elements Mg and Si remain far below 1% of the total solid phase abundances for $T_{\text{eff}} \geq 1800\text{K}$ in case of $\log(g)=3.0$. For the higher gravity atmospheres, a comparable significance of Mg and Si is reached for



approximately 500K higher effective temperatures. In general, the contributions of Fe, Mg, and Si are increased at the expense of Al and Ti for higher gravity and lower effective temperatures. For the coolest model atmospheres, the diversity of the element contribution with the surface gravity has vanished. Titanium and aluminium are effectively absent from the average grains, there. These clouds are composed of some 50% oxygen with almost equal 16% admixture of silicium, magnesium and iron.

5.6 Metallicity

Extreme metal abundances: The presence of dust particles is a key aspect of the collapse of gas clouds to stellar and substellar objects. The Jeans criterion (Jeans, 1902) suggest that less massive gas cloud fragments are less susceptible to collapse. Even if it is theoretically able to contract at all, the respective timescales rise fast (e.g., Hayashi & Nakano, 1963) which increases the chances for destructive external perturbation. Simulations by Omukai (2008) and Clark et al. (2008) suggested that such formation of substellar objects via collapse is

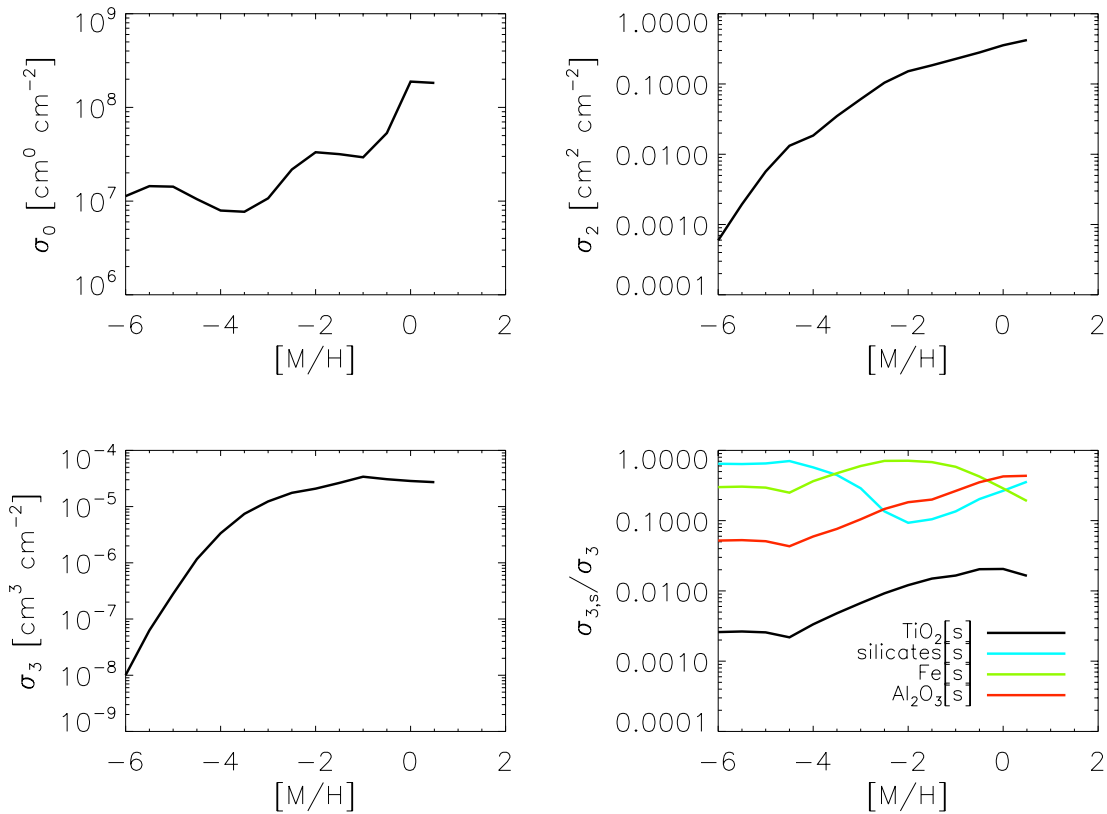


Figure 5.16: The altitude-integrated dust moments as function of the metallicity for $T_{\text{eff}}=1800\text{K}$ and $\log(g)=5.0$.

possible for $[M/H] \geq -6.0$ presuming that the metals are predominantly bound by dust grains which would serve as a cooling agent for the initial gas clouds. According to observations of halo stars (e.g., Frebel et al., 2005), there is a steep decline in the number of objects with $[M/H] < -4.0$ which is likely due to heating effects caused by the formation of H_2 (Omukai, 2008).

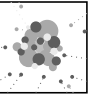
Witte (2008) and Witte et al. (2009a) investigated dust formation in extremely metal-poor atmospheres. Building on those results, the altitude-integrated dust moments are shown in Fig. 5.16.

Comparing σ_0 with σ_2 and σ_3 clearly points out that the dust particle number column density is not a good indicator for the dust opacity or the amount of dust. The dust particle number column density σ_0 as a function of metallicity sports a series of rolling minima and maxima. The most relevant maximum exists for solar metallicity. Counterintuitively, a raise of the metal abundances beyond solar values does not increase the number of dust particles. The reason for this is the hotter atmosphere, which stops the formation of new dust particles slightly higher within the atmosphere. This compensates the higher formation efficiency due to larger amounts of reactants. For subsolar abundances near the solar value, the curve is more in agreement with intuitive expectations in form of dropping dust particle numbers. Between $[M/H] = -1.0$ and -2.0 , the column density of the dust particle number features a plateau. It is a result of the vanishing backwarming effect, which allows the cloud to persist deeper into atmosphere, significantly increasing the descent timescale of the dust grains. For $[M/H] = -2.0 \dots -3.5$, the cloud is no longer able to expand further inwards, i.e., it has reached a minimum altitude. At about the same metallicities, the upper atmosphere develops a temperature inversion that prohibits the formation of dust particles there. The number of dust particles within a vertical gas column drops once more and reaches its absolute minimum. In the models of even lower metallicity, the gas has become cool enough to permit nucleation across the full extension of the cloud down to the bottom layers. As result, σ_0 is raised by one third of an order of magnitude, even though the metal abundances decrease by more than one order of magnitude.

Across the full range of six orders of magnitude in the metal abundances, the column density of dust particles decreases by a mere factor of twenty. In other words, the inwards shift of the dust cloud and the cooling of the atmosphere compensates much of decreasing metallicity effects with respect to the dust particle number.

Though the same factors that alter σ_0 over the metallicity also affect σ_2 and σ_3 , both show only weak kinks around the maxima and minima of σ_0 . The cross section column density σ_2 decreases monotonically with the metallicity. Especially for the near-solar metallicities, the altitude-integrated dust particle cross section decreases only slowly with $[M/H]$, which is a result of the inwards-shift of the cloud, again. Over six and a half orders of magnitude in the metal abundances, the integrated cross-section decreases by less than three orders of magnitude.

The dust volume within a vertical gas column shows more interesting reactions to the metallicity. The maximum volume is achieved around $[M/H] = -1.0$. For near-solar abundances the amount of dust with respect to the grain volume is lower. The inwards-shift of the cloud for decreasing metallicity causes growing particle sizes at the bottom of the cloud and ultimately results in this maximum of σ_3 even though the metal abundances in the at-



mosphere are much smaller than for solar metallicity. Similarly noteworthy is the very weak decrease of σ_3 down to $[M/H]=-3.5$. Between $[M/H]=-3.5$ and -1.0 , there is merely half an order of magnitude difference in the dust volume and even less when compared to the solar dust volume within a vertical gas column. Only for much lower metal abundances, the dust volume begins to drop linearly with the metallicity due to the onset of decreasing dust particle sizes across the cloud.

As indicated by the σ_j , the amount of dust is all but a linear function of the metallicity. Even for the lowest considered metal abundances, the amount of dust remains remarkably high because the shift of the cloud into a higher density environment compensates much of the decreasing metal abundances while self-limiting factors such as the backwarming become negligible very fast. Such an efficient dust formation speaks in favour of the high condensation rates required for a sufficiently fast collapse of gas clouds as presupposed by Omukai (2008).

With the shift of the dust cloud, caused due to variation of the metal abundances, the contribution of the different solid species to the material of the cloud varies as well. Clouds like those for near-solar abundances feature a comparably low gas density in their environment. In such clouds the zone that is dominated by $\text{Al}_2\text{O}_3[\text{s}]$ typically also dominates the dust volume column density σ_3 . A decrease of the metallicity reduces the collision rates between all species of the chemical system that involve metals. This has a critical impact on the chemistry, favouring less complicated molecules due to lower collision rates. This way, the reactants which are required to form $\text{MgSiO}_3[\text{s}]$, $\text{Mg}_2\text{SiO}_4[\text{s}]$ or $\text{Al}_2\text{O}_2[\text{s}]$ become very rare. Hence, the contribution by those solids is decreasing with the metallicity. At the same time, iron requires only single atoms as solid monomers. Therefore, iron quickly becomes the dominant species between $[M/H]=-1.0$ and -3.5 . Initially the volume contribution by all other solid species decreases fast with the metallicity. However, below $[M/H]=-2.0$ the environment of the clouds has become so cool and dense that more and more MgO , another very simple monomer, condenses and remains in the solid phase for a long time. By $[M/H]=-4.5$, all other solids besides $\text{MgO}[\text{s}]$ and $\text{Fe}[\text{s}]$ are nearly absent, together contributing less than 6% of the dust volume. For lower metallicities, the composition appears to remain constant.

Influence of different abundance patterns: The element abundances of a stellar atmosphere are often the result of the nucleosynthesis of several star generations. Following the big bang, the primordial element abundances were determined by the expansion/cooling of the universe as well as the interaction rates between fundamental particles (e.g., Schneider, 2006). The resulting gas was a mixture of $\sim 94\%$ hydrogen (^1H) and $\sim 6\%$ helium (^4He) with almost non-existent amounts of heavier elements. Since the formation of the first generation of stars, the high densities and temperatures of the stellar cores permitted the fusion of elements which enriched the gas with elements up to iron. Incidents of extremely high energy-densities such as supernovae are able to produce even more massive elements. This continuous enrichment affects the properties of consecutive star generations. Therefore, the enrichment is not a linear process, which means that the relative abundances of the various elements vary between stellar generations. With the dependence on the local history of en-

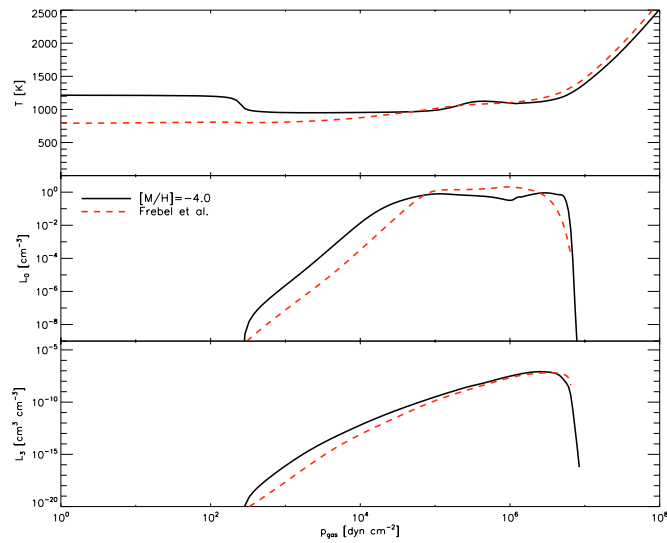


Figure 5.17: Comparison of two models for $T_{\text{eff}}=2000\text{K}$ and $\log(g)=5.0$ and different abundance patterns. The *solid* curves correspond to a $[M/H]=-4.0$ model for solar abundances defined by Asplund et al. (2005) while the *dashed* curves correspond to ultra-metal-poor abundances observed by Frebel et al. (2008). From top to bottom, the panels show the gas temperature, the dust particle number density and the dust volume density across the atmospheres.

riching incidents, these relative abundance may also vary strongly with the site where a new star forms.

The variations of relative abundances is most evident when comparing younger stars with older stellar generations, e.g., comparing an object with a solar abundance pattern and an object from the galactic halo. Beers & Christlieb (2005) and others have studied extremely metal-poor stars in order to deduce a systematic variation of the element abundance pattern over the age of the universe. Frebel et al. (2008) have reported the discovery of an old halo star and derived element abundances for this object with suspected $[\text{Fe}/\text{H}] < -5.0$. Based on their inferred element abundances, a sample atmosphere model for $T_{\text{eff}}=2000\text{K}$ and $\log(g)=5.0$ was calculated. Although the $[\text{Fe}/\text{H}]$ is lower than -5.0 , all the remaining abundances come closer to $[M/H] \approx -4.0$ in case that $[M/H]$ is defined by the results of Asplund et al. (2005). In figures 5.17-5.19 such a model is compared to the sample model for the element abundances derived by Frebel et al. (2008). A more brief discussion of this, including Fig. 5.19, has been published by Witte et al. (2009a).

All shown curves for the model using the Frebel abundances are smoother than those for the scaled Asplund abundances. In contrast to the model for the simply scaled abundances, the observed abundance pattern avoid a temperature inversion that cuts off the dust cloud above $3 \cdot 10^2 \text{ dyn/cm}^2$ (Fig. 5.17). In the upper parts of the cloud, the model for the Frebel abundances features less dust particles which also reduces the total volume of dust particles at the given altitude. Deeper inside the atmosphere, the Frebel abundances model does not

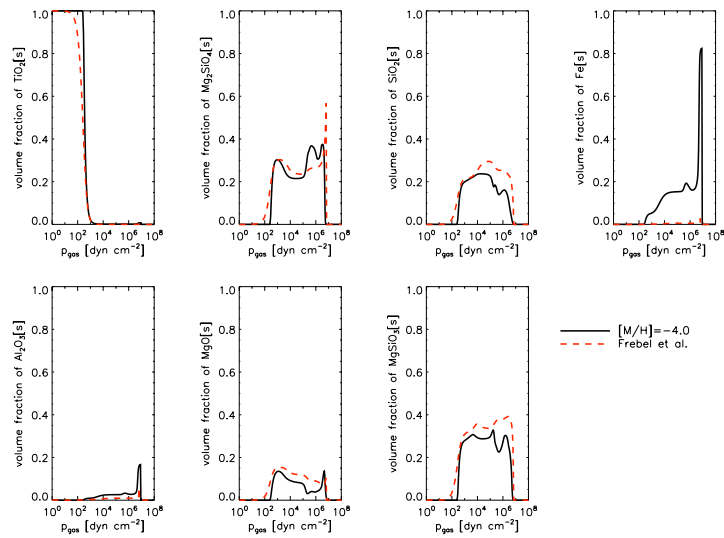


Figure 5.18: Influence of different abundance patterns on the composition of dust grains. The shown models correspond to simple scaled solar abundances with $[M/H]=-4.0$ (*solid*) and the abundances found by Frebel et al. (2008) (*dashed*).

feature the bump in the temperature structure which is present in the scaled abundance model (described by Witte, 2008). This results in locally higher particle numbers. At the same altitude, both models possess a nearly identical distribution of the dust particle volume. In other words, the strong change of the element abundances has a surprisingly weak impact on the amount of dust at the bottom of the cloud. The difference in the abundance pattern is most striking in the mean grain composition (Fig. 5.18). With aluminium and iron being much more rare in the model for the Frebel abundances, $\text{Al}_2\text{O}_3[\text{s}]$ and $\text{Fe}[\text{s}]$ are nearly absent. Their volume fraction, which is otherwise significant at the bottom of the cloud, is redistributed to the more simple silicate species. With its more authentic element abundances, the spectrum of the model for the Frebel abundances shows a markedly changed appearance (Fig. 5.19). Comparably strong water bands dominate the near infrared, while the influence of the alkali lines is significantly larger in the red-optical wavelength range.

This comparison shows that the dust cloud reacts strongly to changed element abundances in terms of the mean grain composition. However, the dust volume density L_3 is rather weakly affected. Because of the low metal abundances of the models, the most significant differences in the spectra are independent from the dust cloud but instead are gas phase effects. In any case this example meets expectations that simple metallicity model sequences are unable to account for significant abundance pattern deviations between stellar generations or different formation sites.

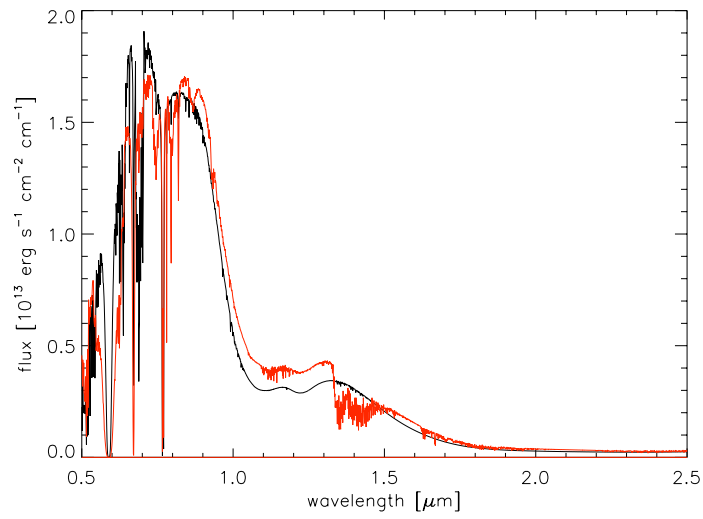
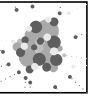


Figure 5.19: Comparison of sample spectra corresponding to simple scaled solar abundances with $[M/H]=-4.0$ (*black*) and the abundances found by Frebel et al. (2008) (*red*).



6 Results: Testing of models on observations

Although interesting by itself, the analysis of the models is inconsequential without a reference to the real world. For this reason, a systematic comparison with observational data was carried out. This analysis is required to identify weaknesses or even outright flaws of the model and to determine the range of the stellar parameter space over which the models can be considered useful.

The content of this chapter has been published recently by Witte et al. (2011). While the publication focused on the discussion of individual objects, this section concentrates on the identification of flaws of the model.

6.1 Observational data and fitting process

Several hundred near-infrared low resolution spectra of M, L and T type dwarfs taken with the SpeX spectrograph were retrieved from Gelino et al. (2009, *DwarfArchive.org*).

The observations have been fitted with the latest model grid in order to derive stellar parameters for the respective objects. The plain χ^2 minimization was performed for normalized spectra. The considered wavelength range was limited to 0.7...2.4 μm in order to avoid a bias due to the often very noisy edges of the observed spectra. Typically, the determination of stellar parameters via standard χ^2 puts an emphasis on the matching of absorption features. Therefore, the goodness-of-fit, as defined by Burgasser et al. (2009), was used as a quality criterion for individual fits in order to identify the best fit in the stellar parameters space, because it provides a more balanced consideration of the full wavelength range. In ambiguous cases, e.g., due to degeneracy of the goodness-of-fit, the fits were checked by eye to obtain the most reasonable stellar parameters. In order to match the resolution of the observed data ($R \sim 300$), the synthetic spectra were smoothed by a Gaussian convolution and were consecutively binned down.

A number of observations were too noisy to be reproduced satisfyingly by any of the models. Such noisy observational data sets that combined overly large goodness-of-fit values with complete mismatches of characteristic features of the corresponding spectral type and strong ambiguities with respect best fitting stellar parameters were excluded from further investigations. Other objects which have been noted for peculiarities that exhibited unusually high goodness-of-fit values were sorted out of the sample. Likewise, objects that have been reported as unresolved binaries, often showed unsatisfying fits, i.e., too high goodness-of-fit. These objects were also left out of the subsequent investigations.

This way, the number of considered data sets was reduced to 108. The number of remaining

individual objects is 105. For one M dwarf (2MASS J23515044-2537367), there are three distinct observations. Their best fits agree well with each other within the range of the fitting errors. Similarly, the agreement between the best fits for the two different observations of the L dwarf 2MASS J2057540-025230 is very good. Both of these examples show that the fitting process works consistently and remains stable for smaller variations of the input spectra.

6.2 Effective temperature-spectral type sequence

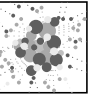
The resulting best fitting parameters of the 108 qualified observations are shown in Tab. 6.1-6.2. In addition, sixteen fits are shown in Fig. 6.1-6.4 and discussed in the following.

Mid- to late M-dwarfs: The range of spectral types is dominated by some of the lowest mass stars. Representative fits of selected objects are shown in Fig. 6.1.

The earliest spectral type that is covered by the model grid is the type M6. However, according to the best fitting models, spectral types earlier than M8 typically do not possess dust clouds. As the example of J04035944+1520502 (Fig. 6.1, top-left) proves, the spectra of such objects are typically very well reproduced by the models.

Within the hottest atmospheres that can sustain dust, the direct influence of the cloud on the spectrum is still hardly detectable because there are only few dust grains which are mostly transparent. Unlike the dust opacity, the gas phase depletion becomes significant almost instantly below the critical temperatures that correspond to the stability of individual solids. The clouds of the hotter atmospheres are dominated by high temperature condensates such as $\text{Al}_2\text{O}_3[\text{s}]$ and $\text{TiO}_2[\text{s}]$, as shown in Sec. 5.5. Therefore, the elements Al and Ti are considerably less abundant in the gas phase at the cloud layers, which means that the clouds can be detected indirectly. As the dust opacity increases for decreasing effective temperatures, the higher density layers below the cloud are quickly blanketed. This magnifies the perceived gas phase depletion (Sec. 5.1). This way, the prominent TiO absorption features begin to fade quickly for the late M dwarfs.

Examples of the earliest dust-bearing objects with respect to the spectral type are J00115060-1523450 and J00335534-0908247 (Fig. 6.1, top-right and bottom-left, resp.). A comparison by eye of the spectra of both objects reveals no significant differences. According to the best fitting models, the latter object features a slightly lower surface gravity, pointing to a rather young age. However, it must be noted that the wide range, low resolution fitting method, employed for this work, results in a very flat goodness-of-fit distribution over the surface gravity for the late M-dwarfs, hence, large $\log(g)$ error bars. Hence, surface gravities of such objects which have been inferred in this work must not be over-interpreted. For a more reliable determination of the surface gravity of late M dwarfs, higher-resolution studies of gravity-sensitive absorption features are necessary. Accepting the younger age of J00335534-0908247, it distinguishes itself from J00115060-1523450 by a slight shift of flux from the red optical range into the H band, which is accompanied by marginally weaker FeH features but slightly stronger H_2O and CO bands. These features are candidates for upcoming studies on gravity sensitivity.



object designation	observation			DRIFT-PHOENIX best fit			
	optical SpT	NIR SpT	observation by	$T_{\text{eff}}[K]$	$\log(g)$	$[M/H]$	goodness-of-fit
2MASS J00013044+1010146	-	M6	Burgasser et al. (2004)	2900	4.5	+0.3	1.19
2MASS J00583814-1747311	-	M6	Burgasser et al. (2004)	2900	4.5	-0.0	2.18
2MASS J01532750+3631482	-	M6	Burgasser et al. (2004)	2900	5.0	-0.0	1.56
2MASS J18244344+2937133	-	M6	Burgasser et al. (2004)	3000	4.5	-0.0	2.57
LEHPM2-461	M6.5	M7	Burgasser et al. (2008)	2900	4.5	+0.3	0.90
2MASS J04035944+1520502	-	M7	Burgasser et al. (2004)	3000	5.0	-0.0	1.72
2MASS J15243203+0934386	-	M7	Burgasser et al. (2004)	2800	4.0	-0.0	0.80
2MASS J11323833-1446374	-	M7	Burgasser et al. (2004)	2900	4.5	-0.0	0.72
CFHT4	M7	-	Muench et al. (2007)	2900	5.0	-0.0	0.06*
MHO4	M7	-	Muench et al. (2007)	2900	4.5	-0.0	0.01*
SO0253+1625	M7	-	Burgasser et al. (2008)	2900	4.5	+0.3	2.76
VB8	M7	-	Burgasser et al. (2008)	2800	4.0	-0.0	3.38
ITG2	M7.25	-	Muench et al. (2007)	2900	5.0	+0.3	0.01*
2MASS J00115060-1523450	-	M7.5	Burgasser et al. (2004)	2700	4.5	-0.0	1.10
2MASS J20491972-1944324	-	M7.5	Burgasser et al. (2004)	2800	4.5	-0.0	5.84
2MASS J01470204+2120242	-	M7.5	Burgasser et al. (2004)	2800	4.5	-0.0	5.18
KPNO2	M7.5	-	Muench et al. (2007)	2900	4.5	-0.0	0.01*
KPNO5	M7.5	-	Muench et al. (2007)	2900	4.0	+0.3	0.01*
CFHT6	M7.5	-	Muench et al. (2007)	2900	3.5	+0.3	0.02*
2MASS J11150577+2520467	-	M7.5	Burgasser et al. (2004)	2900	5.5	+0.3	1.14
CFHT3	M7.75	-	Muench et al. (2007)	2800	4.5	-0.0	0.03*
2MASS J04414825+2534304	M7.75	-	Muench et al. (2007)	2800	4.5	+0.3	0.01*
2MASS J00335534-0908247	-	M8	Burgasser et al. (2004)	2700	4.0	-0.0	5.03
2MASS J23515044-2537367	M8	M8	Burgasser et al. (2008)	2500	4.5	-0.0	8.36
2MASS J23515044-2537367	M8	M8	Burgasser et al. (2008)	2600	4.5	-0.0	4.05
2MASS J23515044-2537367	M8	M8	Burgasser et al. (2008)	2700	5.0	-0.0	2.29
2MASS J00552554+4130184	-	M8	Burgasser et al. (2004)	2700	4.0	-0.0	7.22
2MASS J12121714-2253451	-	M8	Burgasser et al. (2004)	2900	4.5	-0.0	1.13
2MASS J14171672-0407311	-	M8	Burgasser et al. (2004)	2800	4.5	-0.0	0.74
2MASS J17364839+0220426	-	M8	Burgasser et al. (2004)	2800	4.5	-0.0	5.25
LRL405	M8	-	Muench et al. (2007)	2900	5.5	-0.0	0.50*
VB10	M8	M8	Burgasser et al. (2004)	2700	4.5	+0.3	8.85
2MASS J11395113-3159214	M8	M9	Looper et al. (2007)	2500	3.5	-0.3	6.34
LEHPM1-6443	M8.5	M8	Burgasser et al. (2008)	2700	4.5	-0.0	4.66
2MASS WJ0320284-044636	-	M8.5	Burgasser et al. (2008)	2500	3.5	-0.3	2.29
KPNO9	M8.5	-	Muench et al. (2007)	2100	5.5	-0.0	4.18*
LP944-20	M9	-	Burgasser et al. (2008)	2000	5.5	+0.3	12.6
2MASS J11240487+3808054	-	M8.5	Burgasser et al. (2004)	2500	5.0	-0.0	6.58
LHS2924	M9	-	Burgasser & McElwain (2006)	2500	4.0	-0.0	16.6
2MASS J1253+2728	-	M9	Sheppard & Cushing (2009)	2600	4.5	-0.0	2.23
KPNO12	M9	-	Muench et al. (2007)	2700	4.0	-0.0	0.03*
2MASS LJ2107316-030733	-	M9	Burgasser et al. (2004)	2000	5.5	-0.0	5.53
2MASS J04574903+3015195	M9.25	-	Muench et al. (2007)	2600	3.5	-0.0	0.01*
DENIS J124514.1-442907	M9.5	M9	Looper et al. (2007)	2000	5.5	-0.0	3.81
2MASS J01415823-4633574	L0	L0	Kirkpatrick et al. (2006)	1700	4.0	-0.0	1.46
2MASS PJ0345432+254023	L0	-	Burgasser & McElwain (2006)	1900	5.5	-0.0	2.01
2MASS J1230+2827	-	L0	McElwain & Burgasser (2006)	1800	5.0	-0.0	0.50
2MASS J12212770+0257198	L0	-	Burgasser et al. (2008)	1900	5.5	-0.0	2.37
2MASS WJ0228110+253738	L0	L0	Burgasser et al. (2008)	1800	5.5	-0.0	1.99
HD89744B	L0	L0	Burgasser et al. (2008)	1900	5.5	-0.0	2.68
2MASS J02271036-1624479	L1	-	Burgasser et al. (2008)	1800	5.5	-0.0	1.88
2MASS WJ0208183+254253	L1	-	Burgasser et al. (2008)	1800	5.5	-0.0	1.55
GJ1048B	L1	L1	Burgasser et al. (2008)	1800	5.5	-0.0	2.09
SDSS J104842.84+011158.5	L1	L4	Burgasser et al. (2008)	1900	5.5	-0.0	1.38
2MASS J15200224-4422419A	-	L1.5	Burgasser et al. (2007)	1900	5.0	+0.3	2.25
2MASS WJ1439284+192915	L1	-	Burgasser et al. (2004)	2100	5.0	+0.3	6.62
2MASS J2057540-025230	L1.5	L1.5	Burgasser et al. (2004)	1900	5.0	+0.3	2.79
2MASS J2057540-025230	L1.5	L1.5	Burgasser et al. (2004)	1800	5.5	-0.0	2.94
2MASS WJ1645221-131951	L1.5	-	Burgasser et al. (2008)	1900	5.5	-0.0	1.95
2MASS LJ1807159+501531	L1.5	L1	Burgasser et al. (2008)	1900	5.5	-0.0	2.28

Table 6.1: List (1/2) of observations for which we have obtained atmosphere parameters through fitting.

*The data by Muench et al. (2007) lacks error information which results in equal weighting of the data points and systematically lower goodness-of-fit.

object designation	observation			DRIFT-PHOENIX best fit			
	optical SpT	NIR SpT	observation by	$T_{\text{eff}}[K]$	$\log(g)$	$[M/H]$	goodness-of-fit
2MASS J1807159+501531	L1.5	L1	Burgasser et al. (2008)	1800	5.5	-0.0	2.95
Kelu-1	L2	-	Burgasser (2007)	1800	5.0	-0.0	1.63
SSSPM0829-1309	L2	-	Burgasser (2007)	1800	5.5	-0.0	3.39
2MASS J0847287-153237	L2	L2	McElwain & Burgasser (2006)	1800	5.5	-0.0	1.01
2MASS J0117474-340325	-	L2	Burgasser et al. (2008)	1800	4.5	-0.0	0.90
2MASS J1431+1436	L2	L2	Sheppard & Cushing (2009)	2100	5.5	-0.0	3.05
2MASS J09211410-2104446	L2	L4	Burgasser et al. (2007)	2000	5.0	+0.3	2.12
2MASS J0241536-124106	-	L2	Burgasser et al. (2008)	1800	5.0	-0.0	1.65
2MASS J12070374-3151298	L3	-	Siegler et al. (2007)	1700	5.0	-0.0	0.75
2MASS WJ1506544+132106	L3	-	Burgasser (2007)	1700	4.0	-0.0	0.85
2MASS J17072343-0558249B	-	L3	McElwain & Burgasser (2006)	1800	5.5	-0.0	3.23
2MASS J21512543-2441000	L3	-	Burgasser et al. (2008)	1600	4.0	-0.0	1.00
SDSS pJ224953.45+004404.2	L3	L5	Burgasser et al. (2008)	1600	4.5	-0.0	0.90
SDSS J202820.32+005226.5	-	L3	Burgasser et al. (2008)	1800	5.5	-0.0	2.26
SDSS J232804.58-103845.7	-	L3.5	Chiu et al. (2006)	1800	4.5	+0.3	2.25
SDSS J121659.17+300306.3	-	L3.5	Chiu et al. (2006)	1800	5.0	+0.3	0.63
2MASS J17111353+2326333	-	L3.5	Chiu et al. (2006)	1800	5.5	-0.0	1.71
2MASS J11000965+4957470	L3.5	-	Siegler et al. (2007)	1700	5.0	-0.0	0.58
SDSS J134525.57+521634.0	-	L3.5	Chiu et al. (2006)	1800	5.5	-0.0	0.62
2MASS WJ0036159+182110	L3.5	L4	Burgasser et al. (2008)	1800	5.0	-0.0	2.98
SDSS J024256.98+212319.6	-	L4	Chiu et al. (2006)	1800	5.0	-0.0	0.82
SDSS J153453.33+121949.2	-	L4	Chiu et al. (2006)	1700	4.5	-0.0	0.90
SDSS J161731.65+401859.7	-	L4	Chiu et al. (2006)	1600	5.5	+0.3	1.52
SDSS J173101.41+531047.9	-	L4	Chiu et al. (2006)	1700	4.5	-0.0	1.17
2MASS J1104012+195921	-	L4	Burgasser et al. (2004)	1800	5.0	-0.3	1.51
2MASS J15200224-4422419B	-	L4.5	Burgasser (2007)	1900	5.5	-0.0	2.63
SDSS J083506.16+195304.4	-	L4.5	Chiu et al. (2006)	1700	5.0	-0.0	1.75
SDSS J085116.20+181730.0	-	L4.5	Chiu et al. (2006)	1700	5.5	-0.0	0.95
SDSS J213240.36+102949.4	-	L4.5	Chiu et al. (2006)	1800	4.5	+0.3	1.47
GJ1001B	L5	L4.5	Burgasser (2007)	1700	4.0	-0.0	3.70
2MASS J01443536-0716142	L5	-	Burgasser et al. (2008)	1600	4.0	-0.0	2.10
SDSS J162255.27+115924.1	-	L5	Chiu et al. (2006)	1800	5.0	-0.0	0.51
SDSS J154849.02+172235.4	-	L5	Chiu et al. (2006)	1800	5.0	-0.0	0.35
SDSS J164916.89+464340.0	-	L5	Chiu et al. (2006)	1800	5.0	-0.0	1.02
SDSS J213352.72+101841.0	-	L5	Chiu et al. (2006)	1800	5.0	+0.3	1.14
2MASS WJ1507476-162738	L5	L5.5	Burgasser (2007)	1800	5.0	-0.0	0.81
SDSS J020608.97+223559.2	-	L5.5	Chiu et al. (2006)	1800	5.0	-0.0	1.87
SDSS J134203.11+134022.2	-	L5.5	Chiu et al. (2006)	1700	5.0	-0.0	1.15
2MASS J20025073-0521524	L6	-	Burgasser et al. (2008)	1600	4.0	-0.0	0.97
2MASS J0103320+193536	L6	-	Cruz et al. (2004)	1600	3.5	-0.0	0.48
2MASS J0439010-235308	L6	-	Burgasser (2007)	1800	5.0	+0.3	1.18
SDSS J000250.98+245413.8	-	L6	Chiu et al. (2006)	1700	5.0	-0.0	1.66
SDSS J065405.63+652805.4	-	L6	Chiu et al. (2006)	1800	5.5	+0.3	2.33
SDSS J103321.92+400549.5	-	L6	Chiu et al. (2006)	1800	5.0	-0.0	0.83
SDSS J163359.23-064056.5	-	L6	Chiu et al. (2006)	1800	4.5	-0.0	3.64
2MASS J1010148-040649	L6	-	Reid et al. (2006)	1700	4.5	-0.0	1.04
2MASS J21481628+4003593	L6	L6.5	Looper et al. (2008)	1500	3.0	-0.3	5.01
2MASS J2244316+204343	L6.5	L7.5	Looper et al. (2008)	1500	3.5	+0.3	1.57

Table 6.2: List (2/2) of observations for which we have obtained atmosphere parameters through fitting.

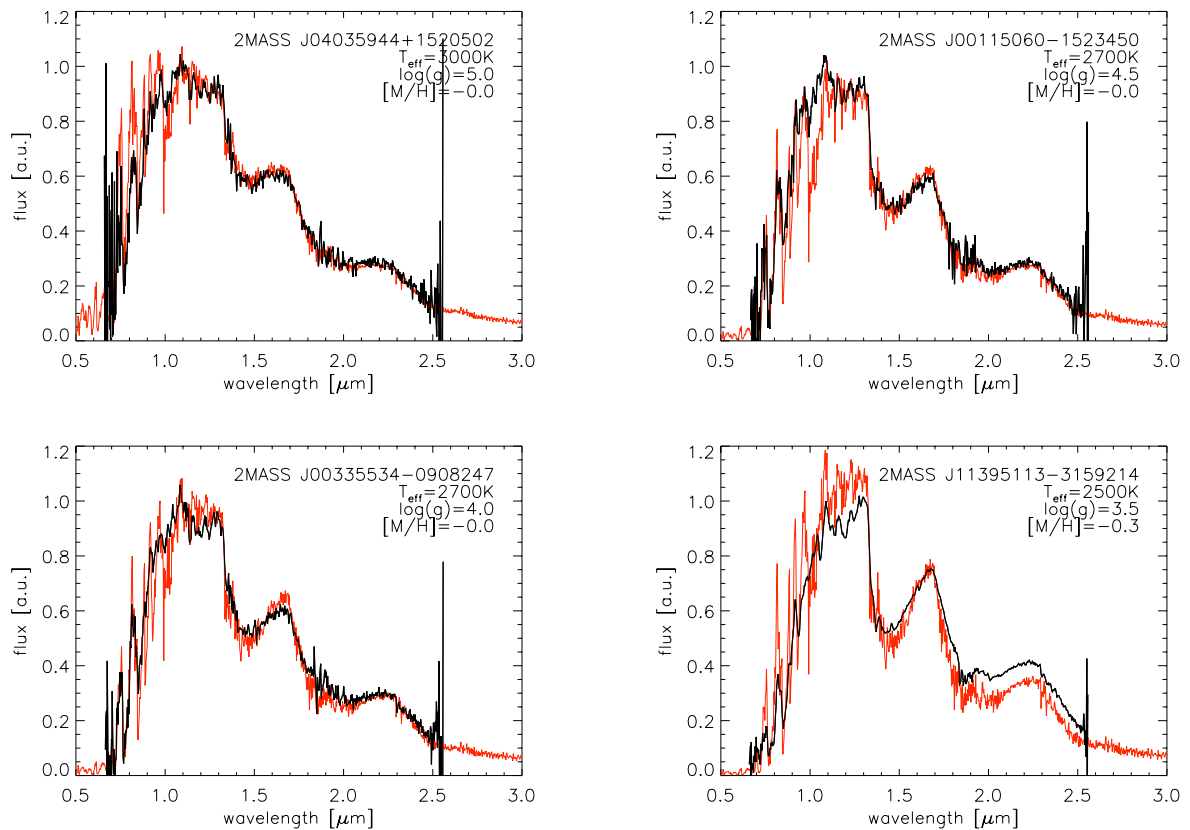


Figure 6.1: Comparison between models and observations (1/4): observation (*black*), best fitting model (*red*); spectral types: *top-left*: M7, *top-right*: M7.5, *bottom-left*: M8, *bottom-right*: M9.

For the slightly later spectral type M9, the atmospheric amount of dust has already increased considerably. The model atmospheres show signs of strong backwarming which feeds back on the spectra. The uncertainties of the atmosphere models increase considerably, which is mostly a result of the complexity of the dust cloud and its growing influence on the spectrum for decreasing effective temperatures. Therefore, observations of spectral type M9 objects are less well reproduced than the hotter atmospheres. Regardless, the example of J11395113-3159214 (Fig. 6.1, bottom-right) demonstrates that the overall shape of the best fitting synthetic spectrum agrees well with the observations. Especially with respect to the strength of the H₂O and CO bands as well as the shape of the H and K band. A slightly overestimated J band flux combined with a too low K band flux of the best fitting model suggest a slightly overrated effective temperature, which appears to become a systematic problem of the fits at spectral type M9.

The gravity distinction has become more reliable for such later spectral types because of the growing amount of dust for decreasing effective temperatures combined with the sensitivity of the grain composition with respect to the gravity. Therefore, our fits suggests a young age for J11395113-3159214 which corresponds to the conclusion of Looper et al. (2007). Rice et al.

(2009) have recently published narrow band fits for JJ11395113-3159214, using DUSTY-PHOENIX spectra. They have found a surface gravity comparable to ours. Both effective temperature estimates are in good agreement, differing by only about 100K. This small difference is not surprising because the cloud has not yet become optically thick for the given effective temperatures. Therefore, the spectra are affected the most by the bottom by the cloud, where the DRIFT-PHOENIX model clouds are very close to phase-equilibrium. With growing optical thickness and growing backwarming for decreasing effective temperatures, higher altitude layers begin to dominate the spectral influence of the cloud. This emphasizes the differences between the two model setups, because only the DRIFT-PHOENIX models considered the non-equilibrium element consumption and gravitational settling effects that are important in these cloud layers.

M-L transition objects: Representative fits for the transition between the M and L spectral types are shown in Fig. 6.2.

Over the range M9...L1, the fits reveal a broad gap with respect to the effective temperature (Tab. 6.1). Instead of a continuous distribution of the effective temperatures, the preferential values of the fitting for these spectral types are $T_{\text{eff}}=2500\text{K}$ and 2000K for high gravity objects.

For the brown dwarf LP994-20 (M9; Fig. 6.2, top-left), the best fitting model suggests an effective temperature of 2000K , which agrees with results of Ribas (2003) within the systematic errors. However, like for many objects around the M-L transition, the best fit overestimates the H band flux and overrates the water bands. Compared to objects of the same spectral type like the previously discussed JJ11395113-3159214, the inferred effective temperatures are systematically too low. This problem has its origin in two aspects of the spectra. The one is the reddening of the spectra for decreasing effective temperatures while the other is the increasing strength of the prominent water bands. Apparently, the reddening of the synthetic spectra with the effective temperature proceeds too slow, which is likely a result of a too weak increase of the dust opacity. This brings about a bias of the goodness-of-fit towards cooler model spectra. At the same time, the lower dust opacity means a greater strength of molecular bands such as H_2O and CO because a deeper view into the atmosphere is possible. The unrealistic strength of these bands creates a fitting bias towards hotter model spectra. Both biases artificially depopulate the range between $T_{\text{eff}}=2500\text{K}$ and 2000K . Such an effect is most significant for the employed wide-band fitting method because it relies heavily on the spectral energy distribution as well as strong features such as the water bands.

The objects J04574903+3015195 (M9.25; Fig. 6.2, top-right) and J01415823-4633574 (L0; Fig. 6.2, bottom-left) have both been characterized as a young dwarfs (Kraus & Hillenbrand, 2009; Kirkpatrick et al., 2006, resp.). The goodness-of-fit across the model grid unambiguously reinforces these conclusions. In other words, the distinction between different surface gravities has become more reliable because the sensitivity of the cloud to this parameter is better visible in the spectrum of the concerned spectral types. In both cases, the best fitting synthetic spectra match the observation very well including many smaller features. Regardless, the deviation between the best fitting effective temperatures of the two objects is 900K ,

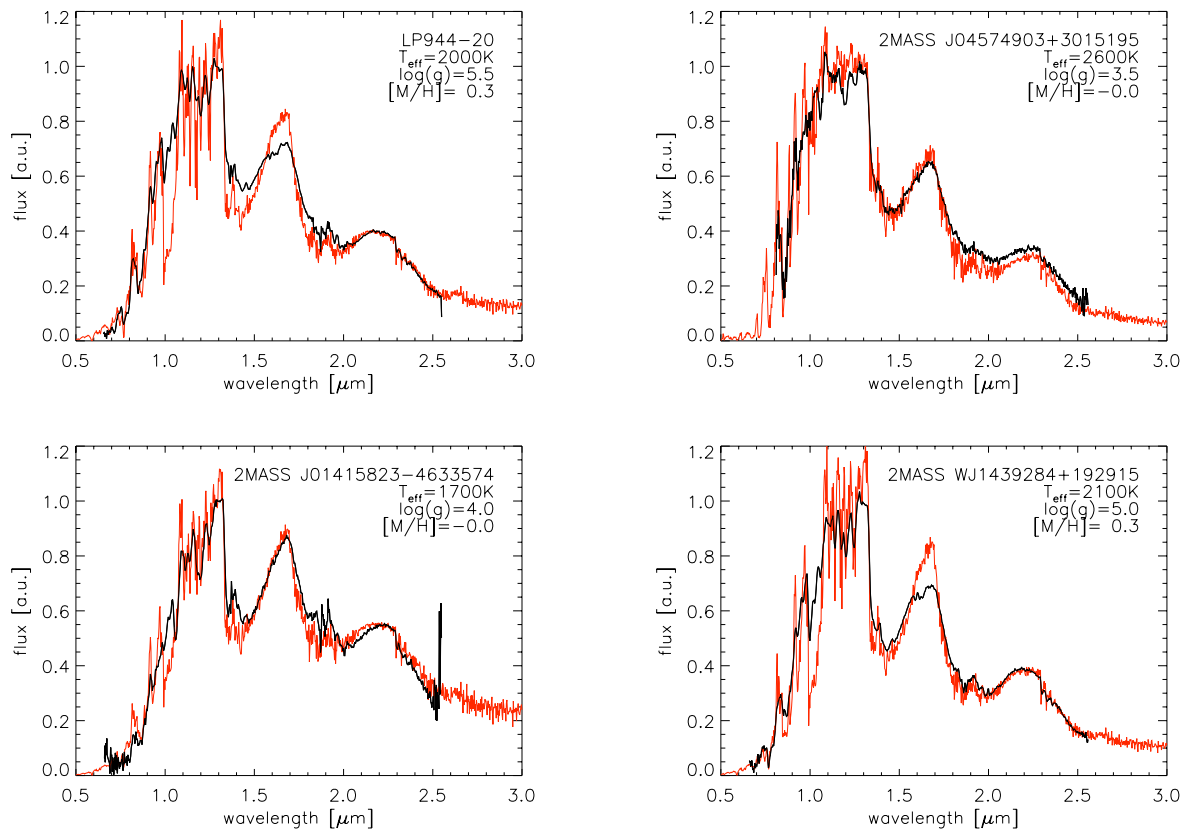


Figure 6.2: Comparison between models and observations (2/4): observation (*black*), best fitting model (*red*); spectral types: *top-left*: M9, *top-right*: M9.25, *bottom-left*: L0, *bottom-right*: L1.

with is considerably too high considering the difference in the spectral classification by less than one sub-type. Hence, while the false effective temperature gap of the fitting process is already huge for higher gravity models, it is twice as wide for the lower gravity models. This implies that the reddening of the models with decreasing effective temperature is even less well reproduced for the lower gravity models. The reason for this is the weaker iron contribution to the dust volume in the lower gravity atmospheres (discussed in Sec. 5.5) that is responsible for much of the opacity in the optical and the blue part of the near-infrared.

There are a number of possible explanations for the deficiencies of the current models at the M-L transition. Particularly the element replenishment produces immense uncertainties with respect to the amount of dust within the atmosphere, because this convection-driven mechanism has not yet been understood well. Another option is a too low number of chemical reaction paths and possibly too low numbers of solid species which would increase the amount of dust and, thereby, raise the opacity. A variation of this would be an insufficient number of nucleation species which would increase the opacity by a larger number of dust particles. Alternatively, the assumed sphericity of the dust particles does not only minimize growth rates due to the small surface area but also reduces the frictional force that the grains

experience. In other words, the model dust particles are smaller and falling faster than in a realistic environment. Again, this limits the dust opacity. Upcoming model generations will need to identify which of these points is causing the most significant errors in order to reproduce the M-L transition better than the current one.

Competing atmosphere models face similar issues. For example, Saumon & Marley (2008, Fig. 10) shows that even the parameterized variation of the grain precipitation in their models via free parameters is unable to reproduce the colors of observations near the M-L transition. The exact conditions of the cloud are not yet satisfyingly emulated by any existing model over this spectral type range.

Early L dwarfs: Following the transition into the regime of L dwarfs, the dust cloud is strongly limiting its own expansion by heating the atmosphere. Section 5.4.4 discussed how the backwarming causes a comparably flat curve of the amount of dust over the effective temperature around $T_{\text{eff}}=2000\text{K}$. Because of this limiting effect, the previously too low dust opacity can catch up on real world dust clouds of early L dwarfs. Accordingly, the goodness-of-fit improves considerably for this range of spectral types, as showcased by Fig. 6.3. The earliest L types might still be affected from the effective temperature gap around the M-L transition. Therefore, the effective temperature of objects such as J2057540-025230 (Fig. 6.3, top-left) tends to be underestimated by the fitting method and the model grid. A systematic problem of the models corresponding to the earliest L dwarfs is the overemphasized FeH band at $\sim 1.0\mu\text{m}$. This might be an indicator for the necessity of additional reaction paths for the condensation that involve iron but might as well have other origins. Aside from the too strong FeH band, the early L dwarf fits are remarkably good. In contrast to the limiting case DUSTY-PHOENIX models, the flux in the JHK bands and the molecular band strength is matched for one and the same stellar parameter set.

Mid-L dwarfs: The fits for intermediate L dwarfs reveal the other big problem of the current model generation. In real world objects, the dust opacity drops suddenly around type L6. With the dust cloud all but gone, the radiation of hotter layers from further inside the atmosphere become directly visible again, which turns the spectra considerably bluer. Lacking the understanding of the process that destroys the dust cloud, the model is unable to account for it. The sudden destruction of dust cloud is heralded by a weak but nonetheless perceptible decrease of the dust opacity over a range of several subtypes. The synthetic spectra are considerably redder than they should be for the given effective temperatures. Thus, the fitting process is biased towards higher effective temperatures which causes discrepancies in the fits that raise the goodness-of-fit of the best fits for later spectral types than L3. An example of this is J1507476-162738 (L5; Fig. 6.4, top-left), which has a higher best fitting effective temperature but a notably later spectral type than J1506544+132106 (L3; Fig. 6.3, top-left). For even later type samples, e.g., J1010148-040649 (L6; Fig. 6.4, top-right), the models can hardly match the contour of the near-infrared spectrum. A lower surface gravity brings about a lower iron contribution to the solid material within the model atmospheres. This results in slightly bluer synthetic spectra, which creates just another bias with respect to the fitting at the given effective temperature range. The destruction of the dust cloud

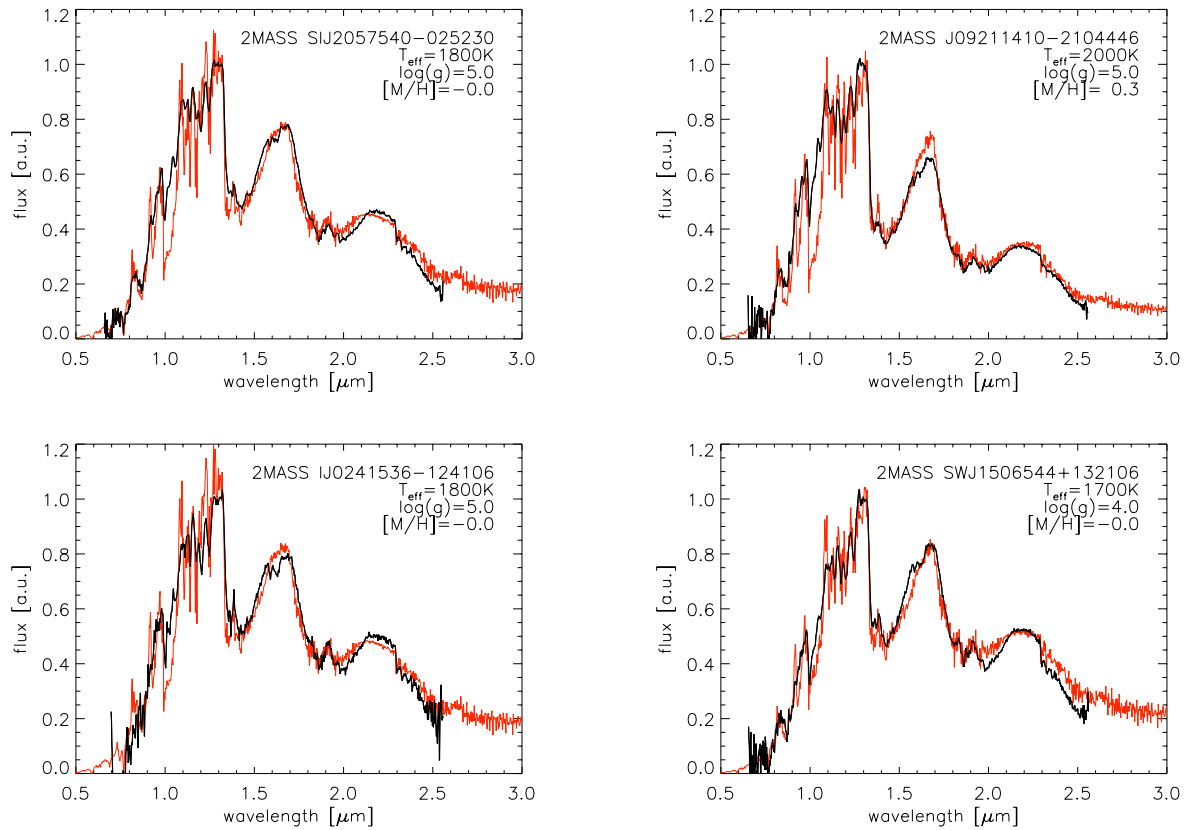
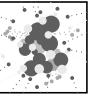


Figure 6.3: Comparison between models and observations (3/4): observation (*black*), best fitting model (*red*); spectral types: *top-left*: L1.5, *top-right*: L2, *bottom-left*: L2, *bottom-right*: L3.

following the spectral type L6 means that no ordinary object of later type can be reproduced properly with the current model generation.

At present, there are only few unusually red dwarfs that are exceptions to this rule. Two of those are J21481628+4003593 (L6.5; Fig. 6.4, bottom-left) and J2244316+204343 (L7.5; Fig. 6.4, bottom-right). Both display a considerably enhanced flux in the H and K bands at the expense of the J band. The best fits point to effective temperatures of 1500K, low surface gravities and near-solar abundances. Unfortunately, the previously noted fitting bias towards higher temperatures and lower gravities makes the best fitting stellar parameters for the two dwarfs rather disputable.

Looper et al. (2008), have studied both objects and argued that either a low surface gravity or a higher metal abundance is responsible for the unusually red spectra. The measurement of a high tangential velocity of J21481628+4003593 led them to conclude a high age, which speaks against a low surface gravity scenario. Conflicting with this are the weak KI lines and lacking FeH absorption in the spectrum of J2244316+204343, which McLean et al. (2003) have interpreted as indication for a low gravity. Therefore, conventional means can neither confirm nor rule out the best fitting parameters of the current DRIFT-PHOENIX model grid.

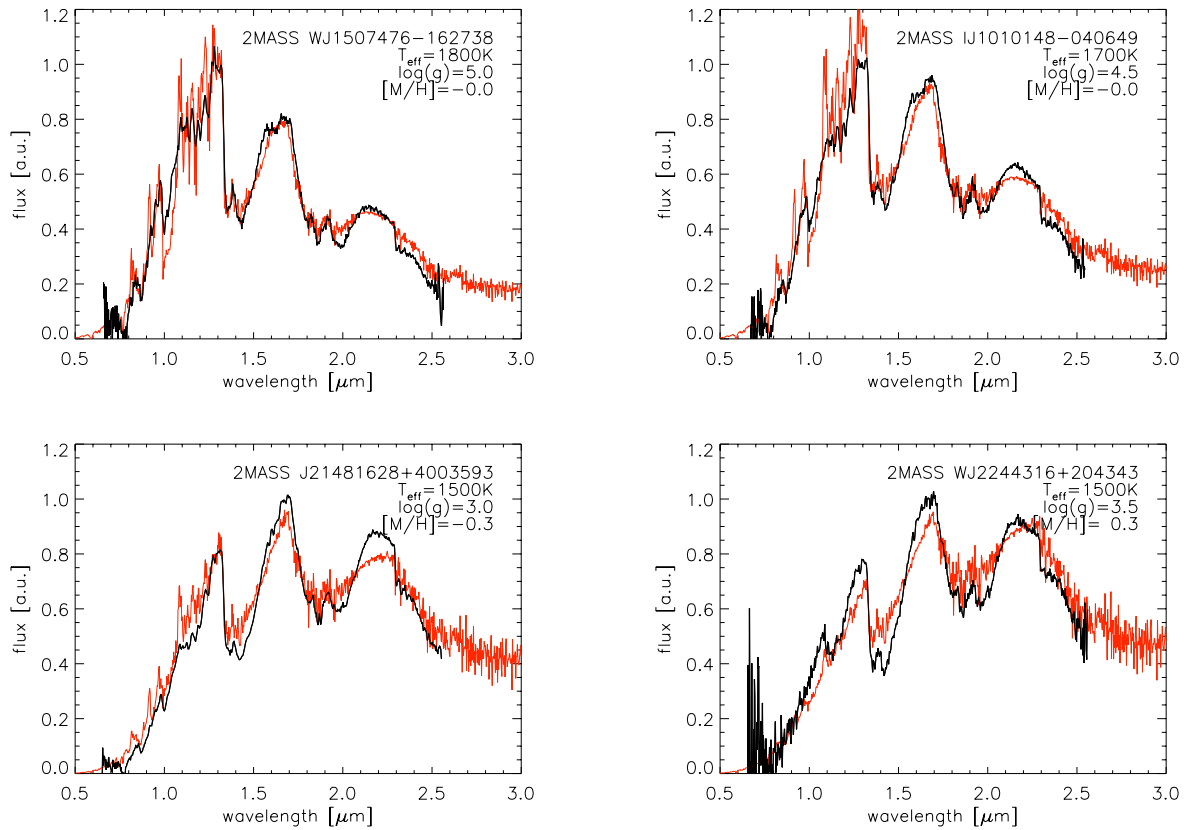


Figure 6.4: Comparison between models and observations (4/4): observation (*black*), best fitting model (*red*); spectral types: *top-left*: L5, *top-right*: L6, *bottom-left*: L6.5, *bottom-right*: L7.5

Relying on Saumon & Marley (2008) atmosphere models which feature a parameterized amount of dust within the atmosphere, Stephens et al. (2009) have obtained best fit parameters of $T_{\text{eff}}=1100\text{K}$ and $\log(g)=5.0$ for J2244316+204343. Together with an unusually large amount of dust within the atmosphere, their presumed high gravity meets expectations by Looper et al. (2008). Considering the best fitting effective temperature of Stephens et al. (2009), figures 8 and 14 of Saumon & Marley (2008) imply that the J-K index of J2244316+204343 would have to differ from typical dwarfs of similar brightness by an immense value of 2.0. Assuming a slightly higher effective temperature by about 200K, the deviation of the J-K from typical values would decrease to 0.4, which is much more plausible. Hence, fits with current Saumon & Marley (2008) models appear to underestimate the effective temperature of the unusually red dwarfs, while the DRIFT-PHOENIX overestimate it. The real effective temperature is likely in between both modelling approaches.

Currently, the characteristics of late L dwarfs and the L-T transition can not be explained by either observational means or reproduced by any atmosphere simulation without resorting to free parameters.

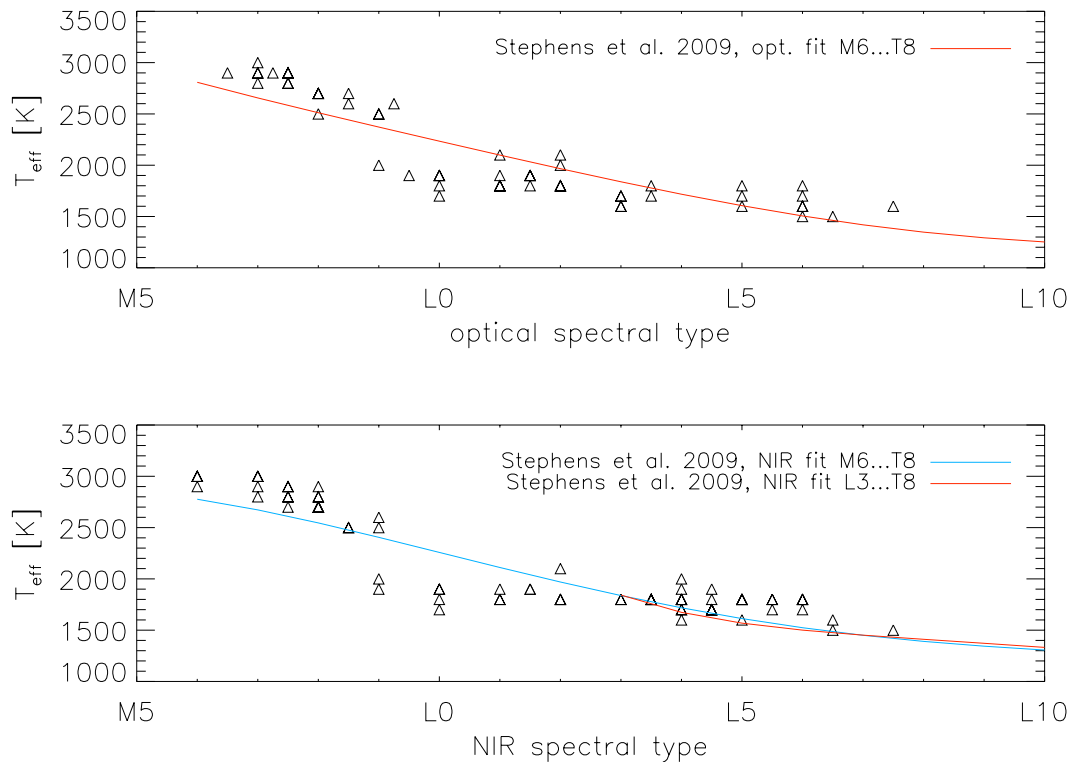


Figure 6.5: Effective temperature-spectral type sequence.

Complete sequence: Following the detailed discussion of more narrow ranges of spectral types it is possible to have a broader view. Figure 6.5 shows the best fitting effective temperatures of all 108 observations as functions of their optical and near-infrared spectral types. In addition, the figure shows polynomial fits for empirically derived effective temperatures by Stephens et al. (2009), which is an improved version of results by Golimowski et al. (2004).

As demonstrated by Fig. 6.1...6.4, the models are able to obtain reasonable fits for most of the given near-infrared data. In general, the agreement between model-derived effective temperatures and empirical values for constant spectral type is quite good. Especially since the models do not rely on the variation of free parameters for tuning the amount of dust. Of course the previously mentioned key problems of the fitting process and the models, i.e., the effective temperature gap at the M-L transition and the mid-L types, are well discernible in the effective temperature-spectral type relation. The former covers the spectral types M9 to about L1 and is caused by too blue model spectra due to a too low dust opacity while the latter appears for spectral type L4 and is caused by exceedingly red spectra due to overestimated dust opacities. Both of these ranges yield significantly higher goodness-of-fit values because of biases to either too high or too low effective temperatures. In addition, there appears to be a systematic disagreement between the model fits and the Stephens et al. (2009) polynomials for the mid-M dwarfs. It is most likely due to the comparably low number of data points that contributed to the polynomial fitting at this range.

While results at the M-L transition are not fully satisfying, the much more severe problem is the effective temperature range of the model grid below 1600K. These models are becoming redder at an enormous pace which contradicts all observational evidence. As a result, the goodness-of-fit for $T_{\text{eff}} \leq 1500\text{K}$ rises so strongly that, ignoring unusually red objects, no fitting process will converge to these models. Therefore, it is not possible to study the transition between the L and T spectral types with the given model grid.

Saumon & Marley (2008) have constructed a sequence of their atmosphere models wherein the amount of dust has been calibrated on observational data. Because of the parameterized nature of the dust in their models the fits can adapt more easily to the rapid changes in observed spectra. In this model sequence, the amount of dust is undergoing a sharp drop for the mid-L types. A yet undetermined mechanism of real world dwarfs destroys the cloud beyond spectral type L5, which matches the symptoms of the fits with the DRIFT-PHOENIX models.

A comparably minor issue that affects the fitting process is an effect of degenerate spectral appearance. For the hottest part of the model grid, the surface gravity has a comparably low influence on the larger features of the spectrum. The goodness-of-fit is nearly identical for such models if the spectral resolution is low. Hence, it is often problematic to determine the correct value for surface gravity from low resolution observations of mid-M dwarfs. For later spectral types, this degeneracy disappears because of a gravity sensitivity of the dust opacity. Around spectral type L3, another degeneracy of the spectra has appeared. In the cool models below $T_{\text{eff}}=2000\text{K}$ the cloud is optically thick in the near-infrared, i.e., it blanks out the atmosphere below, including the gravity-sensitive cloud bottom. As mentioned above, the structure of the upper dust cloud is more or less independent from the stellar parameters. Furthermore, the upper atmosphere of these cool models develops only slowly with the stellar parameters. Therefore, the spectra are mostly distinguished by the altitude of the dust cloud which determines how deep the atmosphere is directly accessible by observations. This altitude of the dust cloud is a function of the stellar parameters. For instance, a decrease of the effective temperature shifts the dust cloud inwards. However, this shift can be compensated by a slightly lower surface gravity. Such a simultaneous increase or decrease of both parameters yields comparable configurations of the dust cloud while the directly visible atmosphere has not changed considerably. Therefore, the spectrum will also not change considerably. An example of such ambiguous spectra is shown in Fig. 6.6. The implications for the low resolution fitting process of the degenerate spectra is a larger uncertainty of derived stellar parameters that is not caused by deficiencies of the models but by the nature of the concerned atmospheres.

6.3 Photometry

In order to study the synthetic spectra from a different perspective, near-infrared color indices have been calculated (Fig. 6.7).

The shown model sequence agrees roughly with the late M and the L dwarfs in the color-color diagram. For the late M dwarfs, especially the H-K index of the models is reproducing the colors of observations. The flux in the J band is underestimated by the models for these

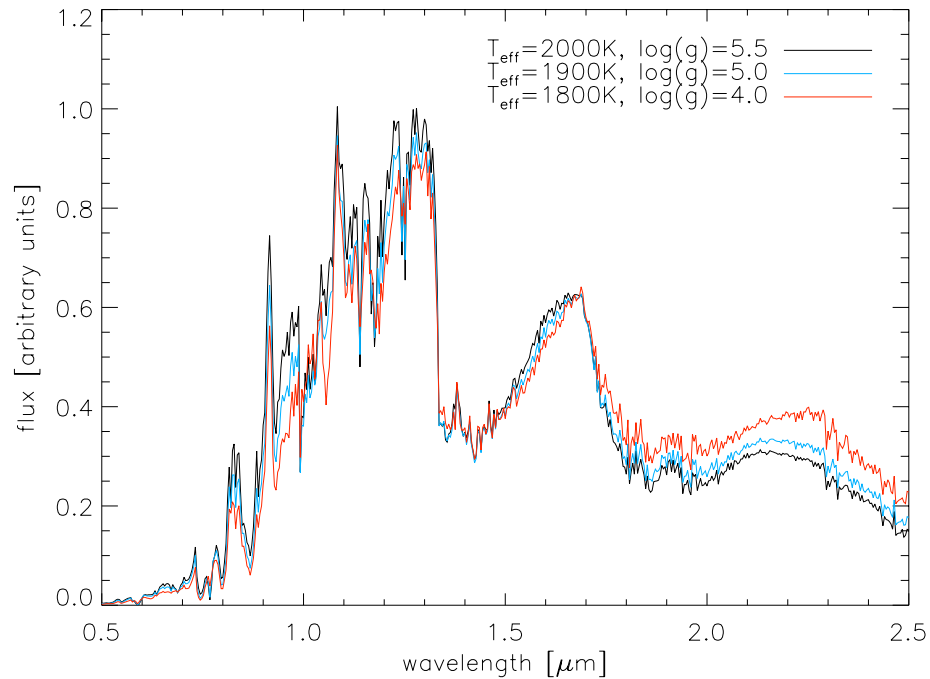
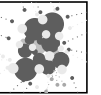


Figure 6.6: Spectral degeneracy effect shown on the example of three models for different stellar parameters. Most of the discernible differences are a result of the coarseness of the model grid.

objects. Because this mismatch decreases for lower surface gravity, there is a small bias towards best fits for intermediate gravity. Following the M-L transition the observed color indices and those of the models are in ideal agreement. For the early to mid-L types, the J-H of the models appears to be appropriate while the H-K point to too red spectra. This overestimation of the H-K index is stronger for the mid-L type models. In the color-color diagram the sudden absence of the dust cloud for the later L and T dwarfs is very well perceptible, because both color indices are shifted back to the blue very quickly. In contrast, the models do not take into account any mechanism that could be responsible for destroying the cloud. Therefore, the model curve continues into the red.

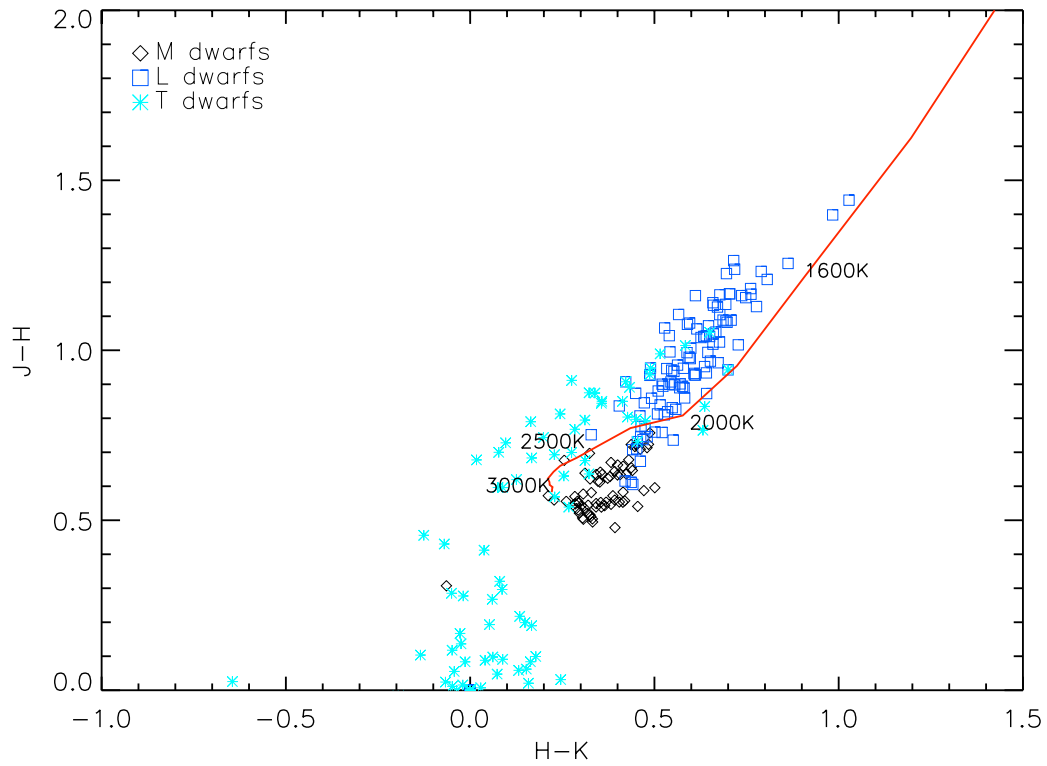
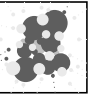


Figure 6.7: Near-infrared color-color plot showing observations between late-M and T spectral types and a model sequence ($\log(g)=5.0$, $[M/H]=0.0$).



7 Conclusions

In the previous sections, the model atmospheres have been discussed. The agreement of their spectra and colors with observations is in many cases excellent.

At this point, all conclusions that have been drawn from the current model grid are gathered, which allows to identify the key issues of the atmosphere and dust model that will have to be addressed in the future.

- The models are able to reproduce observations of spectral types earlier than L6 (Sec. 6.2). Unfortunately, the models for $T_{\text{eff}} \leq 1500\text{K}$ are not yet usable because they lack a mechanism clearing the atmosphere from condensed material as it seems to occur in real world objects of later type than L6.
→ This mechanism needs to be identified and implemented to expand the effective temperature range of the models.
- The best agreements between the models and observations are obtained for dust-poor late M-dwarfs and the early L dwarfs. In the former case it is obviously a result of the still low amount of dust in the atmosphere. Around the M-L transition, the model spectra appear to be too blue in the near-infrared, which is a symptom of an underestimated amount of dust. For the mid-L spectral types, the synthetic spectra are typically too red, which means the model feature too much dust. The switch from too rare dust for the late M dwarfs to too much dust for the mid-L dwarfs occurs in the range of early L spectral types. Therefore, the amount of dust within these model atmospheres seems to come fairly close to those of clouds of corresponding real objects.
→ The underestimation of dust opacity at the M-L transition requires further investigation (Sec. 6.2). On one hand, its reason might be a too conservative approximation of the element replenishment. On the other hand, the gravitational settling might be overestimated because the spherical and non-porous dust particles of the model yield the highest possible density and smallest possible cross section which minimizes the experienced frictional force.
- The formation of silicates and other high temperature condensates depletes many elements in the gas phase at the clouds of M and L dwarfs (Sec. 5.1). With the absence of heavier elements from the cloud layers of cooler atmospheres, the chemistry is very much reduced to the chemical nonmetals. This involves an increasing concentration of NH_3 and H_2S in favor of metal nitrides and metal sulfides, respectively. Condensates of these two gas species have been noted for their importance in the atmospheres of large Jovian planets (e.g., Delitsky & Baines, 2007). Therefore, the gas phase chemistry of the coolest models seems to approach a state that is comparable to observed planetary atmospheres.

- Currently, alkali and earth-alkaline elements such as Ca are not considered in the dust model (Sec. 5.1). Geological studies suggests their growing contribution to condensates for decreasing temperatures (e.g., Mueller & Saxena, 1977), which means they will have to be eventually considered. Their absence in the dust particles of the model underestimates the influence of the dust precipitation and distorts the dust opacity. Likewise, these elements are not depleted in the gas phase, which causes overly strong absorption features. In the comparably hot atmospheres of the current model grid, the relevance of such effects is likely not very large though it will become significant for cooler atmospheres.
 - Additional solid species need to be considered in order to model the dust opacity and the gas phase abundances properly. Prerequisites for this are the availability of laboratory data and a revision of the numerics, such as a switch to a time-dependent relaxation.
- Comparisons with observations have implied an overestimated concentration of water in the model atmospheres (Sec. 5.1). Liquid and solid water are not able to form in the temperature and pressure ranges exhibited by the current model atmospheres, which excludes a direct rain out. However, porous or hygroscopic dust grains might transport some of the water from the higher to the lower atmosphere.
 - Laboratory studies of the porosity and hygroscopy of dust grains are required before a workable model of this problem can be considered.
- Witte (2008) noted that the backwarming could play a role in destruction of the dust cloud in the late L dwarfs. This appeared reasonable since the cloud top sinks deeper into the atmosphere for decreasing effective temperatures while the cloud bottom could not follow this descent due to the backwarming below $T_{\text{eff}}=2000\text{K}$. Only with the new model grid, it was possible to notice that this behaviour changed for $T_{\text{eff}} \leq 1500\text{K}$ (Sec. 5.2). For these models, the withdrawal of the convection zone accelerates, which allows the whole cloud to sink deeper into the atmosphere, causing another strong increase of the amount of dust instead of the expected decrease.
- The cloud structure definition introduced by Witte (2008) still applies to the lower effective temperature range that is now accessible because of the new model grid (Sec. 5.4.1). The surface gravity has a huge influence on the geometrical extension of clouds, that ranges from few kilometers to several thousand kilometers (Sec. 5.4.2). The impact of backwarming is well discernible in the cloud extension, resulting in a decrease of the geometrical thickness below $T_{\text{eff}}=2000\text{K}$.
 - The wide clouds of the low gravity atmospheres suggest the adaption of the dust model for spherical geometry.
- Typical lifespans of dust particles vary over several orders of magnitude, starting from less than an hour for the hottest dust-bearing high gravity models and approaching a century for the coolest low gravity models (Sec. 5.4.3). The time the grains spend at a distinct layer of the atmosphere increases with atmospheric depth. This means,



especially the lowest cloud layers are susceptible to disruption by turbulent motions, which proceed on much shorter timescales than the grain precipitation.

→ It is necessary to study whether significant turbulent motions can occur at dust clouds and how strongly this would perturb them.

- A new set of dust moments (σ_j) was introduced in order to describe the amount of dust within vertical gas columns with respect to the particle number, cross section and volume (Sec. 5.4.4). This allows for a direct comparison of the dust clouds. In agreement with expectations, the amount of dust increases for decreasing effective temperatures. This increase is notably slower around $T_{\text{eff}}=2000\text{K}$, which is a result of the backwarming. For the coolest considered atmospheres, the amount of dust still increases, albeit observational evidence indicates a sudden absence of dust clouds.
→ As noted before, the mechanism responsible for the sudden destruction of the cloud needs to be identified and modeled.
- Considering that the geometrical extension of the dust clouds is about three orders of magnitude wider for the lower gravity models (Sec. 5.4.2) and, likewise, the typical lifetimes of dust particles are orders of magnitude larger for lower gravity models (Sec. 5.4.3), it is somewhat surprising that the amount of dust within vertical gas columns is only so weakly affected by the surface gravity. In particular in the models that show strong backwarming, the high and low gravity atmospheres feature almost identical amounts of dust. This balanced amount of dust as function of the surface gravity is an effect of the gas phase density at the dust cloud layers that raises the rate of condensation to about the same degree as it reduces the typical grain lifetime for an increase in $\log(g)$.
- Like the surface gravity, the metallicity has an influence on the amount of dust that seems to be counterintuitive. The amount of dust within atmospheres does not scale linearly with the metal abundances Sec. 5.6. Notably the dust particle column densities of the models show a strong nonlinearity over the metallicity. Extreme element abundance patterns such as observed by Frebel et al. (2008) have a comparably small influence on the dust cloud with respect to the cloud structure and amount of dust. However, the grain composition and also the spectrum are immensely affected.
- With respect to the composition of the dust cloud, $\text{Al}_2\text{O}_3[\text{s}]$ is by far the dominant species until the backwarming becomes strong enough ($T_{\text{eff}} \approx 2000\text{K}$) to vaporize the lower cloud layers entirely (Sec. 5.5). The silicates quickly become the preeminent species for the cooler atmospheres. With the larger amount of solid state iron in higher gravity atmospheres, there is a narrow effective temperature range for which $\text{Fe}[\text{s}]$ is the dominant species.

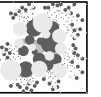
In addition to these points, there are several more improvements to the dust model which seem necessary. Most important is the determination of the grain size distribution f . Unfortunately, the current dust model provides a grain size distribution that appears rather

artificial, because the function is forced into a strict mathematical form. This creates uncertainties, especially with respect to the dust opacity, and strains the numerics of the model as it serves as closing condition for the system of equations. A more precisely determined grain size distribution provides other interesting opportunities for future consideration. The original dust moment approach of Gail & Sedlmayr (1988) considered coagulation and chemical sputtering of grains which, however, relies even stronger on a the grain size distribution. Therefore, this size distribution has to be determined rather precise. Coagulation and sputtering could become an interesting topic for future studies since they would accelerate the growth and evaporation rates. Unfortunately, the complexity of the mathematical formulation is becoming more and more daunting this way. Especially coagulation is able to produce strongly aspherical dust particles which can not be treated in the current model. Nonetheless, asphericity can have an immense influence on the growth/evaporation and also precipitation of dust by varying the surface area of the grains.

Another related issue is the porosity of dust grains that affects their density, hence the precipitation, their geometrical cross-section, thereby the growth/evaporation, precipitation, and the opacity, and their refractive index. In principle, vacuum could be considered in the dust model as an “additional solid species” without notable effort. However, this requires the understanding of how the vacuum as a species grows and evaporates.

Witte (2008) discussed that the flat mean grain size in the center of the dust clouds is caused by the dominance of newly forming particles in the affected layers. Due to this dominance, the rarer but larger particles effectively disappear from the grain size distribution of the model. In fact, the larger grain sizes are more and more populated for decreasing altitudes. However, the dust moments, hence, also the dependent grain size distribution, currently do not show this feature of the cloud. In order to study how such particles evolve, the formulation of the dust moments would have to be modified in order to track the grain size distribution more precisely.

Considering how badly convection is understood, let alone convective overshooting or other suspected element replenishment mechanisms, it is not surprising that comparisons between time-independent 1D simulations and observations of dust-rich atmospheres are still not completely satisfying. Albeit calibrated on solar observations, the mixing length parameter remains uncertain for the very low mass stars and the substellar range. Based on this vague description of convective processes, the DRIFT model approximates turn-over timescales in the radiative zones via a logarithmic dampening of convective timescales on the pressure scale. The overshooting parameter, responsible for the dampening, was calibrated on hydrodynamic simulations of late M dwarf atmospheres by Ludwig et al. (2002). Nonetheless, our understanding of the process remains sketchy. Simulations by Helling & Woitke (2004) and Freytag et al. (2010) resulted in opposing standpoints whether convective overshooting or gravity wave propagation are the dominant process with respect to the element replenishment above the convection zone. It is unlikely that observations will bring about a simple decision between these two rivaling theories, because the optically thick parts of the atmospheres and dust clouds possess comparable characteristics and hence will look very much alike. In the end, this is not even critical for the DRIFT model, since a gravity wave mixing would have to be abstracted in a similar fashion as the overshooting and end up with a simple dampening of the mixing timescales. Anyway, the problem of the unsatisfyingly understood



mixing remains and can only be resolved by hydrodynamical simulations involving dust.

8 Framework for future dust models

The biggest problems of the current dust model have been discussed in the previous section. The next step is to eliminate these issues or at least find workarounds. Before further inroads into the range of exoplanets can be made, the model requires a number of reconsiderations and improvements. Over the course of this section, the mathematical formulation of the problem is expanded for future implementation. The system of equations is expanded stepwise to improve the determination of the grain size distribution, involving a switch to a time-dependent relaxation of the solution, converted to spherical geometry and, finally, expanded for 3D applications.

8.1 Convective term

Motivation: The most important problem of the current model that needs to be addressed is the sudden drop of dust opacity in the atmospheres of real objects of later spectral type than L6.

Burgasser et al. (2002b) and Burrows et al. (2006) have discussed the influence of detached convection zones that might form within dust clouds. On one hand, the motion of the gas can accelerate the element replenishment of higher cloud layers. On the other hand, the grains will be dragged along by moving gas elements. Unfortunately, the current model grid does neither show convective motion within the cloud nor would such motion be considered by the dust model. A closer examination of the absence of detached convection zones revealed that the calculation of the radiative temperature gradient, which determines whether a layer of a model atmosphere is convective or not, did not take into account the opacity of gas molecules or the dust grains. Disregarding both is usually unproblematic because typical convection zones are too hot to feature large amounts of either one. In this case both have to be considered. The reason why detached convection zones can form is the backwarming that levels the temperature gradient of the atmosphere at the bottom of the dust clouds. After the calculation of the radiative temperature gradient was fixed, a new sequence of models was calculated. They begin to feature detached convection zones at the bottom of the clouds for $T_{\text{eff}} < 1700\text{K}$. The resulting gas velocities exceed the settling velocities of typical dust grains by several orders of magnitude. As a result, convection will destroy the cloud in the affected layers by driving about half of the local dust into the higher atmosphere while the remains are pushed into deeper layers which accelerates its eventual evaporation. Furthermore, the grains that have been pushed upwards are still growing. Therefore, these grains will settle comparably fast and return to the initial altitude rather quickly. Presuming that there is still convection at this layer, there is a 50-50 chance of pushing these grains into the evaporation layers below. This way, this layer becomes nearly dust-free very quickly.



Derivation: The influence of the convection on the rate equation of the dust (Eq. 3.26) for a plane-parallel geometry is approximated by an additional term. Considering the convective velocity v_{conv} as gas velocity in Eq. 3.17 allows to adapt Eq. 3.21 for the convective motion:

$$\begin{aligned} \left. \frac{\partial f(\vec{N}_s, \vec{r})}{\partial \vec{r}} \frac{d\vec{r}}{dt} \right|_{\text{conv}} &= \frac{\partial}{\partial z} \left(f(\vec{N}_s, \vec{r}) v_{\text{conv}}(\vec{r}) \right) \\ &= v_{\text{conv}}(\vec{r}) \frac{\partial f(\vec{N}_s, \vec{r})}{\partial z} + f(\vec{N}_s, \vec{r}) \frac{\partial v_{\text{conv}}(\vec{r})}{\partial z} \end{aligned} \quad (8.1)$$

The dust moment equations (Eq. 3.35) are changed to:

$$\begin{aligned} \frac{d}{dt} \rho L_j &= \underbrace{V^{j/3} J^*}_{\text{nucleation}} + \underbrace{\frac{j}{3} \chi_{\text{net}}(z) \rho L_{j-1}}_{\text{growth/evaporation}} \\ &+ \underbrace{\xi \frac{\partial}{\partial z} \left(\frac{\rho_d}{c_{\text{th}}} L_{j+1} \right)}_{\text{gravitational settling}} + \begin{cases} v_{\text{conv}} \frac{\partial \rho L_j}{\partial z} + \rho L_j \frac{\partial v_{\text{conv}}}{\partial z} & \text{convective} \\ -\frac{\rho L_j}{\tau_{\text{mix}}} & \text{not convective} \end{cases} \end{aligned} \quad (8.2)$$

Depending on the local stability against convection, the local gas motion is either treated as convective or driven by overshooting as described in Sec. 3.7.

Application to current models: Focusing on the downwards-directed convective motion, $v_{\text{convection}}$ is negative. At the bottom of the cloud, where the models of the current standard grid show convection, no new grains are formed and the growth process proceed on long timescales compared to the convection (Sec. 5.4.3), which implies $v_{\text{convection}}(\vec{r}) \frac{\partial f(\vec{N}_s, \vec{r})}{\partial z} \ll f(\vec{N}_s, \vec{r}) \frac{\partial v_{\text{convection}}(\vec{r})}{\partial z}$. This permits the simplification of Eq. 8.1:

$$\left. \frac{\partial f(\vec{N}_s, \vec{r})}{\partial \vec{r}} \frac{d\vec{r}}{dt} \right|_{\text{convection}} = f(\vec{N}_s, \vec{r}) \frac{\partial v_{\text{convection}}(\vec{r})}{\partial z} \quad (8.3)$$

This simplified term could be included into the current numerics without significant modifications. Generally, i.e., in (3+1)D models, it is more secure to consider the full term but for the preliminary studies the simplified term is acceptable.

After considering this term, the amount of dust in the resulting models begins to drop as expected (Fig. 8.1). The influence of the forming detached convection zones on the near infrared colors is demonstrated in Fig. 8.2 (dashed line). The sustained trend of reddening of the original model spectra is stopped with this new configuration.

While these preliminary models show an enormous improvement over the standard model grid, the problem is not yet outright solved. For $T_{\text{eff}} \leq 1400\text{K}$, there is no longer a convergence to a unique solution but strong numerical oscillations turn up. In one iteration, there is no detached convection zone, which results in a large amounts of dust. This causes a strong backwarming and a flat gradient of the temperature. Therefore, the criterion for convection is triggered in the next iteration, which destroys the bottom of the dust cloud and, hence,

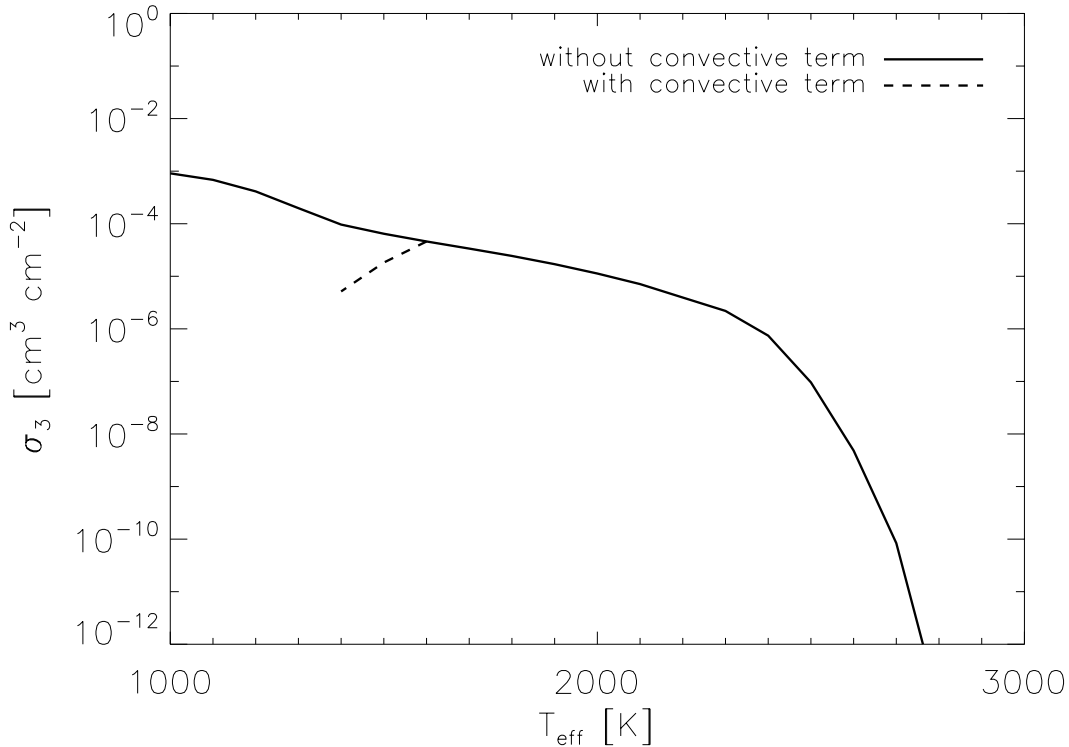


Figure 8.1: Column density of the dust volume as function of the effective temperature for $\log(g)=5.0$ and $[M/H]=0.0$. The solid curve corresponds to the models from the current standard model grid. The dashed lines correspond to models with the new convection term.

also its own cause. This cools the atmosphere considerably which allows a reformation of the dust cloud. Even strong dampening of the temperature correction is unable to stabilize the models, which is an indication for time-dependence.

The point is that the convective motion can wipe out the complete dust within the affected layers on the order of minutes. At the same time, the convection cools the local gas by transporting the deposited heat into other layers rather quickly. Considering that the descent of dust particles takes between weeks and decades (Sec. 5.4.3), it is evident that it will take at least as much time before a sufficient amount of dust has accumulated to restart the convection at these layers. In the mean time, the dust opacity will be considerably weaker than the standard grid of models suggests. Therefore, time-dependent modelling seems inevitable. Though increasing the calculational effort, a time-dependent solution brings about additional benefit in form of a relaxation of the numerics.

Of course, the variability of the atmosphere and cloud are hardly going to cause directly observable cycles on the order of weeks to decades. More likely, the variability is caused by local convective cells instead of a uniform convective layer of the atmosphere which means the various phases of the variability cycle are mapped statistically over the surface of the brown

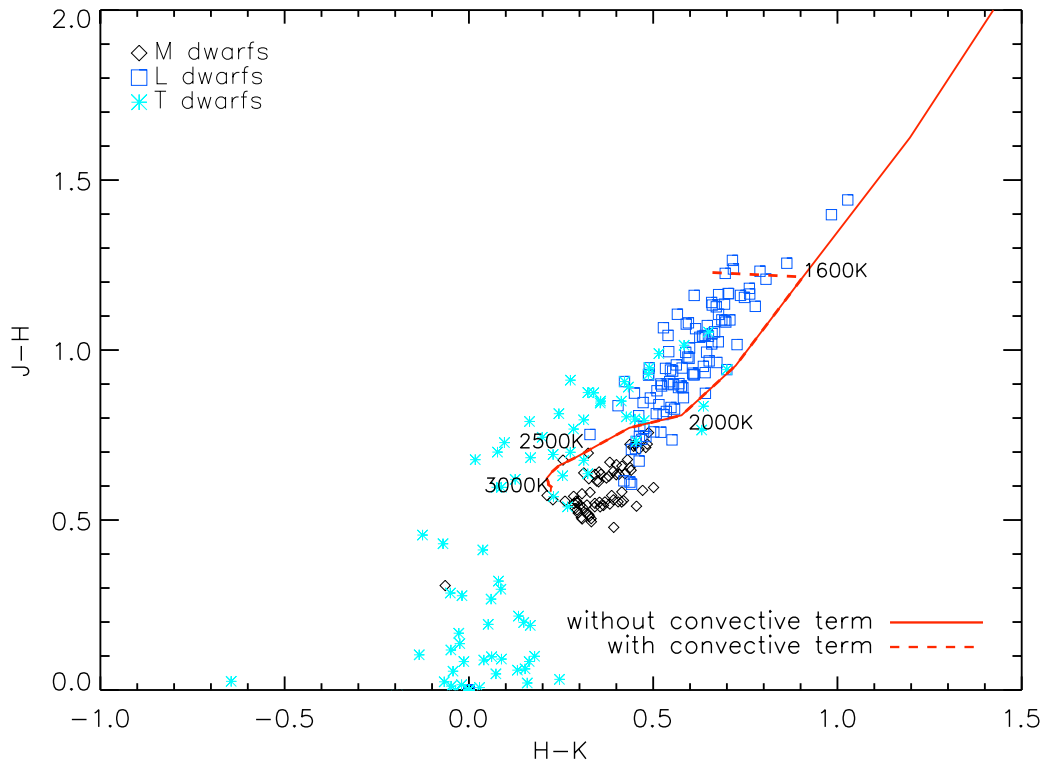
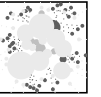


Figure 8.2: Near-infrared color-color plot showing observations between late-M and T spectral types and a model sequence ($\log(g)=5.0$, $[M/H]=0.0$). The dashed turn-off from the standard model sequence is achieved through consideration of convective overshooting (see Sec. 8.1).

dwarf or hot exoplanet. Hence, global variations are statistically washed out by the various local phases. Therefore, the spectrum will remain nearly static. In agreement with this conclusion, observations by Goldman et al. (2008) suggest that objects of the corresponding spectral types do not show notable variations with time. Nonetheless, variations with respect to the statistical mapping of variability phases create a multitude of different spectra for identical stellar parameters. This sheds a new light on the extraordinary blue and red L dwarfs that have been observed. The above or below average dust cloud coverage of objects such as J2244316+204343 (Looper et al., 2008) might be explained by simple chaotic mapping of variability phases that corresponds to additional degrees of freedom of the atmosphere aside from the usual stellar parameters. Previous attempts to explain such unusual blue and red L dwarfs relegated to extreme surface gravities or metallicities. However, this presumes that there are unambiguous indicators for such extreme parameters, which is hardly given if the cloud can undergo statistical variations on such a scale.

The conclusions of this section have recently been published by Witte et al. (2011). Nonetheless, it is noted that all of them have a preliminary status and have to be confirmed by a more thorough investigation.

Conclusion: The appearance of detached convection zones inside dust cloud seems to result in time-dependence of the atmosphere and cloud properties. There are indications that the spectrum of a corresponding object is going to be a superposition of various variability phases. Considering that the variety of the variability is likely going to result in lateral interaction, it appears essential to develop a time-dependent 3D dust model that can be tied into a (3+1)D atmosphere code.

8.2 Improved plane-parallel 1D model

Motivation: One of the biggest problems of the dust model is its grain size distribution. The respective information is effectively lost after the introduction of the dust moments. With an arbitrarily defined function, such as a double-delta peak or power law, the grain size distribution can be approximated from the dust moments (e.g., Helling et al., 2008c). However, this artificial distribution is not necessarily resembling the real distribution because its shape is pre-defined.

While not an unambiguous result of the model, the grain size distribution is a critical quantity for the numerics. First of all, it serves as closing condition for the system of dust moment equations. It is simple to imagine the strain to the numerics, considering that this condition is possibly badly approximated by an arbitrarily chosen function. On the other hand, a badly known grain size distribution creates enormous uncertainties with respect to the dust opacity, which might create additional strain.

In this section, a modified set of rate equations is derived in an attempt to relieve the numerics of some strain caused by the uncertainties in the grain size distribution. For clarity, this section focuses on plane-parallel 1D models.

Expanded system of dust moments equation: The dust moments of the current dust model are defined in Eq. 3.27. With their help, a new set of dust moments $L_{j,i}$ can be introduced. In order to relax the stiff system of rate equations, the original dust moments are separated into intervals $i \in \mathbb{N}$ in the grain volume space (Fig. 8.3). The lower and upper boundaries of the intervals are denoted by $V_{l,i}$ and $V_{u,i}$, respectively, resulting in the precise

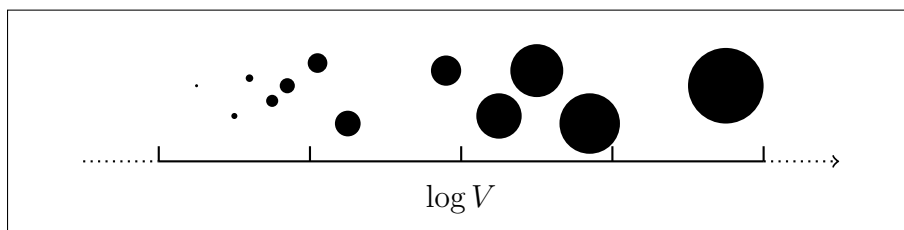
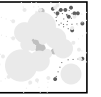


Figure 8.3: The dust moments of the current model refer to the full range of dust volume. This forfeits much information on the grain size distribution. The new model separates the dust moments into grain volume bins. The benefit is a more detailed impression of the grain size distribution.



interval definition $]V_{l,i}, V_{u,i}]$. The constraints $V_{l,0} = V_l$ (cf. Eq. 3.27) and $V_{u,i-1} = V_{l,i}$ and $V_{u,i} = V_{l,i+1}$ ensure that the full volume space remains covered. Exact boundaries between the volume intervals can be chosen arbitrarily, though a logarithmic spacing appears favorable.

With this, it is possible to define the new dust moments:

$$L_j(\vec{r}) = \sum_i L_{j,i}(\vec{r}) = \sum_i \int_{V_{l,i}}^{V_{u,i}} f(V, \vec{r}) V^{j/3} dV \quad (8.4)$$

Like the original dust moments, the new ones refer to the total local particle number, radius, surface area, volume, etc., though not for all dust grains but only those within the grain volume interval i . Similarly, the nature of the problem still adheres to the fundamental rate equation (Eq. 3.26). To keep the focus on the new dust moments, the same steps are taken to transform this equation into moment rate equations for plane-parallel 1D atmospheres. At this point, the only differences to the original derivation are the limits of the integral, which are not substituted by V_l and ∞ but by $V_{l,i}$ and $V_{u,i}$. The resulting set of equations is:

$$\begin{aligned} \frac{d}{dt} \rho L_{j,i} = & \underbrace{V_{l,i}^{j/3} J(V_{l,i}) - V_{u,i}^{j/3} J(V_{u,i})}_{\text{exchange with lower/higher volume intervals}} + \underbrace{\frac{j}{3} \chi_{\text{net}} \rho L_{j-1,i}}_{\text{growth/evaporation}} \\ & + \underbrace{\xi \frac{\partial}{\partial z} \left(\frac{\rho_{d,i}}{c_{th}} L_{j+1,i} \right)}_{\text{gravitational settling}} + \begin{cases} \frac{\partial}{\partial z} (\rho L_j \cdot v_{\text{conv}}) & \text{convective} \\ -\frac{\rho L_{j,i}}{\tau_{\text{mix}}} & \text{not convective} \end{cases} \end{aligned} \quad (8.5)$$

Note that the new dust particle density $\rho_{d,i}$ is a function of the volume interval i . There are two additional exchange rates per equation. Only the lowest considered volume interval $i = 0$ depends on the nucleation rate in its exchange rate term $J(V_{l,0})$. Respective exchange terms are derived in the following paragraphs.

The equations are left in their non-stationary form, which allows their solution via time-dependent relaxation. This way, the calculation of the dust cloud does no longer rely on a successive solution of the atmosphere layers from top to bottom. Instead, the computation of the cloud of all layers can be performed in a parallel mode once per time-step.

Alternative closure condition: When calculating dust moments for consecutive volume intervals, it is necessary to introduce a suited closure condition for the set of equations.

The original double delta-peaked closure condition for the set of moment equations does not provide reliable particle numbers at the interfaces between the volume intervals. However, these quantities are required for the calculation of the exchange rates $J_{l,i}$ and $J_{u,i}$.

The number of dust moment equations per volume interval permits a four parameters function for the definition of the grain size distribution within the interval i . Hence, the grain volume interval i can be separated further into 4 sub-bins $k \in 1, 2, 3, 4$ (Fig. 8.4), defined by $]V_{i,0}, V_{i,1}]$, $]V_{i,1}, V_{i,2}]$, $]V_{i,2}, V_{i,3}]$ and $]V_{i,3}, V_{i,4}]$ where $V_{l,i} = V_{i,0} < V_{i,1} < V_{i,2} < V_{i,3} < V_{u,i} = V_{i,4}$. The exact interval boundaries can be selected arbitrarily though, again,

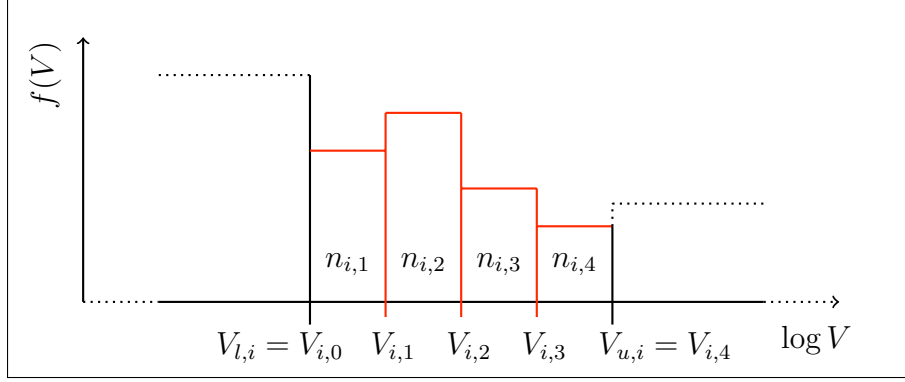


Figure 8.4: The new closure condition for the system of moment equations determines the number of grains $n_{i,k}$ within four sub-bins of the considered volume interval i .

an equidistant logarithmic subdivision of the interval appears opportune. Each bin k governs an individual number of dust grains $n_{i,k}$. This is sufficient to define a grain size distribution $f_i(V)$ for the interval i in form of a step-function

$$f_i(V) = \begin{cases} \frac{n_{i,1}}{V_{i,1}-V_{i,0}} & V \in]V_{i,0}, V_{i,1}] \\ \frac{n_{i,2}}{V_{i,2}-V_{i,1}} & V \in]V_{i,1}, V_{i,2}] \\ \frac{n_{i,3}}{V_{i,3}-V_{i,2}} & V \in]V_{i,2}, V_{i,3}] \\ \frac{n_{i,4}}{V_{i,4}-V_{i,3}} & V \in]V_{i,3}, V_{i,4}] \\ 0 & \text{else} \end{cases} \quad (8.6)$$

This size distribution is inserted into dust moment definition:

$$\begin{aligned} \rho L_{j,i} &= \int_{V_{i,0}}^{V_{i,1}} \frac{n_{i,1}}{V_{i,1}-V_{i,0}} V^{j/3} dV + \int_{V_{i,1}}^{V_{i,2}} \frac{n_{i,2}}{V_{i,2}-V_{i,1}} V^{j/3} dV \\ &+ \int_{V_{i,2}}^{V_{i,3}} \frac{n_{i,3}}{V_{i,3}-V_{i,2}} V^{j/3} dV + \int_{V_{i,3}}^{V_{i,4}} \frac{n_{i,4}}{V_{i,4}-V_{i,3}} V^{j/3} dV \end{aligned} \quad (8.7)$$

$$\begin{aligned} &= \frac{3}{j+3} \left(n_{i,1} \cdot \frac{V_{i,1}^{j/3+1} - V_{i,0}^{j/3+1}}{V_{i,1} - V_{i,0}} + n_{i,2} \cdot \frac{V_{i,2}^{j/3+1} - V_{i,1}^{j/3+1}}{V_{i,2} - V_{i,1}} \right. \\ &+ \left. n_{i,3} \cdot \frac{V_{i,3}^{j/3+1} - V_{i,2}^{j/3+1}}{V_{i,3} - V_{i,2}} + n_{i,4} \cdot \frac{V_{i,4}^{j/3+1} - V_{i,3}^{j/3+1}}{V_{i,4} - V_{i,3}} \right) \end{aligned} \quad (8.8)$$

$$= (n_{i,1} \cdot c_{i,j,1} + n_{i,2} \cdot c_{i,j,2} + n_{i,3} \cdot c_{i,j,3} + n_{i,4} \cdot c_{i,j,4}) \quad (8.9)$$

The constants $c_{i,j,k} = \frac{3}{j+3} \frac{V_{i,k}^{j/3+1} - V_{i,k-1}^{j/3+1}}{V_{i,k} - V_{i,k-1}}$ rely solely on the defined sub-bin boundaries. Solving this system of equations for $\forall j \in \{1, 2, 3, 4\}$ analytically permits to derive expressions for



the $n_{i,k}$ from the current dust moments:

$$\begin{aligned}
n_{i,1} = & \left(\left(c_{i,2,2}(c_{i,3,4}c_{i,4,3} - c_{i,3,3}c_{i,4,4}) + c_{i,2,3}(c_{i,3,2}c_{i,4,4} - c_{i,3,4}c_{i,4,2}) \right. \right. \\
& \left. \left. + c_{i,2,4}(c_{i,3,3}c_{i,4,2} - c_{i,3,2}c_{i,4,3}) \right) \cdot L_{1,i} \right. \\
& + \left(c_{i,1,2}(c_{i,3,3}c_{i,4,4} - c_{i,3,4}c_{i,4,3}) + c_{i,1,3}(c_{i,3,4}c_{i,4,2} - c_{i,3,2}c_{i,4,4}) \right. \\
& \left. + c_{i,1,4}(c_{i,3,2}c_{i,4,3} - c_{i,3,3}c_{i,4,2}) \right) \cdot L_{2,i} \\
& + \left(c_{i,1,2}(c_{i,2,4}c_{i,4,3} - c_{i,2,3}c_{i,4,4}) + c_{i,1,3}(c_{i,2,2}c_{i,4,4} - c_{i,2,4}c_{i,4,2}) \right. \\
& \left. + c_{i,1,4}(c_{i,2,3}c_{i,4,2} - c_{i,2,2}c_{i,4,3}) \right) \cdot L_{3,i} \\
& + \left(c_{i,1,2}(c_{i,2,3}c_{i,3,4} - c_{i,2,4}c_{i,3,3}) + c_{i,1,3}(c_{i,2,4}c_{i,3,2} - c_{i,2,2}c_{i,3,4}) \right. \\
& \left. + c_{i,1,4}(c_{i,2,2}c_{i,3,3} - c_{i,2,3}c_{i,3,2}) \right) \cdot L_{4,i} \left. \right) \\
& / \left(c_{i,1,1} \cdot \left(c_{i,2,2}(c_{i,3,3}c_{i,4,4} - c_{i,3,4}c_{i,4,3}) + c_{i,2,3}(c_{i,3,4}c_{i,4,2} - c_{i,3,2}c_{i,4,4}) \right. \right. \\
& \left. \left. + c_{i,2,4}(c_{i,3,2}c_{i,4,3} - c_{i,3,3}c_{i,4,2}) \right) \right. \\
& + c_{i,1,2} \cdot \left(c_{i,2,1}(c_{i,3,4}c_{i,4,3} - c_{i,3,3}c_{i,4,4}) + c_{i,2,3}(c_{i,3,1}c_{i,4,4} - c_{i,3,4}c_{i,4,1}) \right. \\
& \left. + c_{i,2,4}(c_{i,3,3}c_{i,4,1} - c_{i,3,1}c_{i,4,3}) \right) \left. \right) \\
& + c_{i,1,3} \cdot \left(c_{i,2,1}(c_{i,3,2}c_{i,4,4} - c_{i,3,4}c_{i,4,2}) + c_{i,2,2}(c_{i,3,4}c_{i,4,1} - c_{i,3,1}c_{i,4,4}) \right. \\
& \left. + c_{i,2,4}(c_{i,3,1}c_{i,4,2} - c_{i,3,2}c_{i,4,1}) \right) \left. \right) \\
& + c_{i,1,4} \cdot \left(c_{i,2,1}(c_{i,3,3}c_{i,4,2} - c_{i,3,2}c_{i,4,3}) + c_{i,2,2}(c_{i,3,1}c_{i,4,3} - c_{i,3,3}c_{i,4,1}) \right. \\
& \left. + c_{i,2,3}(c_{i,3,2}c_{i,4,1} - c_{i,3,1}c_{i,4,2}) \right) \left. \right) \left. \right) \quad (8.10)
\end{aligned}$$

Similar expressions for $n_{i,2}$, $n_{i,3}$ and $n_{i,4}$ follow through cyclic permutation of the coefficients $c_{i,j,k}$. Though possibly confusing on the first look, computational effort is negligible because all terms except for the the dust moments can be calculated before the actual model run. Merely, twenty float variables would have to be stored per grain volume interval i , independent from the number of layers/voxels. Test calculations for arbitrary definitions of the sub-bin boundaries and the dust moments have confirmed the reliability of this closure condition.

The new formulation provides two benefits for the model. On one hand, the exact number of dust grains per installed bin is determined, which permits a more detailed and less constrained calculation of the dust opacity than in previous models. On the other hand, the conventional double delta-peaked grain size distribution of the DRIFT model is inadequate for the calculation of particle numbers at the boundaries between grain volume intervals i . Nevertheless, these are strictly required in order to determine exchange rates $J_{l,i}$ and $J_{u,i}$ between these intervals properly. The new method meets this requirement.

The new closure condition is:

$$L_{0,i}(L_{1,i}, L_{2,i}, L_{3,i}, L_{4,i}) = n_{i,1} + n_{i,2} + n_{i,3} + n_{i,4} \quad (8.11)$$

Exchange rates between grain volume intervals; Following the derivation of an appropriate grain size distribution, it is possible to determine the exchange rates $J_{l,i}$ and $J_{u,i}$.

A growth reaction of species s increases the grain volume by ΔV_s . Hence, grains of $V \in]V_{l,i} - V_s, V_{l,i}]$ can migrate from interval $i - 1$ to interval i through growth of species

s . Vice versa, grains of $V \in]V_{l,i}, V_{l,i} + V_s]$ can migrate from i to $i - 1$ through evaporation of species s . The particle number density affected by the exchange from $i - 1$ to i through growth is $n_{i-1,4} \frac{\Delta V_s}{V_{i-1,4} - V_{i-1,3}}$ while the corresponding particle number density affected by the counteracting evaporation reaction is $n_{i,1} \frac{\Delta V_s}{V_{i,1} - V_{i,0}}$. Considering these particle numbers in Eq. 3.11 in place of the grain size distribution provides

$$J_s(V_{l,i}, \vec{r}) = \sum_{r_s} \left(n_{i-1,4} \frac{A(V_{l,i} - \Delta V_s)}{V_{i-1,4} - V_{i-1,3}} - n_{i,1} \frac{A_s(V_{l,i} - \Delta V_s)}{(V_{i,1} - V_{i,0}) \cdot S_{r_s}} \right) \cdot \Delta V_s \cdot n_{r_s, \text{key}} \left(\frac{kT}{2\pi m_{r_s, \text{key}}} \right)^{1/2} \cdot \alpha_{r_s} \quad (8.12)$$

There is one exception to this equation. For $i = 0$, the lower boundary is V_l , below which the rate equations do not apply but instead the nucleation rate J (Eq. 3.3). Therefore, the valid expression of this case is

$$J_s(V_{l,0}, \vec{r}) = J_{l,s} - \sum_{r_s} n_{0,1} \frac{A_s(V_{l,0} - \Delta V_s)}{(V_{0,1} - V_{0,0}) \cdot S_{r_s}} \cdot \Delta V_s \cdot n_{r_s, \text{key}} \left(\frac{kT}{2\pi m_{r_s, \text{key}}} \right)^{1/2} \cdot \alpha_{r_s} \quad (8.13)$$

The final exchange rates follow from the two previous equations and $J_s(V_{u,i}) = J_s(V_{l,i+1})$:

$$V_{l,i}^{j/3} J(V_{l,i}) - V_{u,i}^{j/3} J(V_{u,i}) = \sum_s \left(V_{l,i}^{j/3} J_s(V_{l,i}) - V_{u,i}^{j/3} J_s(V_{u,i}) \right) \quad (8.14)$$

Conclusion: With these steps, the new model is formally complete, because the related element conservation equations are not affected by this transformation. The number of moment equations that have to be solved simultaneously is increased by a factor equal to the number of considered volume intervals. However, the numerics are less strained by artificial definitions of the grain size distribution. The additional equations become entirely unproblematic when switching the numerics from solving the stationary system of equations to a time-dependent relaxation. As a side-effect, such a relaxation allows for a parallelisation of the numerics that is otherwise precluded (Sec. 4.2). The parallelization is especially convenient since the PHOENIX atmosphere code and the computing clusters are specifically designed for parallelized applications. Furthermore, the time-dependence rids the dust model of the need for an own chemical solver for the gas phase, which the stationary cloud model has to call during every iterative step.

Due to the new closure condition, the number of data points of the grain size distribution is at least doubled, compared to the currently implemented dust model with the double delta-peaked distribution. By increasing the number of grain size intervals, the number of data points of the grain size distribution can be optimized for a compromise between computational effort and precision of the results.

8.3 Spherical 1D model

Motivation: On the basis of Sec. 3.7, the new model of the previous section (Sec. 8.2) can be expanded to work consistently with spherical geometry atmosphere models. As mentioned



above, simulations show that this becomes relevant for the geometrically thick dust clouds of low gravity atmospheres, i.e., young brown dwarfs and exoplanets.

Spherical flow rates: Presuming, the model consists of voxel with spherical stacking ($\vec{r} = (r \in \mathbb{R}_+, \phi \in [0, 2\pi], \theta \in [0, \pi])$) and voxel spacing $\vec{\Delta r} = (\Delta r, \Delta\phi, \Delta\theta)$, the enveloping surface is, again, simply the sum of the six voxel facings. The area of the voxel faces is

$$\begin{aligned}
A_{\text{west/east}}(\vec{r}) &= \frac{\Delta\theta}{2} \left((r + \Delta r/2)^2 - (r - \Delta r/2)^2 \right) \\
A_{\text{north}}(\vec{r}) &= \frac{\Delta\phi}{2} \left((r + \Delta r/2)^2 - (r - \Delta r/2)^2 \right) \cdot \sin(\theta + \Delta\theta/2) \\
A_{\text{south}}(\vec{r}) &= \frac{\Delta\phi}{2} \left((r + \Delta r/2)^2 - (r - \Delta r/2)^2 \right) \cdot \sin(\theta - \Delta\theta/2) \\
A_{\text{top}}(\vec{r}) &= \Delta\phi (r + \Delta r/2)^2 \cdot |\cos(\theta - \Delta\theta/2) - \cos(\theta + \Delta\theta/2)| \\
A_{\text{bottom}}(\vec{r}) &= \Delta\phi (r - \Delta r/2)^2 \cdot |\cos(\theta - \Delta\theta/2) - \cos(\theta + \Delta\theta/2)|
\end{aligned}$$

The voxel volume is given by

$$V_v(\vec{r}) = \frac{\Delta\phi}{3} \cdot \left((r + \Delta r/2)^3 - (r - \Delta r/2)^3 \right) \cdot |\cos(\theta - \Delta\theta/2) - \cos(\theta + \Delta\theta/2)|$$

From these quantities, the net flow of grains can be constructed as follows:

$$\begin{aligned}
\Phi(\vec{N}_s, \vec{r}) &= f(V, \vec{r} - \vec{1}_r/2) v_{d,r}(\vec{r} - \vec{1}_r/2) A_{\text{bottom}}(\vec{r}) \\
&- f(V, \vec{r} + \vec{1}_r/2) v_{d,r}(\vec{r} + \vec{1}_r/2) A_{\text{top}}(\vec{r}) \\
&+ f(V, \vec{r} - \vec{1}_\phi/2) v_{d,\phi}(\vec{r} - \vec{1}_\phi/2) A_{\text{west/east}}(\vec{r}) \\
&- f(V, \vec{r} + \vec{1}_\phi/2) v_{d,\phi}(\vec{r} + \vec{1}_\phi/2) A_{\text{west/east}}(\vec{r}) \\
&+ f(V, \vec{r} - \vec{1}_\theta/2) v_{d,\theta}(\vec{r} - \vec{1}_\theta/2) A_{\text{south}}(\vec{r}) \\
&- f(V, \vec{r} + \vec{1}_\theta/2) v_{d,\theta}(\vec{r} + \vec{1}_\theta/2) A_{\text{north}}(\vec{r})
\end{aligned} \tag{8.15}$$

Distributed over the voxel volume, the flow rate becomes:

$$\begin{aligned}
\frac{\partial f(\vec{N}_s, \vec{r})}{\partial \vec{r}} \frac{d\vec{r}}{dt} &= \frac{3(r - \Delta r/2)^2}{(r + \Delta r/2)^3 - (r - \Delta r/2)^3} f(V, \vec{r} - \vec{1}_r/2) v_{d,r}(\vec{r} - \vec{1}_r/2) \\
&- \frac{3(r + \Delta r/2)^2}{(r + \Delta r/2)^3 - (r - \Delta r/2)^3} f(V, \vec{r} + \vec{1}_r/2) v_{d,r}(\vec{r} + \vec{1}_r/2) \\
&+ \frac{3}{2} \cdot \frac{((r + \Delta r/2)^2 - (r - \Delta r/2)^2)}{((r + \Delta r/2)^3 - (r - \Delta r/2)^3)} \cdot \frac{1}{|\cos(\theta - \Delta\theta/2) - \cos(\theta + \Delta\theta/2)|} \\
&\cdot \left[\frac{\Delta\theta}{\Delta\phi} \cdot \left(f(V, \vec{r} - \vec{1}_\phi/2) v_{d,\phi}(\vec{r} - \vec{1}_\phi/2) - f(V, \vec{r} + \vec{1}_\phi/2) v_{d,\phi}(\vec{r} + \vec{1}_\phi/2) \right) \right. \\
&+ \sin(\theta - \Delta\theta/2) f(V, \vec{r} - \vec{1}_\theta/2) v_{d,\theta}(\vec{r} - \vec{1}_\theta/2) \\
&\left. - \sin(\theta + \Delta\theta/2) f(V, \vec{r} + \vec{1}_\theta/2) v_{d,\theta}(\vec{r} + \vec{1}_\theta/2) \right]
\end{aligned} \tag{8.16}$$

Employing the same simplifications as for the plane-parallel static vertical 1D case (Sec. 3.7), the spherical geometry flow rate simplifies to:

$$\left. \frac{\partial f(\vec{N}_s, z)}{\partial z} \frac{dz}{dt} \right|_{\text{gravity}} = \frac{3 \cdot f(V, z + \Delta z/2) v_{\text{drift}}(z + \Delta z/2) \cdot (z + \Delta z/2)^2}{(z + \Delta z/2)^3 - (z - \Delta z/2)^3} - \frac{3 \cdot f(V, z - \Delta z/2) v_{\text{drift}}(z - \Delta z/2) \cdot (z - \Delta z/2)^2}{(z + \Delta z/2)^3 - (z - \Delta z/2)^3} \quad (8.17)$$

The term for convective motion is identical except for v_{conv} in place of v_{drift} . Likewise, the convective overshooting would have to be affected by a spherical geometry. However, since the mixing timescales are only roughly approximated anyway, it will not be treated here.

Moment equations & discussion: The dust growth and evaporation are not directly affected by the geometry of the atmosphere. Therefore, all required terms have been derived to revisit the fundamental rate equation (Eq. 3.26). Following the same arguments as in Sec. 8.2 results in the spherical geometry set of moment equations:

$$\begin{aligned} \frac{d}{dt} \rho L_{j,i}(z) &= \underbrace{V_{l,i}^{j/3} J(V_{l,i}, z) - V_{u,i}^{j/3} J(V_{u,i}, z)}_{\text{exchange with lower/higher volume intervals}} + \underbrace{\frac{j}{3} \chi_{\text{net}} \rho L_{j-1,i}(z)}_{\text{growth/evaporation}} \quad (8.18) \\ &+ \underbrace{3\xi(z + \Delta z/2) \rho_{d,i}(z + \Delta z/2) \frac{(z + \Delta z/2)^2}{(z + \Delta z/2)^3 - (z - \Delta z/2)^3} \frac{L_{j+1,i}(z + \Delta z/2)}{c_{th}(z + \Delta z/2)}}_{\text{gravitational settling inflow}} \\ &- \underbrace{3\xi(z - \Delta z/2) \rho_{d,i}(z - \Delta z/2) \frac{(z - \Delta z/2)^2}{(z + \Delta z/2)^3 - (z - \Delta z/2)^3} \frac{L_{j+1,i}(z - \Delta z/2)}{c_{th}(z - \Delta z/2)}}_{\text{gravitational settling outflow}} \\ &+ \begin{cases} \left\{ \begin{aligned} &+ \frac{3 \cdot \rho(V, z + \Delta z/2) L_{j,i}(V, z + \Delta z/2) v_{\text{conv}}(z + \Delta z/2) \cdot (z + \Delta z/2)^2}{(z + \Delta z/2)^3 - (z - \Delta z/2)^3} && \text{convective} \\ &- \frac{3 \cdot \rho(V, z - \Delta z/2) L_{j,i}(V, z - \Delta z/2) v_{\text{conv}}(z - \Delta z/2) \cdot (z - \Delta z/2)^2}{(z + \Delta z/2)^3 - (z - \Delta z/2)^3} \end{aligned} \right. \\ \left. - \frac{\rho L_{j,i}(z)}{\tau_{\text{mix}}} \right. && \text{not convective} \end{cases} \end{aligned}$$

Although these moment equations look much more complicated, the computational effort is only marginally increased, compared to the plane-parallel case. Nonetheless, the significance of this spherical treatment has yet to be tested. For the typically low ratios of the geometrical thickness of the photosphere and total radius of very low-mass stars and most brown dwarfs, there is no general, groundbreaking influence to expect. However, for young brown dwarfs and hot giant planets, this ratio can exceed 5%. Within this niche, i.e., low gravity objects, sphericity may cause perceivable differences in the cloud structure and spectra.

8.4 Time-dependent 3D model in spherical geometry

Motivation: Though very expensive with respect to computing time, a simulation of dust clouds in a proper time-dependent 3D environment has the clear advantage of requiring much



less fundamental assumptions. With mixing mechanisms still hardly understood, 1D models rely on overly simple and abstract descriptions. In contrast, hydrodynamical simulations automatically provide gas velocities that affect the distribution of elements and dust particles across the atmosphere. A systematic distinction of convective and non-convective layers, as done for the 1D models, is not necessary with hydrodynamical input.

Woitke (2006) has integrated the standard dust moment method into the FLASH code (Fryxell et al., 2000). Likewise, the modified method of the previous sections can be coupled with this hydro-code.

Derivation: The grain growth and evaporation are not affected by the geometry of the atmosphere. Only the grain flow becomes more complicated due to the additional spatial dimensions.

The velocity of the dust particles in Eq. 8.15 is substituted by $\vec{v}_d = \vec{v}_g + \vec{v}_{\text{drift}} = (v_r, v_\theta, v_\phi) + (-v_{\text{drift}}, 0, 0)$. Only the vertical gravitational settling terms are non-zero. Convective overshooting and other mixing mechanisms are considered intrinsically in the gas velocities from the hydrodynamics. The remaining eight flow rate terms are inserted into the fundamental rate equation (Eq. 3.26), followed by the usual conversion into the dust moment equations:

$$\begin{aligned}
\frac{d}{dt} \rho L_{j,i}(\vec{r}) &= V_{l,i}^{j/3} \cdot J(V_{l,i}, \vec{r}) - V_{u,i}^{j/3} \cdot J(V_{u,i}, \vec{r}) + \frac{j}{3} \chi_{\text{net}}(\vec{r}) \cdot \rho(\vec{r}) \cdot L_{j-1,i}(\vec{r}) \\
&+ 3\xi \left(\vec{r} + \frac{\vec{1}_r}{2} \right) \cdot \rho_{d,i} \left(\vec{r} + \frac{\vec{1}_r}{2} \right) \cdot \frac{(r + \frac{\Delta r}{2})^2}{(r + \frac{\Delta r}{2})^3 - (r - \frac{\Delta r}{2})^3} \frac{L_{j+1,i} \left(\vec{r} + \frac{\vec{1}_r}{2} \right)}{c_{th} \left(\vec{r} + \frac{\vec{1}_r}{2} \right)} \\
&- 3\xi \left(\vec{r} - \frac{\vec{1}_r}{2} \right) \cdot \rho_{d,i} \left(\vec{r} - \frac{\vec{1}_r}{2} \right) \cdot \frac{(r - \frac{\Delta r}{2})^2}{(r + \frac{\Delta r}{2})^3 - (r - \frac{\Delta r}{2})^3} \frac{L_{j+1,i} \left(\vec{r} - \frac{\vec{1}_r}{2} \right)}{c_{th} \left(\vec{r} - \frac{\vec{1}_r}{2} \right)} \\
&+ \frac{3(r - \frac{\Delta r}{2})^2}{(r + \frac{\Delta r}{2})^3 - (r - \frac{\Delta r}{2})^3} \cdot v_r \left(\vec{r} - \frac{\vec{1}_r}{2} \right) \cdot \rho \left(V, \vec{r} - \frac{\vec{1}_r}{2} \right) \cdot L_{j,i} \left(V, \vec{r} - \frac{\vec{1}_r}{2} \right) \\
&- \frac{3(r + \frac{\Delta r}{2})^2}{(r + \frac{\Delta r}{2})^3 - (r - \frac{\Delta r}{2})^3} \cdot v_r \left(\vec{r} + \frac{\vec{1}_r}{2} \right) \cdot \rho \left(V, \vec{r} + \frac{\vec{1}_r}{2} \right) \cdot L_{j,i} \left(V, \vec{r} + \frac{\vec{1}_r}{2} \right) \\
&\vdots
\end{aligned}$$

$$\begin{aligned}
 & \vdots \\
 & + \frac{3}{2} \cdot \frac{\left(r + \frac{\Delta r}{2}\right)^2 - \left(r - \frac{\Delta r}{2}\right)^2}{\left(\left(r + \frac{\Delta r}{2}\right)^3 - \left(r - \frac{\Delta r}{2}\right)^3\right)} \cdot \frac{1}{|\cos(\theta - \Delta\theta/2) - \cos(\theta + \Delta\theta/2)|} \\
 & \cdot \left[\frac{\Delta\theta}{\Delta\phi} \cdot v_\phi \left(\vec{r} - \frac{\vec{1}_\phi}{2}\right) \cdot \rho \left(V, \vec{r} - \frac{\vec{1}_\phi}{2}\right) \cdot L_{j,i} \left(V, \vec{r} - \frac{\vec{1}_\phi}{2}\right) \right. \\
 & - \frac{\Delta\theta}{\Delta\phi} \cdot v_\phi \left(\vec{r} + \frac{\vec{1}_\phi}{2}\right) \cdot \rho \left(V, \vec{r} + \frac{\vec{1}_\phi}{2}\right) \cdot L_{j,i} \left(V, \vec{r} + \frac{\vec{1}_\phi}{2}\right) \\
 & + \sin \left(\theta - \frac{\Delta\theta}{2}\right) \cdot v_\theta \left(\vec{r} - \frac{\vec{1}_\theta}{2}\right) \cdot \rho \left(V, \vec{r} - \frac{\vec{1}_\theta}{2}\right) \cdot L_{j,i} \left(V, \vec{r} - \frac{\vec{1}_\theta}{2}\right) \\
 & \left. - \sin \left(\theta + \frac{\Delta\theta}{2}\right) \cdot v_\theta \left(\vec{r} + \frac{\vec{1}_\theta}{2}\right) \cdot \rho \left(V, \vec{r} + \frac{\vec{1}_\theta}{2}\right) \cdot L_{j,i} \left(V, \vec{r} + \frac{\vec{1}_\theta}{2}\right) \right] \quad (8.19)
 \end{aligned}$$

This formulation is already adapted to the discretized geometry of the model atmosphere. A plane-parallel analogon follows trivially for $\lim \frac{\Delta r}{r} \rightarrow 0$.

Discussion: The development of the local dust quantities during a time-step depends on the local dust moments and those of adjacent voxels. Although the computation of the cloud can be parallelized spatially, the data of the adjacent voxel has to be updated regularly. One of the key problems of the time-dependent simulation of dust clouds is the length of the time-steps. Due to the fast precipitation in the higher cloud layers, the $d\frac{dL_{j,i}}{dt}/dL_{j,i}$ will be high there, which will require rather short time-steps. Therefore, the computational effort will be high unless errors in the calculation of the upper layers are accepted.



9 Future prospects

This work represents a theoretical study of the formation of dust clouds and their development over the stellar parameter space. Furthermore, the quality of the models was tested with observations. Conclusions on dust clouds based on the current standard DRIFT-PHOENIX grid are summarized in Sec. 7. The model formalism was expanded in order to overcome the most critical deficiencies of the current model. The implementation of the improved model is pending, followed by integration with the FLASH code and PHOENIX/3D.

Preliminary calculations that consider forming convection zones inside the dust cloud prove that this mechanism is quickly able to sweep away most of the atmospheric dust, which could explain the absence of clouds in late L- and T type objects as suggested by Burgasser et al. (2002b) and others. Furthermore, these simulations show indications for local, temporal variability of this effect. This will be investigated further.

At the same time, the existing atmosphere models will be used for further research on objects between spectral types M6...L5. For instance, higher resolution spectra of these atmosphere model grid are currently being calculated and will be made available to the community. An upcoming application of these high resolution spectra is the study of gravity-sensitive features. In addition, there are plans to use the models for the analysis of transit observations of extrasolar planets and their host stars.

In the past there have been a number of requests for irradiated models involving dust for studies on hot exoplanets. One of the planned applications is the determination of boundary conditions for modelling of giant planet interiors (e.g., Nettelmann et al., 2010). Respective irradiation models are currently being tested (Schweitzer, priv. comm.).

Likewise, a large-scale systematic comparison of spectral properties of the DRIFT-PHOENIX and DUSTY/COND-PHOENIX models and possibly competitive models has been started (Lee & Helling, priv. comm.)

With the consistent results of the new EOS module, new evolutionary calculations based on the new model grid have become possible and are planned to be carried out. It will be interesting to study how strongly dust clouds affect the aging of the latest type stars and, more interestingly, substellar objects.

The study of charge separation in dust clouds and incidental discharges by Helling et al. (2011) is continued and will involve the DRIFT-PHOENIX models.

As noted in this work, the introduction of additional solid species to the model relies on the available data. Furthermore, some of the current refractive index data sets are only poorly resolved with respect to the wavelength and should be replaced in order to resolve dust-based features in spectra properly. Therefore, it will be strictly necessary to gather more and better data in the future.

A much more exotic, albeit fascinating, application of the dust model could be the simulation of accretion streams of cataclysmic variables. According to Hessman (1999), the

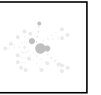
involved gas is dense and cool enough to sustain dust formation. These particles need not necessarily be destroyed upon reaching the accretion disk but could remain intact due to stream overflow, therefore, be responsible for currently unexplained features in spectra of cataclysmic variables.



Bibliography

- Ackerman, A. S. and Marley, M. S. (2001). *ApJ*, 556:872–884.
- Allard, F. and Hauschildt, P. H. (1995). *ApJ*, 445:433–450.
- Allard, F., Hauschildt, P. H., Alexander, D. R. and Starrfield, S. (1997). *ARA&A*, 35:137–177.
- Allard, F., Hauschildt, P. H., Alexander, D. R., Tamanai, A. and Schweitzer, A. (2001). *ApJ*, 556:357–372.
- Asplund, M., Grevesse, N. and Sauval, A. J. (2005). In T. G. Barnes III & F. N. Bash, editor, *Cosmic Abundances as Records of Stellar Evolution and Nucleosynthesis*, volume 336 of *Astronomical Society of the Pacific Conference Series*, pages 25–+.
- Baraffe, I. and Chabrier, G. (2010). *A&A*, 521:A44+.
- Baraffe, I., Chabrier, G., Barman, T. S., Allard, F. and Hauschildt, P. H. (2003). *A&A*, 402:701–712.
- Barman, T. (2011). . in prep.
- Basri, G. (2000). *ARA&A*, 38:485–519.
- Becklin, E. E. and Zuckerman, B. (1988). *Nature*, 336:656–658.
- Beers, T. C. and Christlieb, N. (2005). *ARA&A*, 43:531–580.
- Béjar, V. J. S., Martín, E. L., Zapatero Osorio, M. R., Rebolo, R., Barrado y Navascués, D., Bailer-Jones, C. A. L., Mundt, R., Baraffe, I., Chabrier, C. and Allard, F. (2001). *ApJ*, 556:830–836.
- Biermann, L. (1932). *Zeitschrift für Astrophysik*, 5:117.
- Blum, J. and Wurm, G. (2008). *ARA&A*, 46:21–56.
- Borucki, W. J. and Summers, A. L. (1984). *Icarus*, 58:121–134.
- Bosch, S., Ferre-Borrull, J., Leinfellner, N. and Canillas, A. (2000). *Surface Science*, 453:9–17(9).
- Bruggeman, D. A. G. (1935). *Annalen der Physik*, 24:636–664.

- Burgasser, A. J. (2007). *ApJ*, 659:655–674.
- Burgasser, A. J., Kirkpatrick, J. D., Brown, M. E., Reid, I. N., Burrows, A., Liebert, J., Matthews, K., Gizis, J. E., Dahn, C. C., Monet, D. G., Cutri, R. M. and Skrutskie, M. F. (2002a). *ApJ*, 564:421–451.
- Burgasser, A. J., Liu, M. C., Ireland, M. J., Cruz, K. L. and Dupuy, T. J. (2008). *ApJ*, 681:579–593.
- Burgasser, A. J., Looper, D. L., Kirkpatrick, J. D. and Liu, M. C. (2007). *ApJ*, 658:557–568.
- Burgasser, A. J., Marley, M. S., Ackerman, A. S., Saumon, D., Lodders, K., Dahn, C. C., Harris, H. C. and Kirkpatrick, J. D. (2002b). *AJL*, 571:L151–L154.
- Burgasser, A. J. and McElwain, M. W. (2006). *AJ*, 131:1007–1014.
- Burgasser, A. J., McElwain, M. W., Kirkpatrick, J. D., Cruz, K. L., Tinney, C. G. and Reid, I. N. (2004). *AJ*, 127:2856–2870.
- Burgasser, A. J., Witte, S., Helling, C. and Hauschildt, P. H. (2009). *ApJ*, 697:148–159.
- Burrows, A. and Sharp, C. M. (1999). *ApJ*, 512:843–863.
- Burrows, A., Sudarsky, D. and Hubeny, I. (2006). *ApJ*, 640:1063–1077.
- Cannon, C. J. (1973). *ApJ*, 185:621–630.
- Catala, C., Mangeney, A., Gautier, D., Auvergne, M., Baglin, A., Goupil, M. J., Michel, E., Zahn, J. P., Magnan, A., Vuillemin, A., Boumier, P., Gabriel, A., Lemaire, P., Turck-Chieze, S., Dzitko, H., Mosser, B. and Bonneau, F. (1995). In R. K. Ulrich, E. J. Rhodes Jr., & W. Dappen, editor, *GONG 1994. Helio- and Astro-Seismology from the Earth and Space*, volume 76 of *Astronomical Society of the Pacific Conference Series*, pages 426–+.
- Chabrier, G. and Baraffe, I. (2000). *ARA&A*, 38:337–377.
- Chabrier, G., Baraffe, I., Allard, F. and Hauschildt, P. (2000). *ApJ*, 542:464–472.
- Chabrier, G., Baraffe, I., Allard, F. and Hauschildt, P. H. (2005). *ArXiv e-prints*.
- Chiu, K., Fan, X., Leggett, S. K., Golimowski, D. A., Zheng, W., Geballe, T. R., Schneider, D. P. and Brinkmann, J. (2006). *AJ*, 131:2722–2736.
- Clark, P. C., Glover, S. C. O. and Klessen, R. S. (2008). *ApJ*, 672:757–764.
- Cooper, C. S., Sudarsky, D., Milsom, J. A., Lunine, J. I. and Burrows, A. (2003). *ApJ*, 586:1320–1337.
- Cruz, K. L., Burgasser, A. J., Reid, I. N. and Liebert, J. (2004). *AJL*, 604:L61–L64.
- Dehn, M. (2007). PhD thesis, Universität Hamburg.



- Delitsky, M. L. and Baines, K. H. (2007). In *Bulletin of the American Astronomical Society*, volume 38 of *Bulletin of the American Astronomical Society*, pages 444–+.
- Dunaeva, A. N., Antsyshkin, D. V. and Kuskov, O. L. (2010). *Solar System Research*, 44:202–222.
- Dupuy, T. J., Liu, M. C., Bowler, B. P., Cushing, M. C., Helling, C., Witte, S. and Hauschildt, P. (2010). *ApJ*, 721:1725–1747.
- Epchtein, N. and Mamon, G. A. (1992). In G. A. Mamon & D. Gerbal, editor, *Distribution of Matter in the Universe*, pages 382–387.
- Frebel, A., Aoki, W., Christlieb, N., Ando, H., Asplund, M., Barklem, P. S., Beers, T. C., Eriksson, K., Fechner, C., Fujimoto, M. Y., Honda, S., Kajino, T., Minezaki, T., Nomoto, K., Norris, J. E., Ryan, S. G., Takada-Hidai, M., Tsangarides, S. and Yoshii, Y. (2005). In Hill, V., François, P. and Primas, F., editors, *From Lithium to Uranium: Elemental Tracers of Early Cosmic Evolution*, volume 228 of *IAU Symposium*, pages 207–212.
- Frebel, A., Collet, R., Eriksson, K., Christlieb, N. and Aoki, W. (2008). *ApJ*, 684:588–602.
- Freytag, B., Allard, F., Ludwig, H., Homeier, D. and Steffen, M. (2010). *A&A*, 513:A19+.
- Fryxell, B., Olson, K., Ricker, P., Timmes, F. X., Zingale, M., Lamb, D. Q., MacNeice, P., Rosner, R., Truran, J. W. and Tufo, H. (2000). *AJS*, 131:273–334.
- Gail, H.-P., Keller, R. and Sedlmayr, E. (1984). *A&A*, 133:320–332.
- Gail, H.-P. and Sedlmayr, E. (1988). *A&A*, 206:153–168.
- Gauger, A., Sedlmayr, E. and Gail, H. (1990). *A&A*, 235:345–361.
- Gelino, C., Kirkpatrick, D. and Burgasser, A. (2009). DwarfArchives.org: Photometry, spectroscopy, and astrometry of M, L, and T dwarfs. URL: <http://spider.ipac.caltech.edu/staff/davy/ARCHIVE/>.
- Goldman, B., Cushing, M. C., Marley, M. S., Artigau, É., Baliyan, K. S., Béjar, V. J. S., Caballero, J. A., Chanover, N., Connelley, M., Doyon, R., Forveille, T., Ganesh, S., Gelino, C. R., Hammel, H. B., Holtzman, J., Joshi, S., Joshi, U. C., Leggett, S. K., Liu, M. C., Martín, E. L., Mohan, V., Nadeau, D., Sagar, R. and Stephens, D. (2008). *A&A*, 487:277–292.
- Golimowski, D. A., Leggett, S. K., Marley, M. S., Fan, X., Geballe, T. R., Knapp, G. R., Vrba, F. J., Henden, A. A., Luginbuhl, C. B., Guetter, H. H., Munn, J. A. and Canzian, B. e. a. (2004). *AJ*, 127:3516–3536.
- Hauschildt, P. H., Barman, T., Baron, E. and Allard, F. (2003). In *Stellar Atmosphere Modeling*, volume 288 of *ASP Conference Series*, pages 227–+.

- Hauschildt, P. H. and Baron, E. (1999). *Journal of Computational and Applied Mathematics*, 109:41–63.
- Hauschildt, P. H. and Baron, E. (2007). *PHOENIX version 15 (manual)*. <http://www.hs.uni-hamburg.de/EN/For/ThA/phoenix/Manual/Manual.pdf>.
- Hayashi, C. (1962). *Pub. A.S.J.*, 13:450–452.
- Hayashi, C. and Nakano, T. (1963). *Progress of Theoretical Physics*, 30:460–474.
- Helling, C., Ackerman, A., Allard, F., Dehn, M., Hauschildt, P., Homeier, D., Lodders, K., Marley, M., Rietmeijer, F., Tsuji, T. and Woitke, P. (2008a). *MNRAS*, 391:1854–1873.
- Helling, C., Dehn, M., Woitke, P. and Hauschildt, P. H. (2008b). *AJL*, 675:L105–L108.
- Helling, C., Jardine, M., Witte, S. and Diver, D. A. (2011). *ApJ*, 727:4–+.
- Helling, C. and Woitke, P. (2004). In J. Beaulieu, A. Lecavelier Des Etangs, & C. Terquem, editor, *Extrasolar Planets: Today and Tomorrow*, volume 321 of *Astronomical Society of the Pacific Conference Series*, pages 199–+.
- Helling, C. and Woitke, P. (2006). *A&A*, 455:325–338.
- Helling, C., Woitke, P. and Thi, W.-F. (2008c). *A&A*, 485:547–560.
- Hessman, F. V. (1999). *ApJ*, 510:867–873.
- Hubble, E. (1929). *Proceedings of the National Academy of Science*, 15:168–173.
- Jeans, J. H. (1902). *Philosophical Transactions of the Royal Society of London*, 199:1–53.
- Johnas, C. M. S., Helling, C., Dehn, M., Woitke, P. and Hauschildt, P. H. (2008a). *MNRAS*, 385:L120–L124.
- Johnas, C. M. S., Helling, C., Witte, S., Dehn, M., Woitke, P. and Hauschildt, P. H. (2008b). In D. Fischer, F. A. Rasio, S. E. Thorsett, & A. Wolszczan, editor, *Astronomical Society of the Pacific Conference Series*, volume 398 of *Astronomical Society of the Pacific Conference Series*, pages 393–+.
- Johnson, J. A. (2009). *Publications of the Astronomical Society of the Pacific*, 121:309–315.
- Jones, H. R. A. and Tsuji, T. (1997). *AJL*, 480:L39+.
- Kant, I. (1755). *Allgemeine Naturgeschichte und Theorie des Himmels*. Johann Friederich Petersen, first edition.
- Kirkpatrick, J. D. (2005). *ARA&A*, 43:195–245.
- Kirkpatrick, J. D., Barman, T. S., Burgasser, A. J., McGovern, M. R., McLean, I. S., Tinney, C. G. and Lowrance, P. J. (2006). *ApJ*, 639:1120–1128.



- Kleinmann, S. G. (1992). In A. V. Filippenko, editor, *Robotic Telescopes in the 1990s*, volume 34 of *Astronomical Society of the Pacific Conference Series*, pages 203–212.
- Kraus, A. L. and Hillenbrand, L. A. (2009). *ApJ*, 704:531–547.
- Kumar, S. S. (1963a). *ApJ*, 137:1126–+.
- Kumar, S. S. (1963b). *ApJ*, 137:1121–+.
- Lafrenière, D., Jayawardhana, R., Janson, M., Helling, C., Witte, S. and Hauschildt, P. (2011). *ArXiv e-prints*.
- Latham, D. W., Stefanik, R. P., Mazeh, T., Mayor, M. and Burki, G. (1989). *Nature*, 339:38–40.
- Lemaître, G. (1927). *Annales de la Societe Scietifique de Bruxelles*, 47:49–59.
- Looper, D. L., Burgasser, A. J., Kirkpatrick, J. D. and Swift, B. J. (2007). *AJL*, 669:L97–L100.
- Looper, D. L., Kirkpatrick, J. D., Cutri, R. M., Barman, T., Burgasser, A. J., Cushing, M. C., Roellig, T., McGovern, M. R., McLean, I. S., Rice, E., Swift, B. J. and Schurr, S. D. (2008). *ApJ*, 686:528–541.
- Ludwig, H.-G., Allard, F. and Hauschildt, P. H. (2002). *A&A*, 395:99–115.
- Lunine, J. I., Hubbard, W. B. and Marley, M. (1986). *ApJ*, 310:238–260.
- Mayor, M. and Queloz, D. (1995). *Nature*, 378:355–+.
- McElwain, M. W. and Burgasser, A. J. (2006). *AJ*, 132:2074–2081.
- McLean, I. S., McGovern, M. R., Burgasser, A. J., Kirkpatrick, J. D., Prato, L. and Kim, S. S. (2003). *ApJ*, 596:561–586.
- Mie, G. (1908). *Annalen der Physik*, 25:377.
- Mihalas, D. (1970). *Stellar Atmospheres*. San Francisco: Freeman, first edition.
- Mihalas, D. (1978). *Stellar Atmospheres*. San Francisco: Freeman, second edition.
- Mueller, R. F. and Saxena, S. K. (1977). *Chemical Petrology*. New York: Springer, first edition.
- Muench, A. A., Lada, C. J., Luhman, K. L., Muzerolle, J. and Young, E. (2007). *AJ*, 134:411–444.
- Nakajima, T., Oppenheimer, B. R., Kulkarni, S. R., Golimowski, D. A., Matthews, K. and Durrance, S. T. (1995). *Nature*, 378:463–+.

- Nettelmann, N., Kramm, U., Redmer, R. and Neuhäuser, R. (2010). *A&A*, 523:A26+.
- Neuhäuser, R., Schmidt, T. O. B., Seifahrt, A., Bedalov, A., Helling, C., Witte, S. and Hauschildt, P. H. (2009). In *Cool Stars 15 Proceedings*, 15th Cambridge Workshop.
- Noll, K. S., Geballe, T. R. and Marley, M. S. (1997). *AJL*, 489:L87+.
- Nolting, W. (2004). *Grundkurs Theoretische Physik 3: Elektrodynamik*. Springer, sixth edition.
- Omukai, K. (2008). In O’Shea, B. W. and Heger, A., editors, *First Stars III*, volume 990 of *American Institute of Physics Conference Series*, pages 63–67.
- Prandtl, L. (1925). *Zeitschrift für angewandte Mathematik und Mechanik*, 5:136–139.
- Rebolo, R., Martin, E. L. and Maguzza, A. (1992). *ApJ*, 389:L83–L86.
- Rebolo, R., Zapatero Osorio, M. R. and Martín, E. L. (1995). *Nature*, 377:129–131.
- Reid, I. N., Lewitus, E., Burgasser, A. J. and Cruz, K. L. (2006). *ApJ*, 639:1114–1119.
- Ribas, I. (2003). *A&A*, 400:297–302.
- Rice, E. L., Barman, T., McLean, I. S., Prato, L. and Kirkpatrick, J. D. (2009). *ArXiv e-prints*.
- Rutten, R. J. (2003). *Radiative Transfer in Stellar Atmospheres*. Utrecht University lecture notes, eighth edition.
- Saumon, D. and Marley, M. S. (2008). *ApJ*, 689:1327–1344.
- Saumon, D., Marley, M. S., Lodders, K. and Freedman, R. S. (2003). In E. Martín, editor, *Brown Dwarfs*, volume 211 of *IAU Symposium*, pages 345–+.
- Schmidt, T. O. B., Neuhäuser, R., Seifahrt, A., Vogt, N., Bedalov, A., Helling, C., Witte, S. and Hauschildt, P. H. (2008). *A&A*, 491:311–320.
- Schneider, P. (2006). *Einführung in die Extragalaktische Astronomie und Kosmologie*. Springer, first edition.
- Seifahrt, A., Helling, C., Burgasser, A. J., Allers, K. N., Cruz, K. L., Cushing, M. C., Heiter, U.,Looper, D. L. and Witte, S. (2009). In E. Stempels, editor, *American Institute of Physics Conference Series*, volume 1094 of *American Institute of Physics Conference Series*, pages 283–290.
- Sheppard, S. S. and Cushing, M. C. (2009). *AJ*, 137:304–314.
- Siegler, N., Close, L. M., Burgasser, A. J., Cruz, K. L., Marois, C., Macintosh, B. and Barman, T. (2007). *AJ*, 133:2320–2326.



- Smith, W. R. and Missen, R. W. (1982). *Chemical Reaction Equilibrium Analysis: Theory and Analysis*. Wiley-Interscience.
- Sromovsky, L. A. and Fry, P. M. (2010). *Icarus*, 210:230–257.
- Stephens, D. C., Leggett, S. K., Cushing, M. C., Marley, M. S., Saumon, D., Geballe, T. R., Golimowski, D. A., Fan, X. and Noll, K. S. (2009). *ArXiv e-prints*.
- Tarter, J. C. (1975). PhD thesis, AA(California Univ., Berkeley.).
- Tarter, J. C. (1976). In *Bulletin of the AAS*, volume 8 of *Bulletin of the AAS*.
- Thies, I. and Kroupa, P. (2007). *ApJ*, 671:767–780.
- Trieloff, M., Blum, J. and Klahr, H. (2009). *Meteoritics and Planetary Science Supplement*, 72:5215–+.
- Tsuji, T., Ohnaka, K., Aoki, W. and Nakajima, T. (1996). *A&A*, 308:L29–L32.
- Unsöld, A. (1955). *Physik der Sternatmosphären, mit besonderer Berücksichtigung der Sonne*. Berlin: Springer, second edition.
- Weigert, A. and Wendker, H. J. (2001). *Astronomie und Astrophysik*. VCH, third edition.
- Whitworth, A. P. and Stamatellos, D. (2006). *A&A*, 458:817–829.
- Witte, S. (2008). diploma thesis, Universität Hamburg.
- Witte, S., Helling, C., Barman, T., Heidrich, N. and Hauschildt, P. H. (2011). Dust in brown dwarfs and extra-solar planets. III. Testing of synthetic spectra on observations. *A&A*, in print.
- Witte, S., Helling, C. and Hauschildt, P. H. (2009a). *A&A*, 506:1367–1380.
- Witte, S., Helling, C. and Hauschildt, P. H. (2009b). In E. Stempels, editor, *American Institute of Physics Conference Series*, volume 1094 of *American Institute of Physics Conference Series*, pages 572–575.
- Woitke, P. (2006). *A&A*, 452:537–549.
- Woitke, P. and Helling, C. (2003). *A&A*, 399:297–313.
- Woitke, P. and Helling, C. (2004). *A&A*, 414:335–350.
- Wolf, S. and Voshchinnikov, N. V. (2004). *Computer Physics Communications*, 162:113.
- Wolszczan, A. and Frail, D. A. (1992). *Nature*, 355:145–147.
- Wuchterl, G. (2004). In A. Penny, editor, *Planetary Systems in the Universe*, volume 202 of *IAU Symposium*, pages 167–+.

Wuchterl, G. (2008). In H. Deeg, J. A. Belmonte, & A. Aparicio, editor, *Extrasolar Planets*, pages 89–+.

Zuckerman, B. and Becklin, E. E. (1987). *Nature*, 330:138–140.

Do not seek to follow in the footsteps of the wise. Seek what they sought.

Bashô, japanischer Dichter

Ein gut gemeinter Spruch, oder? Aber wenn man anfangs noch nicht einmal so genau weiss, was es eigentlich zu suchen gilt, läuft man dann doch eine Weile in den vorhandenen Fussspuren umher. Und auch später muß man sich doch immer wieder an diesen Spuren orientieren. Zu meinem Glück haben viele Menschen solche Spuren für mich hinterlassen, so daß ich letzten Endes dazu kam, ein, zwei eigene Fussabdrücke zu produzieren.

An dieser Stelle möchte ich daher all denen danken, die diese Arbeit möglich gemacht haben:

Zuallererst gilt mein Dank Peter Hauschildt, der mit seiner unvergleichlichen Art eine aussergewöhnlich kreative und entspannte Arbeitsgruppe am laufen hält und der trotz seines eng bemessenen Terminplans stets ein offenes Ohr für Fragen und Problemchen jeglicher Art hat. Vor allem aber gebührt ihm Dank für die Erschaffung von PHOENIX, dem coolsten Computerspiel ever. Im weiteren Sinne gilt der Dank also auch allen Anderen, die ihre Zeilen im Code hinterlassen haben.

Christiane Helling und Peter Voitke danke ich für ihr Staubmodell, die viele Unterstützung, die angenehme und erfolgreiche Zusammenarbeit, sowie die wunderschöne Zeit in St. Andrews.

Desweiteren gebührt Andreas Schweitzer ein riesiger Dank für all das schmunzelnde Beantworten dümmlicher Fragen, das Korrekturlesen dieser Arbeit und dafür, dass die Cluster trotz ihres erbitterten Widerstands doch immer noch so gut liefen.

Matthias Dehn bin ich nach wie vor dankbar für das Zähmen des Biests namens DRIFT-PHOENIX.

All meinen Office-Mates und den Mitgliedern meiner Arbeitsgruppe, einschliesslich aller Ehemaligen, sei gedankt für all den Austausch über Wissenschaftliches und Nicht-so-Wissenschaftliches.

Generell möchte ich allen Mitarbeitern an der Sternwarte, denen ich über den Weg laufen durfte, für die angenehme und spannende Zeit am Institut danken. Insbesondere der Besatzung des Hauptgebäudes für ihre freundliche Unterstützung bei all den kleinen Dingen die denn so angefallen sind und, nicht zu vergessen, für all die Kekse.

Dank gilt ausserdem meinen weiteren Gutachtern Robi Banerjee, Ralph Neuhäuser und Jürgen Schmitt.

Diese Arbeit und andere Publikationen wären nicht zustande gekommen ohne die Finanzierung durch das GrK 1351 und des SPP 1385 der DFG.

Im Rahmen meiner Arbeit habe ich verwirrt auf den Output diverser Rechner starren dürfen. Da eigentlich sie den Grossteil der Arbeit erledigt haben, sollen die Wichtigsten hier erwähnt sein: Atlan, hslxws13, Leo, Marvin, Nathan, Nebular, Seneca, Susi, Mythenmetz

Abschließend möchte ich meinen Eltern und meiner Mella danken, für all ihre Liebe und Unterstützung. Ohne sie hätte all das hier nie funktioniert.